NOVA SCHOOL OF SCIENCE & TECHNOLOGY

DEPARTMENT OF PHYSICS

RÚBEN MIGUEL GONÇALVES INOCÊNCIO

BSc in Physics Engineering

X-RAY ENERGY DISPERSIVE SPECTROMETER DEVELOPMENT IN A TRIAXIAL GEOMETRY

MASTER IN PHYSICS ENGINEERING

NOVA University Lisbon
September, 2023

NOVA SCHOOL OF
SCIENCE & TECHNOLOGY

DEPARTMENT OF
PHYSICS

X-RAY ENERGY DISPERSIVE SPECTROMETER DEVELOPMENT IN A TRIAXIAL GEOMETRY

RÚBEN MIGUEL GONÇALVES INOCÊNCIO

BSc in Physics Engineering

Adviser: Jorge Machado
Assistant Professor, NOVA University Lisbon

Co-adviser: Mauro Guerra
Assistant Professor, NOVA University Lisbon

Examination Committee

Chair: Yuri Nunes
Assistant Professor, FCT-NOVA

Rapporteur: Patrícia Carvalho
Assistant Researcher, FCT-NOVA

MASTER IN PHYSICS ENGINEERING

NOVA University Lisbon
September, 2023

X-Ray Energy Dispersive Spectrometer Development in a Triaxial Geometry

This document was created with the (pdf/Xe/Lua)LaTeX processor and the NOVAthesis template (v7.1.5) [1].

Acknowledgements

This dissertation would not have been possible without the advisory of professor Jorge Machado and professor Mauro Guerra, from them I found beauty in the world of Physics and I may have uncovered my biggest interests in science, their guidance allowed me to find purpose in my work and to grow as a student, a reasearcher and as a professional worker. I also want to highlight the unfailingly support given by professor Sofia Pessanha, which I'm very glad I encountered during my adventure. Professor André Wemans was always present from the very beginning of my course, he watched me grow as a student and fortunatelly will see me grow as a graduate, for his guidance in my disseratiation preparation and for all the support and conversations we had I want to thank him.

I will never forget to thank to Faculdade de Ciências e Tecnologia da Universidade de Lisboa, for the great institution it is and for the warming second home it was, it's Campus is a fresh breeze that inspires me everytime my creativity gets stuck. Beside much struggling, I want to spend some words thanking the effort that the Department of Physics invested in me, in us. During this last year, I spent whole months in the Atomic and Molecular Physics Laboratory, part of LIBPhys, from which I will keep methodologies and memories as it was my first laboratory experience.

I want to thank very much to Faustino, Sr. Afonso and Bruno, people like you are the ones that offer so much, teach so much and keep the departments flame burning, your experience and guidance taught me things that no professor would have. To my older lab partners, Daniel and César, I want to express my apreciation for your perseverence on pursuing a PhD and I want to thank you for the help you gave me that allowed me to perform a much complete research. This last months would not have been the same without Sara and Gonçalo, they were excellent partners and above all, friends.

To all the excellent and other academics I encountered, I want to thank you, preeminently to the other ones because those were the ones that pushed my limits and made me a more capable and resilient person.

My first personal acknowledgements are for Engenharia Física and its students, such talented poeple that elevated my university experience. I could not forget to mention my older colleagues, they taught me what is to be a Physics student and to be a better older

colleagues for my younger ones. To all the people that gave a part of their lifes to build and support the awesome Engenharia Física community, you have my full appreciation.

I want to thank to my little ones, Veggie, Bárbara, Iara and Rita, you laid a lot of responsability in me and I will never forget it. You made me realize that even when I lose faith in me, you once gave me yours. I want to thank to my older ones, Joana and Santos, you are a source of inspiration and experience, thank you for being here and for being who you are.

Félix, thank you for the intervals we had during our thesis writing, they were supposed to be relaxing but never were. Tiago, thank you for sharing more than 8 years of you patience with me. What crazy times we had, what crazy times we will have. Guida, the simple fact that we started as 25 freshmans and your name remained in this page, tells a lot about your meaning to me. A whole new world awaits us, lets face it!

To my family, you never fully understood why I spent so much time at the university, at the lab, at the computer, out of home. Maybe you do not realize how all my hard work fits my interest or the interests of the world. But that is exactly why I want to thank you, you never needed that realization to relentlessly support me in every decision I made. You built this safe bubble where I know I can always return, you are a rare refuge, that makes me very lucky in this world. Rafael, you will always be my little brother, even when you grew so much, you helped me to grow much more that you imagine. You are truly my greatest companion. I love you all.

Ana meu amor, if I am where I am, wiriting what I'm wiriting, its because you raised me everytime I was down. You are the ultimate representation of an ally for life, you inspire the best of me and complement the worst. Your character builds part of my identity and, as a consequence, helps me to give the best of me in every work I do, including this thesis. Thank you for your revision on my less impressive english. I love you.

Abstract

Energy dispersive X-ray fluorescence (EDXRF) spectrometry is a non-destructive method to perform qualitative and quantitative analysis of elements present in solid and liquid samples. This technique is widely used in industry and academia despite facing some difficulties on offering high signal-to-noise, due to *Bremsstrahlung* background noise, and because it deeply relies on a software capable of analysing the data assertively.

This dissertation presents the development of an EDXRF spectrometer in a triaxial geometry (3EDXRF) and a software for spectra analysis. The adaptation of the classical XRF setup into a triaxial geometry raises the signal-to-noise ratio by progressively eliminating the orthogonal components of the eletromagnetic field that makes *Bremsstrahlung* photons. Furthermore, this 3EDXRF spectrometer is coupled with a double crystal wavelength dispersive spectrometer (DCS) that enables analyses with greater energy resolution which makes this setup exclusive with high scientific importance. It was further developed a software for spectra analysis in *Python* that improves spectra reading by introducing exponential modified gaussians (EMG) to better fit the spectra components, achieving more reliable results. By modelling the observed phenomena using complex physical models and solving them with non-linear optimization algorithms, the elements in a sample are quantified.

While developing the cluster of spectrometers, the fluorescence spectra of a set of metallic alloys containing Ag, Cu and Zn were taken as a case study. The results from fitting the spectra are presented along with the quantification results. By implementing the EMG, the spectra fitting improved and the errors associated with the fit were reduced. Concerning the quantification, the methodology produced consistent results with the ones considered as a control, showing a potential success on modelling the physical phenomena considered in the quantification. However, quantification results show relative errors on the order of tens percent, indicating our model needs further developments in order to be more complete and accurate. Such improvements may start from considering multiple fluorescence events.

Keywords: Triaxial X-ray fluorescence spectrometry, Exponential modified gaussian, Quantification software, Fundamental parameters quantification

Resumo

A espectrometria por fluorescência de raios-X dispersiva em energia (EDXRF) é um método de análise não destrutivo de amostras sólidas e preparados líquidos que tem como objetivo caracterizar as amostras de forma qualitativa e quantitativa. Esta técnica é amplamente utilizada na indústria e na academia apesar de enfrentar desafios como a obtenção de espectros com uma razão elevado de sinal/ruído, devido ao fundo *Bremsstrahlung*, e a necessidade de ter um software que faça o tratamento dos dados com assertividade.

Nesta dissertação propõe-se desenvolver um espectrómetro de fluorescência de raios-X dispersivo em energia numa geometria triaxial e um software de análise de espectros. A adaptação a uma geometria triaxial aumenta a razão sinal/ruído por eliminação progressiva das componentes ortogonais do campo eletromagnético que compõem o fundo de *Bremsstrahlung*. Adicionalmente, integramos ao sistema descrito um espectrómetro de duplo cristal dispersivo em comprimento de onda, possibilitando análises com maior resolução em energia, o que torna este projeto único e de elevado valor científico. Foi ainda desenvolvido um software em *Python* que incorpora curvas gaussianas exponencialmente modificadas (EMG) para obter resultados mais fidedignos das componentes do espectro. Seguindo modelos físicos complexos, esta informação é tratada com recurso a algoritmos de otimização não-linear, tornando possível a quantificação dos elementos numa amostra.

Aquando do desenvolvimento do complexo de espectrómetros, foram medidos espectros de fluorescência de raios-X de um conjunto de ligas metálicas contendo Ag, Cu e Zn como estudo de caso. Os resultados da análise dos espectros são apresentados juntamente com o tratamento de dados para a quantificação. A implementação de EMG melhora significativamente a análise de espectros, reduzindo os erros na sua caracterização. Em relação à quantificação, os métodos produzem resultados coerentes com a quantificação de controlo, mostrando aparente sucesso na modelação dos fenómenos físicos considerados nos cálculos da quantificação. No entanto, os erros relativos são da ordem das dezenas de pontos percentuais mostrando que é necessário desenvolver um modelo físico mais complexo, considerando múltiplos fenómenos de fluorescência por exemplo.

Palavras-chave: Espectrometria Triaxial de Fluorescência de Raios-X, Curvas gaussianas exponencialmente modificadas, Software de quantificação, Quantificação por parâmetros fundamentais

Contents

List of Figures

List of Tables

Acronyms

3EDXRF Triaxial Energy Dispersive X-ray Fluorescence *(pp. iv, vi, viii, 1, 8, 11–16, 33, 39, 41)*

DCS Double Crystal Spectrometer *(pp. iv, 1, 11–13, 39)*

EDXRF Energy Dispersive X-ray Fluorescence *(pp. iv–vi, 1, 7, 11, 39)*
EMG Exponential Modified Gaussian *(pp. iv, v, viii, 16, 21–24, 37, 38)*
ESM External Standard Method *(p. 9)*

FCM Fundamental Coefficient Method *(pp. 9, 10)*
FWMH Full Width at Maximum Height *(p. 20)*

GDM Gradient Descent Method *(pp. 28, 29, 31)*
GNM Gaussian-Newton Method *(pp. 28, 29, 31)*

IUPAC International Union of Pure and Applied Chemistry *(p. 2)*

LIBPhys Laboratory for Instrumentation, Biomedical Engineering and Radiation Physics *(p. 11)*
LMA Levenberg-Marquardt Algorithm *(pp. 28, 29)*

NIST National Institute of Standards and Technology *(pp. 19, 26, 27)*

SDD Silicon Drift Detector *(p. 9)*

WDXRF wavelenght Dispersive X-ray Fluorescence *(pp. 7, 11, 39)*

XRF X-ray Fluorescence *(pp. 2, 3, 7, 21, 39, 41)*

Chapter 1

Introduction

1.1 Objective and Relevance

In this project we propose a quite rare experimental setup that improves the identification and quantification of atomic species in a non-destructive manner: an energy dispersive X-ray fluorescence (EDXRF) spectrometer arranged in a triaxial geometry (3EDXRF) coupled with a double crystal spectrometer (DCS). We also propose a software for spectra analysis - VerX - that pledges improvement in the way spectra are used for quantification purposes. This software was built to be verstatile in order to be easily upgraded to analize other than X-Ray fluorescence spectra and to be used on a regular computer.

1.1.1 Thesis Overview

In section 1 there is an introduction to the most general and fundamental concepts needed to understand the methods and results presented, as well as a descripton of the *State of the Art* concerning X-ray fluorescence spectrometry and quantification methods. In section 2 it is proposed a setup composed of multiple spectrometers that are in their final stages of development and aim to perform complete X-ray fluorescence analyses. A software for spectra analysis was developed entirely anew and it is presented in section 3. This software is able to label X-ray lines in a spectrum, to make an individual and overall fit of these components and to translate them into quantification of the elements in a sample. At the end, in section 4 and 5, the performance of the software in a case study is assessed and conclusions are taken from its results.

1.2 Theoretical Concepts

Nowadays, spectrometers are the most common method to qualitatively and quantitatively evaluate the elemental composition of a sample. A variety of entities can be induced and detected providing relevant information about the atomic species under analysis, from charged particles with a certain mass and kinetic energy, to photons from

every wavelength range. Nonetheless, our setup allows an analysis to be carried out via an X-ray fluorescence spectrum emitted by the sample.

1.2.1 X-Ray fluorescence spectrometry

X-ray fluorescence is a phenomenon in which an atomic species gets into an unstable state through ionization of their innermost shells, and to restore its energetic stability, an electron from a higher shell drops to the vacancy emitting an X-ray [2].

Unfortunately, there are a few phenomena that are not relevant to our type of spectrometry such as the emission of Auger electrons, that is more likely for atoms with fewer electrons, and the emission of satellite X-ray, that might be possible when there is a manyfold ionization of one shell [3, Chapter 3]. None of the last described processes is of interest and they can significantly disturb the resulting analysis. That being said, the number of X-rays emitted is always less than the number of ionizations due to these effects. As fluorescence is what concerns us, we define the fluorescence yield (ω) as it is commonly known [3–5]:

$$\omega_i = \frac{I_i}{n_i} \tag{1.1}$$

Where the ω_i is the fluorescence yield for vacancies of the i shell, I_i is the rate of events, like fluorescence, and n_i is the number of vacancies.

The justification for the strong interest in studying photons that come from different elements lies in the clear distinction that their energies possess since the energy of the induced X-ray only depends on the difference between the energy of the inner orbital and the initial one (equation 1.2). These energies are characteristics of each element [6], and allows us to determine which element corresponds to each X-ray based on its energy [2].

$$E_{photon} = E_{final} - E_{initial} \tag{1.2}$$

1.2.2 X-ray Terminology

It is commonly used a specific notation when referring to photons emitted by each electron transition, the *Siegbahn nomenclature*. This notation in named after Kai Siegbahn, and although there are currently other nomenclatures, such as the one proposed by the *International Union of Pure and Applied Chemistry* (IUPAC) [7], the nomenclature adopted in this document will be the one proposed by Siegbahn and is summarized in figure 1.1.

1.2.3 Ionization of the Sample

The existence of inner energetic levels on the atom is always implicit in an X-ray Fluorescence (XRF) analysis, so the most relevant and obvious constraint of this technique is the range of elements that can be identified, further on explained, since the atoms of the sample must accommodate at least two energetic levels.

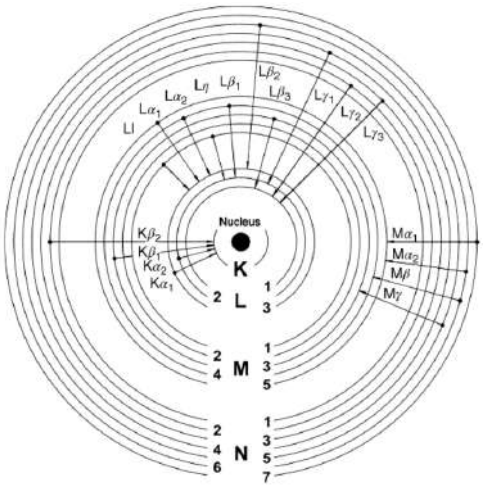

Figure 1.1: Diagram representing the Siegbahn notation for the X-ray lines. The displayed symbols, next to the arrows, corresponds to the X-ray emitted by the electron when performing the transition indicated by the correspondent arrow. Figure adapted from [8].

X-ray Tube

Ionization of the sample, in XRF, happens via photons with high enough energy to ionize these inner shell electrons. One way to obtain such energetic beams is using an X-ray tube. These technologies are basically composed of 4 principal elements [2, 6]: a set of filaments (cathode) which eject electrons by thermionic emission; a target (anode) where electrons will, ideally, collide to ionize its atoms; a glass envelope to sustain the vacuum inside; and a protective housing so that x-rays in unwanted direction get absorbed (figure 1.2). The X-rays emitted from the X-ray tube are photons created by transiting electrons from higher energy states to the hole left in inner states, within the atoms of the target placed on the anode.

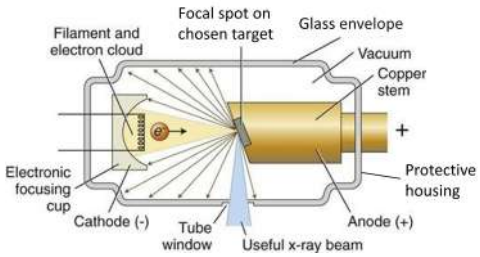

Figure 1.2: Schematic of an X-ray tube where the four main components are highlighted: the cathode composed of a focusing cup and a filament; the anode where a target is placed; a glass envelope; and a protective housing. Adapted from [9].

Spectrum of an X-ray Tube and *Bremsstrahlung*

Interestingly, the beam of X-rays emitted from the tube is continuous in energy and not only composed of characteristic lines of the atoms from the target. This happens because the X-rays are generated as a result of 2 processes [6, 10]:

1. Ionization of the inner shells of target atoms - As mentioned, the thermionic emitted electrons are accelerated according to the voltage applied on the electrodes. The electron ionizes, for instance, the K levels of the target atoms creating a vacancy that will be occupied by a higher state electron with emission of the characteristic X-ray photon.

2. Deceleration of the incident electron - When accelerated towards the anode, the thermionic electrons may not collide with the target atoms, being decelerated and geting their trajectories brutally altered. The loss of kinetic energy is emitted as electromagnetic radiation called *Bremsstrahlung* radiation [11, chapter 3]. The energy is continuous since the alteration of the electron trajectory can be vastly different, with different losses of energy. It should be noted that the range of this radiation can be as high as the maximum kinetic energy of the electron (equation 1.3).

$$E_{max} = eU_0 \tag{1.3}$$

These two phenomena compose a much more complex spectrum of incident X-rays, as illustrated in figure 1.3, an example from an X-ray tube using a Tungsten (W) anode.

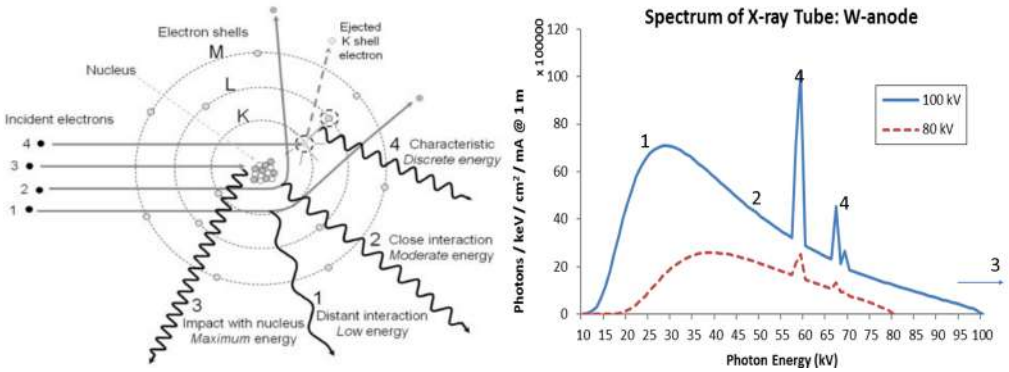

Figure 1.3: Diagram explaining the four types of interactions that can occur when trying to produce X-rays. The emitted photons according to the electron-W atom interactions, are represented both in the scheme (on the left) as on the spectrum (on the right). It is also represented the loss of characteristic X-rays when the electric potential on the tube is less than 100kV empowering the urge of having high accelaration voltages on the X-ray tube. Adapted from [10, 12].

It is universally known, that X-rays are electromagnetic waves made of an oscillating electric field perpendicular to an oscillating magnetic field [13]. X-rays are polarized if the

electrical field has a preferred directionor, or non-polarized if not [6]. The described continuous X-ray spectrum is almost entirely non-polarized even though some polarizability can be observed.

If the spectrum depicted in figure 1.3 is directly aimed toward the sample that we want to analyze (planar geometry), the X-ray beam is going to interact with atoms of the sample through three possible phenomena [6]:

1. Ionization of the atom and emission of a characteristic X-ray - **X-ray Fluorescence** (figure 1.4 - 1)

2. Photon scattering

    a) The incident X-ray ionizes an outer shell electron, losing a fraction of its energy, resulting in an ejected electron and a different photon with less energy - **Compton Scattering** - this phenomenon increases with light elements and disappears with heavier elements (figure 1.4 - 2a)[14].

    b) The incoming X-ray collides with a strongly bound electron that starts to oscillate at such a frequency that allows it to re-emit a photon with the same energy as if the photon was reflected by the atom - **Rayleigh Scattering** - this phenomenon is reduced for light elements and keeps occurring with heavier elements (figure 1.4 - 2b).

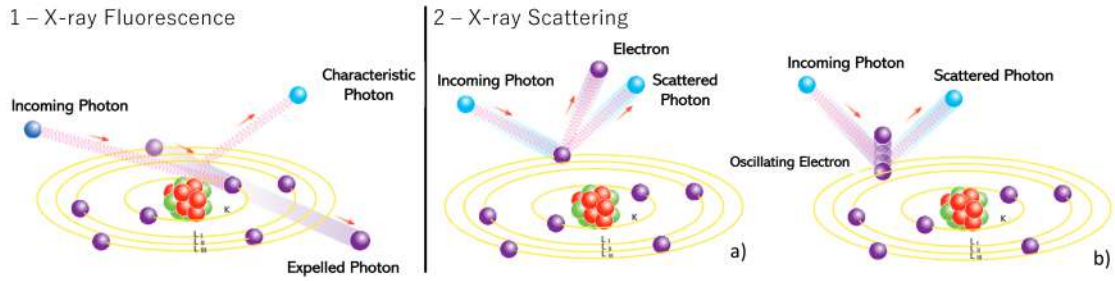

Figure 1.4: Types of interactions between an incident X-ray and the atom in analysis. 1) X-ray Fluorescence - it is emitted a characteristic X-ray of interest; 2a) X-ray Compton Scattering - the scattered photon has lower energy than the incident one; 2b) X-ray Rayleigh scattering - the scattered photon is "reflected" with the same energy. Adapted from [6].

1.2.4 Matrix Effects

In an ideal scenario, the intensity of a characteristic line of an element should only be proportional to the concentration of the element. Unfortunately, there is a dependence on the concentration of other coexistent elements and on the thickness of the sample. These are the reason behind the so-called matrix effects. These effects disturb the quantification of the element concentration in our sample in two possible ways [15, 16]:

1. Attenuation

The characteristic x-rays, instead of being emitted by the sample, are absorbed within the sample due to the mass attenuation coefficient that characterizes the sample. A similar process may take place with source x-rays on their way to ionising the sample atoms.

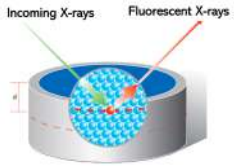

Figure 1.5: Absorption effect. Adapted from [6].

When the wavelength of an analyte line A is just less than that of the absorption edge of a particular matrix element B, the A line is highly absorbed by the element B, and the A line intensity is reduced in a proportion equivalent to the B concentration

---

Dr. Richard M. Rousseau in [15]

2. Enhancement

When a characteristic X-ray travels directly to the detector without any inelastic interaction it is called *primary fluorescence*. However, *enhancement* effects may occur if these X-rays ionize a secondary atom producing a different characteristic X-ray with alteration of the first one.

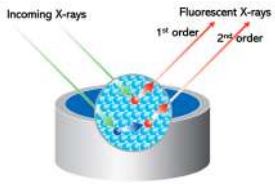

Figure 1.6: Absorption effect. Adapted from [6].

When the wavelength of the analyte absorption edge (A) is just greater than that of the line of a particular matrix element B, the B line is absorbed by A, and the A line intensity is enhanced (or increased) in a proportion equivalent to the B concentration.

Dr. Richard M. Rousseau in [15]

These two phenomena represent an obstacle to the analyses of samples, specially when quantification is at stake. Such matters have more importance with thicker and heavier samples, which constitution turns these effects more likely. This is why so many studies and approaches [17–20] are taking place in order to theorize with accuracy these effects to make relevant contributions to algorithms capable of fully quantify such samples.

1.3 State of the Art

XRF spectrometry is already implemented in the industry with a variety of applications, different technologies and different approaches. Regarding XRF spectrometers, and its application in solid samples, we can regroup them into two families [2]: the EDXRF and the Wavelength Dispersive XRF (WDXRF). EDXRF spectrometry distinguishes the different energy lines at the detector, resulting in a very versatile method but with generally less resolution in energy; the WDXRF spectrometry needs a well-parameterized dispersive medium (like a crystal) to decompose the spectrum and to focus the detector into a very small range of energies, thus having very higher resolution in energy.

There is a limit to the atomic numbers to be detected by XRF because as the number of protons in the nuclei increases, the energy required to ionize a K or L level also increases to unsustainable energies. The energy range which are able to analyze is also an important constraint we must take into account. To summarize, disregarding other possibly significant constraints, the XRF technique is mostly capable of identifying elements with atomic numbers from 4 (beryllium) in a WDXRF spectrometry (because it is the lightest element with more than one shell) or from 11 (sodium) in an EDXRF spectrometry which is the technology we present, to 92 (uranium) often identified using its L-lines (less energetic) [4, 6].

1.3.1 EDXRF Geometry

As already illustrated in figure 1.3, a spectrometer that uses a *bremsstrahlung*-saturated spectrum to excite the sample may not be able to distinguish less intense peaks of interest, due to the elastic scattering of *bremsstrahlung* in the sample. These kind of spectrometers, that directly aim the X-ray spectrum towards the sample, have a planar geometry.

Our goal is to produce an EDXRF spectrometer that eradicates, at its fullest, the *bremsstrahlung* background, leaving a cleaner spectrum with the characteristic lines of the elements of the sample. This ideal scenario cannot be achieved in a planar geometry, even if a set of filters attenuating a narrow range of energies is applied.

In pursuit of an ideal scenario, we propose to turn this setup's geometry into a triaxial geometry like the one presented in figure 1.7. Setups of this nature have proven to be powerful with truly enhanced results in inumerous subjects, such as biological tissue analyses [21], human remains [22, 23], artifacts with cultural value [22], or even human blood [24]. This assembly is composed of an X-ray tube, a secondary target and a third target where the sample is placed. This geometry divides the existing radiation into three stages: the spectrum obtained at the exit of the X-ray tube, one after the secondary target, and the one of interest that is indeed detected after the sample.

The continuous X-ray spectrum emitted by the X-ray tube is mainly composed of non-polarized radiation, whose electric field must always be perpendicular to the direction of propagation. After being reflected according to the three possible cartesian directions,

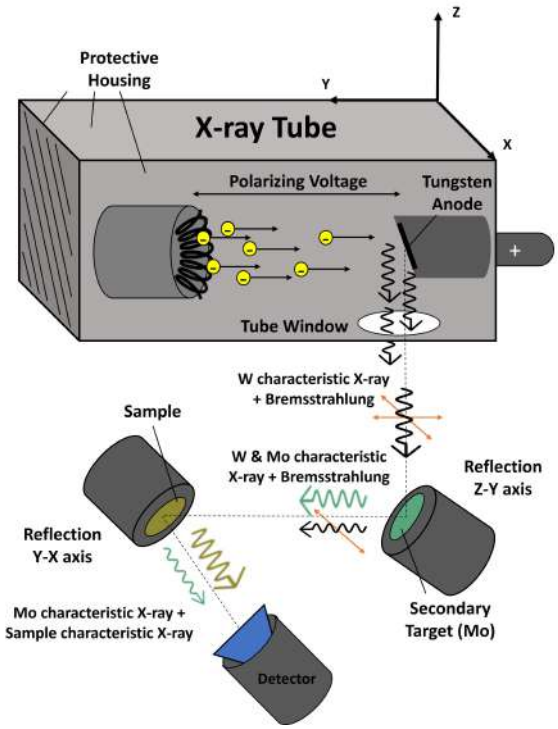

Figure 1.7: 3EDXRF spectrometer setup using a W anode X-ray tube, a Molybdenum (Mo) secondary target and a sample holder. The spectrum at the exit of the tube is composed of W characteristic X-ray and *Bremsstrahlung*; after interacting with the secondary target, one of the *Bremsstrahlung* electric field components is destroyed and is emitted Mo characteristic X-ray; after interacting with the sample, the last *Bremsstrahlung* electric field component vanishes, the W X-rays are very attenuated resulting in a spectrum without background and with the Mo and sample characteristic lines.

the electric field is progressively eliminated. Thus, the *Bremsstrahlung* background is completely eradicated [6], leaving only the characteristic lines of the secondary target and the sample as seen in figure 1.7. The interest of a clearer X-ray beam is explained by a general increase of signal-to-noise ratio, allowing higher signal-to-noise ratios which can lead to more accurate quantifications [22, 25].

In summary, this geometry offers enormous advantages in how clearly the less intense characteristic lines are emitted and how well we can detect them and deduce the elements that compose a given sample. All this comes at a cost: all the reflections performed until the beam reaches the detector cause an immense loss of X-rays that must be compensated with more detection time.

1.3.2 Energy Dispersive Detection

At the final stage of the spectrometer, the detected beam is a combination of different characteristic X-rays that have to be distinguished according to their energies - Energy Dispersive. All this analysis is carried away by the type of detector in use, which should be able to produce an electric signal proportional to the energy of the detected photon.

The most suitable type of detectors are Silicon Drift Detectors (SDD), these are the ones implemented in our project.

SDD works on an extensively examinated principle, the photoelectric effect. The incident X-ray is absorbed by the SDD material using its energy to create a certain number of electron-hole pairs, according to the SDD type of material. Then, the electron drifts through under the influence of an electric field, giving forth a small electric signal [26]. The number of created pairs is proportional to the absorbed energy, so more energetic X-rays create a larger number of electrons, thus higher signals are linked to more energetic photons.

These detectors need to be as fast as possible in resolving an X-ray contribution to prevent different signals from different X-rays from blending into one another resulting in undesired phenomena such as pile-up peaks. Pile-up peaks appear when different photons are absorbed within a short period of time, so the generated signal misleads us to think that a photon with the sum of the incident energies was detected [27], which is wrong.

1.3.3 Quantification Methods

It would be relatively easy to qualitatively identify the elements that compose the sample. Nevertheless, it would be highly complex to calculate nearly exact concentrations mostly because of the discussed *matrix effects*. A set of analytical methods can be used to accurately quantify the elements in a specimen. These quantification methods are divided into two main groups: *comparative methods* and *mathematical methods*; and each of these has a thread of consecutively specific methods (figure 1.8).

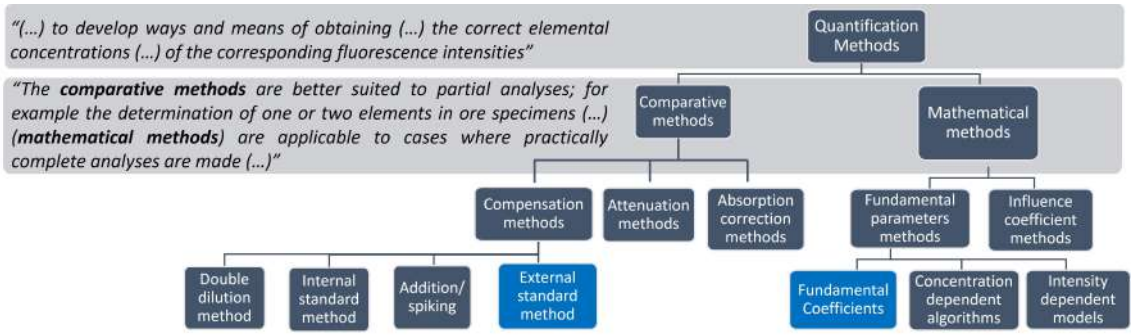

Figure 1.8: Schematic hierarchy of the relevant quantification methods for this work, the highlighted (in light blue) methods are the ones in discussion in this thesis. Adapted with citations from [28].

Our goal is to develop a software that enables the quantification of elements in a sample using the *External Standard Method* (ESM), but mainly through the *Fundamental Coefficient Method* (FCM). In an ESM, it is vital to have a good set of standards to compare our sample, which means having a set of well-known matrices (similar to the matrix of our sample) with a good knowledge of the elemental concentration. These methods can

lead to great results specially when analyzing samples with light matrices as shown by Machado et al. [29].

In FCM, there is a demand for a mathematical model which takes atomic fundamental parameters or even geometrical ones related to the setup and tries to mimic the amount of charactheristic X-rays detected when a certain amount of ionizing X-rays hit the sample. A pioneer researcher, Jacon Sherman, tried to elaborate such physical model through a mathematical relation he created, the *Sherman's equation* [30]:

$$I^i_{theor} = f(C^i_{approx}, K^i_1, K^i_2, ..., C^j_{approx}, K^j_1, K^j_2, ...) \tag{1.4}$$

Where the intensity of an X-ray line from an element i (I^i) is function of the fundamental coefficients of the element i (K^i) and other elements j (I^j), their concentrations (C^i) and (I^j) and geometrical parameters. From analogous equations, theoretical elemental concentrations are calculated and relative intensities can be estimated as well. Comparing these theoretical intensities with the ones measured from the practical spectrum, the theoretical concentrations are adjusted and new theoretical intensities are obtained. This is an iterative process that stops when the relative deviation from the results of consecutive iterations is below a given threshold [28]. There are also non-variable inputs to the function, such as: X-ray tube intensity, detector's efficiency, atomic charactheristics of each element (fluorescence yields, jump ratios,...). Although they might be difficult to take accurately into account, they can also be merged into coefficients that play a role into the optimization process. Nowadays, there are inumerous interpretations of the Sherman's equation which led to fundamental based quantifications with different approximations, geometrical and physical considerations according with each apparatus [31–33]. There are also softwares, some already working in industry, that aim to implement such theory merged with highly optimized mathematical algorithms in order to quickly simulate spectra based on very few prior information [34, 35].

Chapter 2

Apparatus Overview

The improvement in signal-noise ratio, the versatility and the wide range of scientific applications are the most significant motivations for developing a 3EDXRF spectrometer. Having an apparatus capable of performing quantitative and qualitative analysis on a sample and reaching compatible results through distinct approaches is a step forward in achieving consistant and coherent results. In pursuit of excellent scientific research, a system of spectrometers that includes a 3EDXRF spectrometer and a WDXRF spectrometer is being developed, by our group, and combined in the same apparatus.

2.1 Cluster of Spectrometers

Within the *Atomic and Molecular Physics Laboratory*, part of the *Laboratory for Instrumentation, Biomedical Engineering and Radiation Physics* (LIBPhys), a 3EDXRF spectrometer is undergoing finalization and will be assembled together with a DCS (a WDXRF spectrometer), sharing ammongst them the same X-ray tube and secondary target holder as illustrated in figure 2.1. Despite the combination of these two spectrometers, they can not analyze the same sample simultaneously. But the way these two are connected enables an easy switching between EDXRF and WDXRF.

When using the 3EDXRF configuration, the triaxial geometry must be respected, so the X-ray beam is firstly aimed at the secondary target placed at a 45° angle which redirects the beam towards the sample, exciting it, and once again redirecting the characteristic X-ray beam towards the last direction aiming at the detector. When one wishes to perform a WDXRF using the DCS configuration, the secondary target is replaced by the sample allowing the characteristic X-rays to exit the 3EDXRF spectrometer chamber and enter the DCS ready to be scattered by the crystals that compose it. These steps are visually explained further on.

To summarize, having a functional DCS combined with the 3EDXRF spectrometer improves the quality and precision of the analises because of the high-resolution these provide, allowing us to easily distinguish the X-ray contributions presented in a XRF spectrum. When having a set of crystals from which the crystallography characteristics

are known with tremendous detail, an extremely high precision in energy is possibly achieved through *Bragg's Diffraction*. By changing the angle of diffraction, researchers can cover a fairly wide range of energies, always with the ability to distinguish closely spaced peaks in energy within fluorescence spectra and characterize complex materials with fine detail, providing the system with higher chances of groundbreaking results.

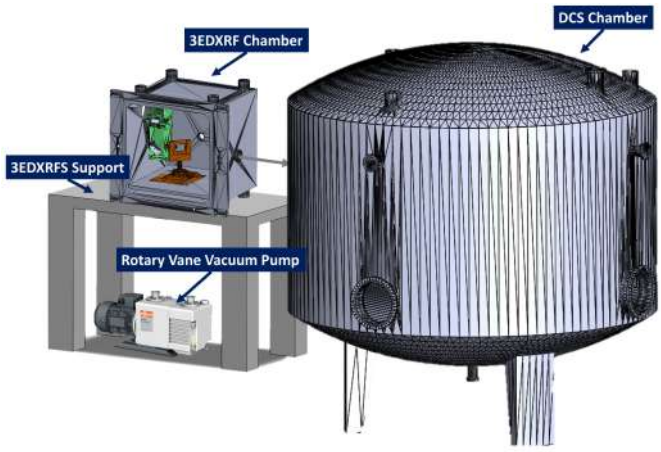

Figure 2.1: Representation of the whole apparatus, including the 3EDXRF spectrometer open chamber placed upon a steel support holding. On the bottom, a rotary vane vacuum pump. Inside the 3EDXRF spectrometer chamber, there is the 2^{nd} target case (in green) and the sample holder (in orange).The connection to the DCS chamber is made on the side of the 3EDXRF spectrometer chamber and by removing the sample holder and placing the sample in the 2^{nd} target holder instead, the characteristic beam can reach the DCS chamber.

2.2 Triaxial X-ray Fluorescence Spectrometer

As emphasized in the above description, the development of this 3EDXRF spectrometer and the DCS is parallel and collaborative, requiring constant review and consideration in order to operate seamlessly. On the other hand, once the 3EDXRF spectrometer is fully operational by itself, it is possible to make analyses despite the DCS not being fully operational yet.

2.2.1 3XRF In The Cluster

The mentioned 3EDXRF spectrometer can be divided into five main parts: the X-ray tube, the secondary target holder, the sample holder, the detector, which will be placed inside a chamber, and lastly the vacuum system. For a thorough analysis, all these parts needed to be developed or assembled together with maximum caution in order to preserve the triaxial geometry and to assure the perfect alignment with the DCS. Figure 2.2 represents a schematic of all these components in their final arrangement.

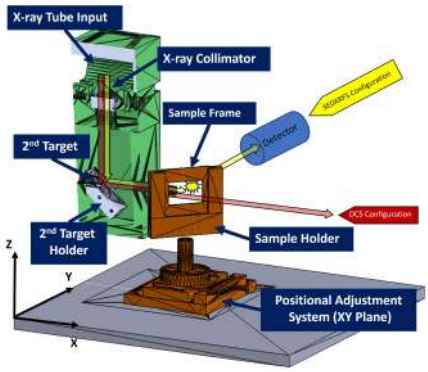

(a) Representation of the X-ray tube entrance, a section of the 2^{nd} target case, the sample holder and the detector.

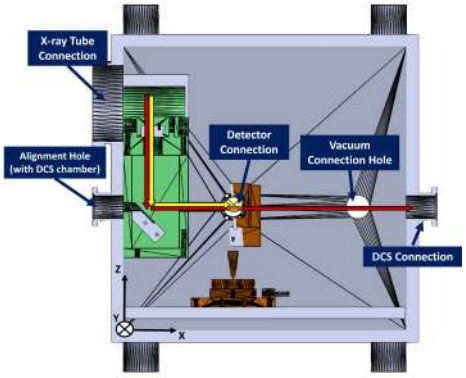

(b) Frontal representation, with a vertical section, of the 3EDXRF spectrometer along with the connection path to the DCS and the vacuum exit.

Figure 2.2: Representation of the principal elements that compose the 3EDXRF spectrometer. The assembled elements are fixed inside a vacuum chamber that connects with the DCS chamber and also has a connection to the vacuum system (rotary vane pump). It is represented in the possible paths of the X-ray beam according to the type of spectrometry to be performed: in yellow according to the 3EDXRF configuration, and in red the DCS configuration.

The two operation modes can be visualized in figure 2.2 specially when analysing the 3EDXRF configuration. The X-ray tube is placed inside the secondary target holder so that the X-ray beam is focused, along the Z axis, towards the secondary target. The secondary target holder is placed at a 45° angle allowing the beam to follow an orthogonal direction (X direction). Until this stage, the X-ray beam follows the exact same path in both configurations as represented by the yellow and the red arrows in figure 2.2b and 2.2a, representing the beam during the 3EDXRF and the DCS operation modes respectively. The only difference being what is placed in the secondary target holder, a secondary target if working in the 3EDXRF configuration or the actual sample if working as DCS. The next interaction will be one of two: either the sample is placed in the secondary target holder, so the beam proceeds to the DCS chamber (red arrow representing DCS analysis); or the sample is placed in the sample holder and a final excitation occurs in sample and the characteristic X-rays are collected in a detector aimed along the Y axis.

All the setup presented in figure 2.2 is aligned in a vacuum chamber ready to support fine vacuum, around $10^{-3}mbar$. Although vacuum is not mandatory to perform this experiment, the X-ray attenuation and scattering caused by air molecules is decreased, improving the quality of the spectrum acquired.

2.2.2 Other 3EDXRF Setups

While developing the cluster 3EDXRF+DCS, two major setups were used to acquire spectra with the intention of developing a tool capable of analysing them and quantifying the respective samples as a final objective. These two setups are also 3EDXRF spectrometers

but they were built separately, as individual apparatus. In figures 2.3 and 2.4 there are representations of them both. These two setups are simpler than the 3EDXRF spectrometer first mentioned, yet they are still composed of an X-ray tube, a secondary target case, a sample holder and a detector.

2.2.2.1 High Voltage 3EDXRF spectrometer

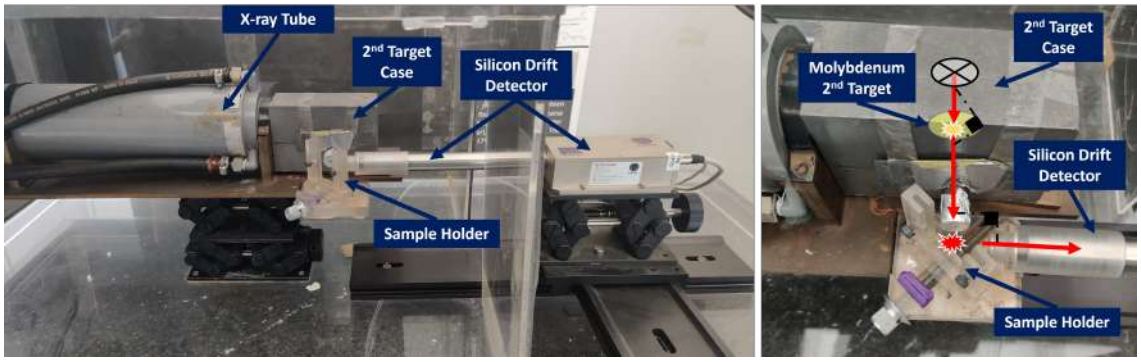

(a) 3EDXRF spectrometer setup containing a Molybdenum 2^{nd} target and a 50kV powered W X-ray tube.

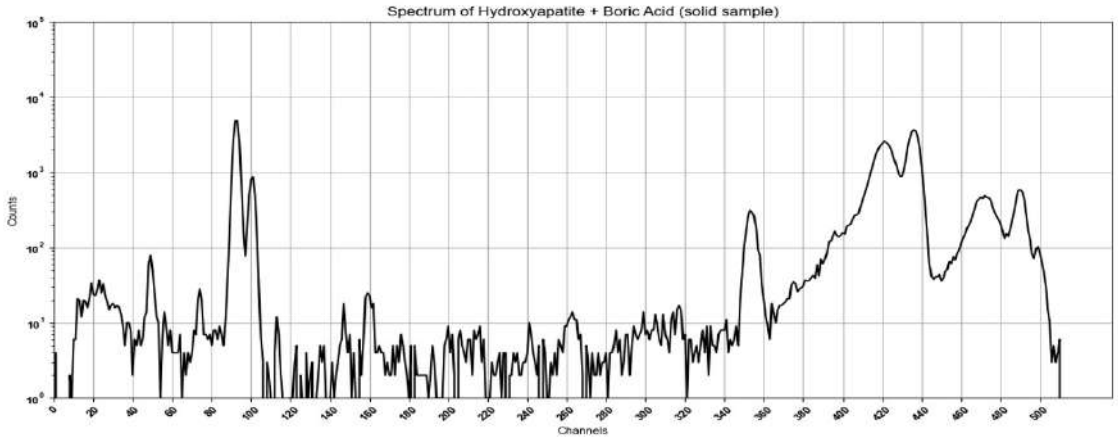

(b) Example of a spectrum acquired in the setup represented in (a). The sample contains Hydroxyapatite and Boric Acid in a solid pellet for quantification purposes.

Figure 2.3: Representation and description of a high voltage 3EDXRF spectrometer and an examplary spectrum acquired by it.

The setup described above makes use of an X-ray tube powered by a high voltage supply reaching 50kV and a Mo secondary target. These features enable the analyses of sample containing heavier elements, since Mo is a relatively heavy element producing high energy K_α capable of ionizing element which inner shells hold less energetic bounds, an example of such applications are given by Pessanha et al [20].

2.2.2.2 Portable 3EDXRF spectrometer

Figure 2.4 illustrates a less powerful X-ray tube with Mo as the target within the tube and a W as secondary target. With such setup, less energetic X-rays are emitted from the

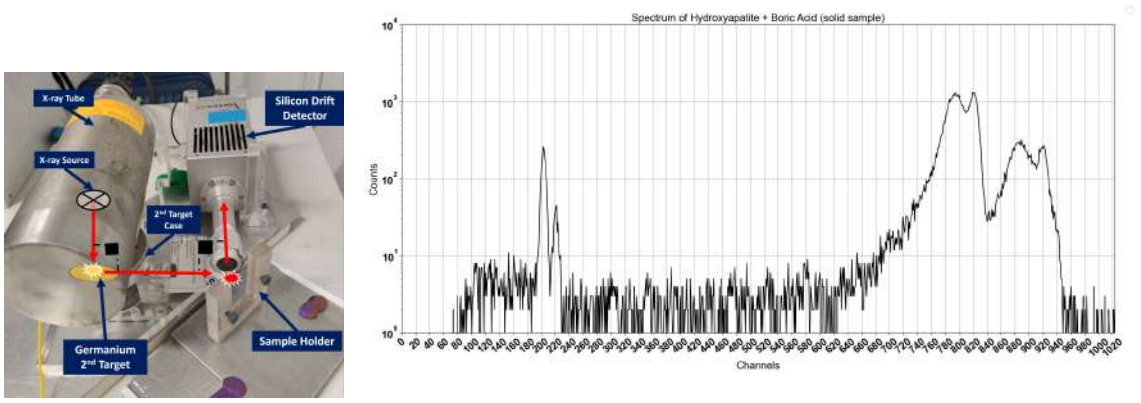

Figure 2.4: Representation and description of a portable low voltage 3EDXRF spectrometer setup with a Molybdenum (Mo) X-ray tube and an examplary spectrum acquired by it. The sample is the same as the one used above (Hydroxyapatite and Boric Acid).

X-ray tube, so only elements with inner shell energies lower than Mo K_α X-rays can be used as secondary targets. The fact that this setup is portable represents a great advantage for researchers that are now able to perform analysis *in situ* [22, 23]. In figure 2.4 is shown a spectrum of the exact same sample analyzed in figure 2.3b, but using this portable setup with an Y secondary target.

The main difference between both spectra figures (2.3b and 2.4) is the presence of K lines (Rayleigh and Compton components) corresponding to the secondary targets used in each setup, but also the appearance of either less energetic X-rays (when using Ge secondary target) or much higher X-rays (when using Mo secondary target). To understand these spectra we need to be aware that the secondary target is a limiting factor to the analysis. The X-rays coming from this target have the highest energies that we can visualize in a fluorescence spectrum, since its their X-rays that will excite the samples. These observations can possibly mean that X-rays have higher probability of producing fluorescence on atomic shells when presenting similar, but lower, energies when comparing to the incident beam. The biggest inconvenient of using lighter targets is the loss of range, because with lower energy there would be many elements that would not be ionized, thus we would not see any signature of these elements on the X-ray spectrum. Therefore, in figure 2.3b a considerable number of signatures can be unlocked and presented to the researcher.

In figure 2.3a (on the right side) and in figure 2.4, diagrams explaining the path of the X-ray beam through the spectrometer are shown. From the X-ray source, until it reaches the detector the phenomena and the way the triaxial geometry is accomplished is similar to the 3EDXRF spectrometer already presented in subsection 2.2.1.

Chapter 3

Spectra Analysis Software – VerX

A vital starting point of any energy dispersive X-ray spectra analysis is to properly distinguish relevant X-ray line contributions from noisy fluctuations at the same time it calculates the detected photon rate at a sufficiently wide range of energies. To ensure software flexibility according to the spectrometer system in use, we developed a fully functional spectra analysis software, named **VerX**.

This software, developed in *Python*, aims to identify the most relevant X-ray peaks, perform a Gaussian fit or an EMG fit to the individual resolved peaks and integrate each one of them in order to proceed with further quantification algorithms. It must be noted that this software is built to be adapted to a much more extensive range of photon-driven spectrometry techniques and to be implemented in any computer capable of running python scripts.

3.1 X-ray Lines Searching

In 3EDXRF the obtained spectra are composed of well-defined peaks corresponding to X-ray lines of the sample elements, either K, L or M lines (depending on the energy detection resolution). Not all of these lines can be recognized since some of them, due to their intensities, are blended with noise. However, as already explained, background noise is not a major concern in triaxial geometry spectrometry, since *Bremstrahlung* background gets immensely eliminated due to loss of normal polarization on the consecutive beam reflection along the three cartesian directions.

It is important to note that all lines are represented by two contributions, an elastic scattering (Rayleigh phenomena) which preserves the energy of the photon and an inelastic scattering (Compton phenomena) which results in a predominant loss of the photon energy. For the elements of the sample, only the Rayleigh contribution can be recognized, while the lines of the secondary target give rise to Rayleigh but also significant and quantifiable Compton contributions. Figure 3.1 is an example of a simple spectrum obtained in the 3EDXRF spectrometer presented above in figure 2.4.

To identify peaks like the ones in 3.1 an algorithm was created that, for every channel,

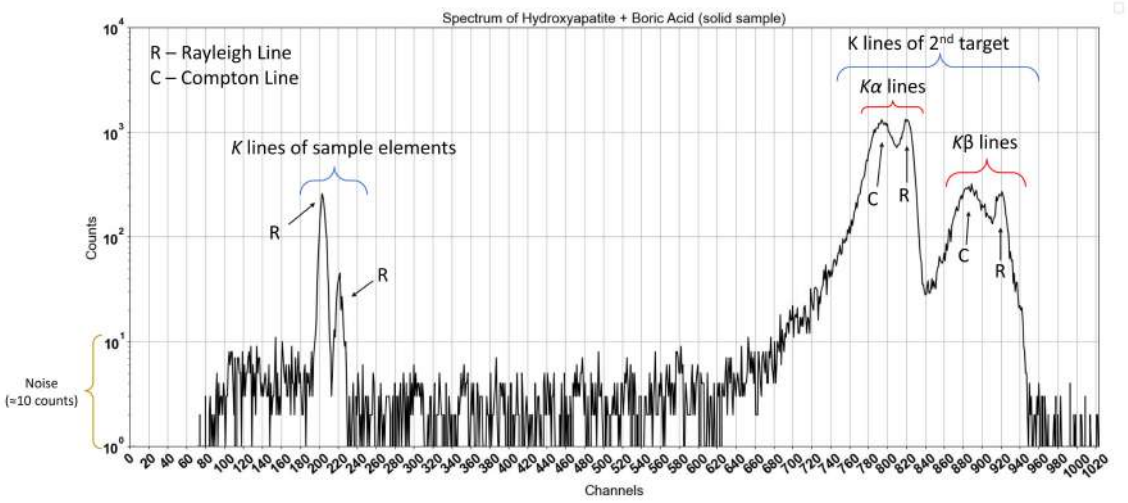

Figure 3.1: Example of an Hydroxyapatite spectrum, with 1024 channels (x-axis) and counts in logarithmic scale (y-axis). It always presents 4 lines (on the right) representing the Rayleigh and Compton contributions of the $K\alpha$ and $K\beta$ lines of the secondary target. The lines on the left are representative of the elements in the sample. The noise is reduced when compared with the planar geometry spectrometry and it is about 10 counts.

evaluates how many adjacent channels (lower and higher channels) have fewer counts than the one in analysis. Then it is assigned to each channel a score that is equal to the number of channels between them and the closest one with more counts. There are a couple of exceptions in the assignment of score: if the analyzed channel is the first or the last, it is automatically assigned a score of 0; if the difference of channels between one channel and the closest one with more counts is bigger than the difference of channels between the first or last channel, then the score is the difference between the present channel and either the first or last channel; and if the channels present counts under a predefined value of counts, the channels gets a score of 0.

This algorithm creates an array where is stored the score of each channel. This is graphically represented in figure 3.2. By plotting an horizontal line at $Score = 10$ it is very easy to identify potential peaks.

After this assessment, the channels with score and counts above a certain threshold are stored in pairs *channel-counts* and a set of peaks is finally recognized. A diagram of this algorithm is shown in figure 3.3.

To overcome possible unresolved peaks, the user can specify the channel of the visible peak that the software missed. This feature prevents an incomplete, and so incorrect, analysis but is also useful to indicate X-ray lines that, despite our knowledge *a priori* about their existence, are disguised within major contributions or even Compton peaks. A prime example where this feature has proved to be useful is during the analysis of alloys composed of Nickel (Ni), Copper (Cu) and Zinc (Zn), since the energies of their X-ray lines lay really close to each other. It is also possible to eliminate false-positive peaks pointed out by the algorithm.

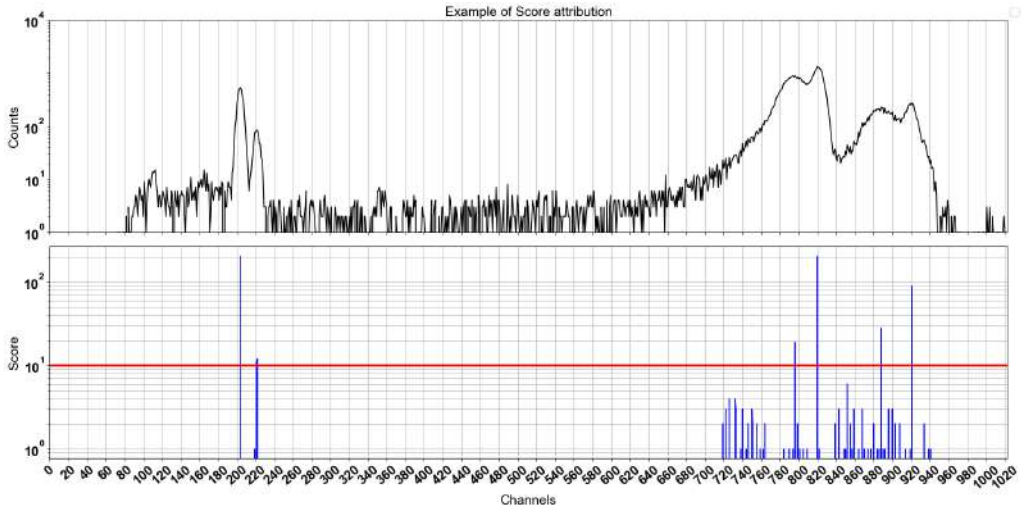

Figure 3.2: Representation of an array of scores given to each channel according to the distance of each channel to the closest adjacent channel with more counts. The red horizontal line allows the selection of potential peaks.

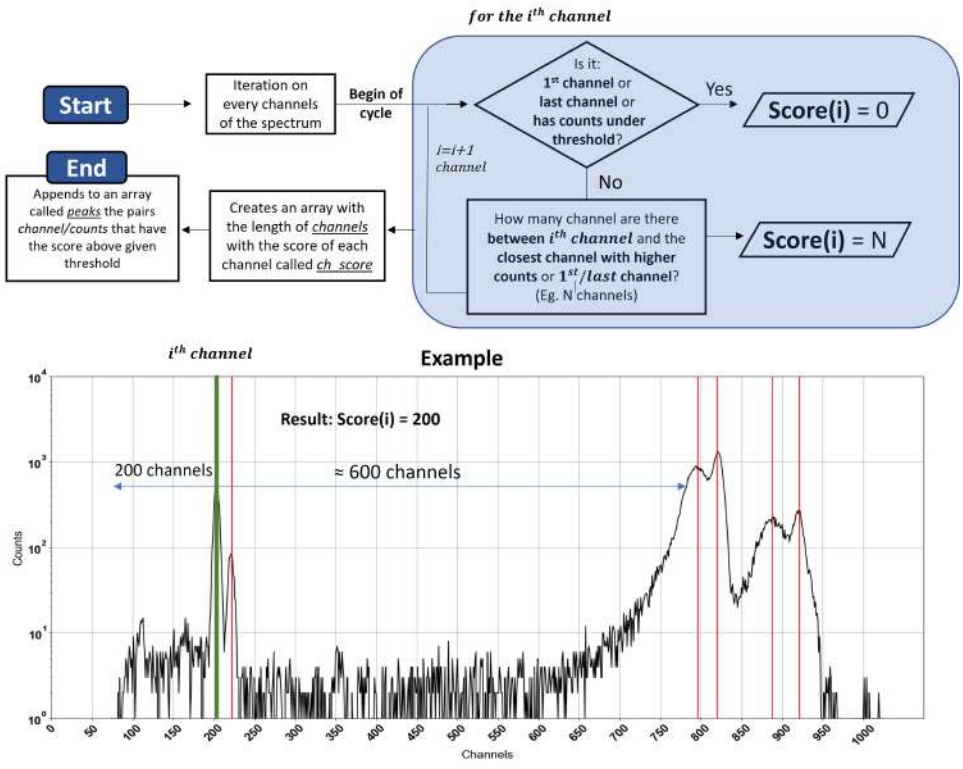

Figure 3.3: Above diagram explaining the operation performed by the algorithm that finds possible peaks in the spectrum (below). The red vertical lines identifies the possible X-ray contributions and the green vertical line represents the peak in analysis. The calculated score for the i^{th} is 200 following the rules described in the diagram above.

3.2 X-ray Lines Identification

Locating a peak in a spectrum does not mean acknowledging which element is in the sample. It is fundamental to build a function that converts channels into energy, an energy calibration curve. This curve can be regarded as a straight line obtained knowing at least two pairs of channel-energy. Usually, $K\alpha$ and $K\beta$ X-ray lines of the secondary target in use are part of the points use to construct the line since they are easily identifiable due to their Compton component with a distinctive shape on the left side of these peaks. It must be noted that the curve precision depends on the number of points used in the interpolation to calculate it and also on the channels used, the more spread the channels of the points are, the better the curve will be obtained.

To perform this calculation, were gathered X-ray transition energy values for $K\alpha$, $K\beta$, $L\alpha$, $L\beta$ presented in the *X-Ray Transition Energies Database - National Insitute of Standards and Technology (NIST) Standard Reference Database 128*[36], meticulously calculated and measured by NIST and european laboratories [37].

Once this database is imported it is possible to proceed with the calibration curve calculation. During the analysis and after the peak searching, the user must associate two or more of the identified peaks with X-ray lines in the database, gathering all the requirements to complete the calculation. To overcome hypothetical errors in the peak labelling, the software may ask the user to clarify, among X-ray lines having similar energies, which is the most likely line for the peaks in doubt. This clarification is used to improve energy calibration accuracy. An exemplary analysis of pine needles - *Pinus taeda* - Standard Reference Materials 1575a from *NIST database* was performed (datasheet of the sample is presented in annex2). Figure 3.4 shows the final result of the mentioned labelling, along with the energy calibration curve on the left top graph.

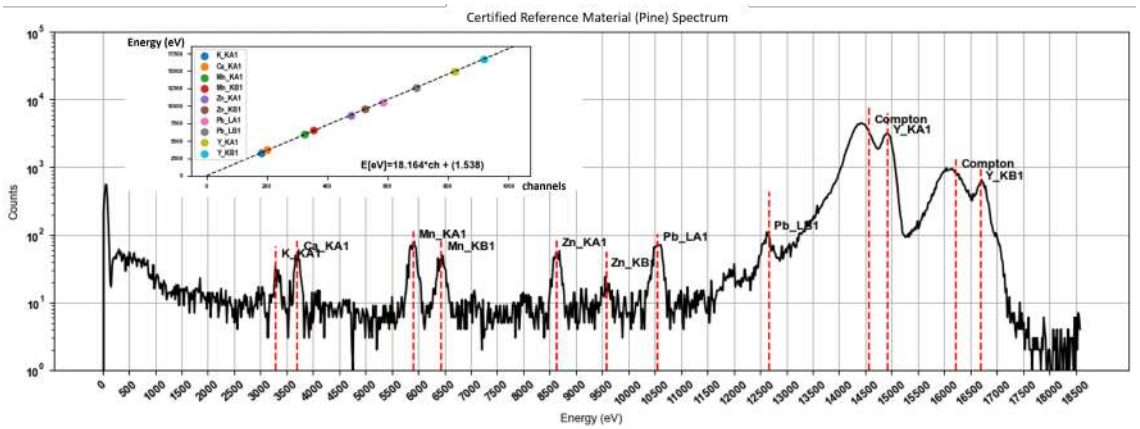

Figure 3.4: Peak labelling and energy calibration curve of the spectrum obtained from the analysis of the Standard Reference Materials 1575a: Pine Needles - *Pinus taeda* from *NIST Database*. The analysis was made using an Yttrium (Y) secondary target.

An accurate peak labelling is imperative at this point in order to proceed with further analysis, like element quantification. An incoherent labelling will cause paradoxical data

at the beginning of the quantification. An example of such a scenario would be: identifying characteristic Kβ lines of Cu without any evidence of Cu Kα lines, or the same with Lβ lines without Lα since there should be a correlation between them: α transitions are always at least two times more likely to occur.

3.3 Individual and Overall Peak Fitting

Up to this stage, several important tasks were already completed, including identifying centroids for the characteristic X-rays. These lines are linked to the corresponding electronic transition of a certain atomic species, enabling the precise calculation of an energy calibration curve. An analysis of an X-ray spectrum would not be possible without the described steps. Peak fitting is the next and the first major set of calculations to be performed, by doing it we define a curve that modulates each peak, allowing us to integrate them in order to know what is the area underneath. The area defined by a peak is the number of measured X-rays corresponding to a characteristic transition, this is valuable information for further quantification techniques.

Gaussian Fitting

When detecting photons with a certain energy, their interaction with the detector will cause an energy broadening of the detected signal. This phenomenon is due to several events that are generally well known in the physics community [38]: thermal broadening, caused by thermal fluctuations of the atoms in the sample leading them to emit X-rays with slightly different energies; natural broadening, which can be explained as an inherent energy uncertainty of the emitted X-rays since excited states may have short differences in lifetime; instrumental broadening, that can be simply explained by the energy resolution of X-ray detectors. These natural and instrumental limitations broaden the signal from multiple well-defined energy photons into a *Voigt* profile. Since our resolution cannot distinguish, with high resolution, the difference between a *Voigt* profile and a simple *Gaussian* shape, this last will be assumed (equation 3.1) given its simplicity and similarity to the *Voigt* profile.

$$Gaussian(x) = \frac{G}{\sigma\sqrt{2\pi}} \times exp\left\{\frac{-(x-x_0)^2}{2\sigma^2}\right\} \tag{3.1}$$

This expression gives us a normalized *Gaussian* curve (for G=1), where σ represents the full width at medium height (FWMH), G defines the gain of this curve and x_0 represents the channel corresponding to the centroid of the *Gaussian*.

Non Gaussian Fitting

As previously mentioned in subsection 3.1 and accordingly to the spectrum illustrated in figure 3.1, peaks from *Rayleigh* scattered characteristic X-rays can be assumed to have a

Gaussian shape. However, there is a set of equally important peaks, the *Compton* scattered ones, whose shape is manifestly different from a *Gaussian* profile. In order to understand the physical phenomenon behind the photon energy distribution that makes this disturbed *Gaussian* shape, it is necessary to reiterate that the *Compton* interaction leaves photons with different energies according with the measuring angle. In this case, the measured photons are collected with a scattering angle of 90°, so the expected energy for inelastic scattered X-rays is given by equation 3.2.

$$E_X^c = \frac{E_X}{1 + \left(\frac{E_X}{m_e c^2}\right)(1 - cos(\theta)} \quad \xrightarrow{\theta=90°} \quad E_X^c = \frac{E_X}{1 + \left(\frac{E_X}{m_e c^2}\right)} \tag{3.2}$$

Due to some uncertainty in the scattering angle and energy deviations, not all scattered X-rays that are measured will have energy equal to E_X^c, otherwise a *Gaussian* shape would arise. Consequently, a smooth yet significantly decreasing of the *Gaussian* shape will take place for lower energies than E_X.

A problem arises from this observation: Can a *Gaussian* profile be used to fit these signals? If so, is this approximation leading to considerable fit and quantification errors? Are there significantly better and equally simple distributions to replace the *Guassian* function in such peaks?

Some efforts have been made to better fit such peaks. Most of them sought to modify the standard *Gaussian* profile by adding a soft decay on curve [39]. Derived from analogous approaches, *VerX* proposes a not yet so commercialized distribution to fit *Compton* peaks: an EMG, adding to the pure *Gaussian* distribution an exponential decay on the lower energy side (left side of the *Gaussian* centroid). The equation of this curve is presented in equation 3.3.

$$EMG(x) = G\frac{\lambda}{2} exp\left\{\frac{\lambda}{2} 2\mu + \lambda\sigma^2 - 2(-x + x_0)\right\} erfc\left\{\frac{\mu + \lambda\sigma^2 - (-x + x_0)}{\sqrt{2}\sigma}\right\} \tag{3.3}$$

Where G is a multiplicative factor, λ is a coefficient that determines the slope of the exponential decay, σ represents the width of the peak, x_0 is the centroid of this modified *Gaussian* and *erfc* is the complementary error function. The application of such function in peak fitting is not groundbreaking. However it is not widely seen in most of the industrialized software. Using these two profiles, *Gaussian* and *EMG*, we were able to fully characterize any XRF spectrum. A demonstration of the similarity of the *Gaussian* and *EMG* curves to the Rayleigh and Compton peaks, respectively, can be observed in figure 3.5

Peak Fitting Algorithm

Having discovered the peaks positions and the potential natures they manifest, the remaining task before applying a fitting algorithm is to establish which of the discovered peaks are in fact to be fitted with a *Gaussian* of *EMG* curve. This task shall be performed

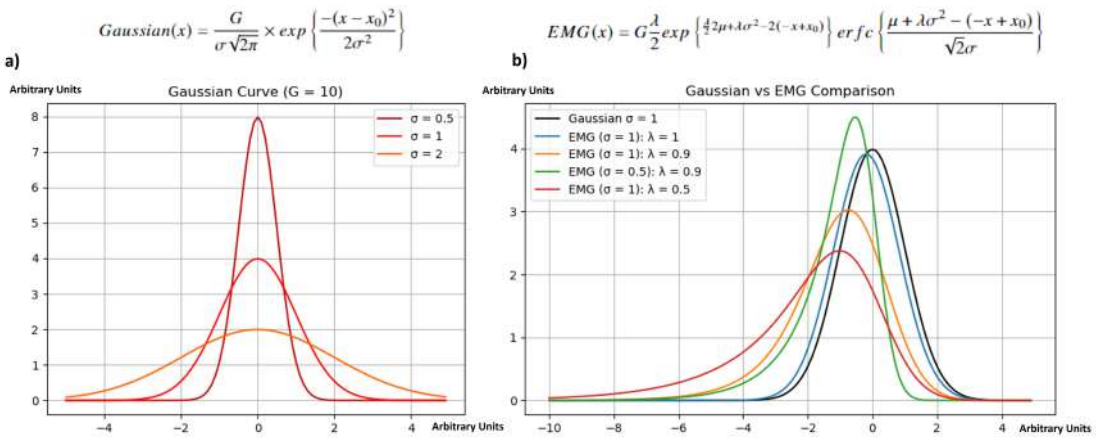

Figure 3.5: Comparison of the *Gaussian* and *EMG* curves. a) Comparison of different *Gaussian* curves with different values of σ but with the same area. b) Comparison between a *Gaussian* curve (in black) and different *EMG* with decreasing values for λ and σ.

manually in order to achieve greater freedom during the analysis. By defining their nature it is attributed an individual model at each peak and are constrained some of the parameters that compose either the *Gaussian* or the *EMG*, such as the centroid (x_0), the width σ, or the slope λ in the case of *EMG*. The initial values for the parameters of each model are at this point set and the fitting process is then initiated.

The application of the algorithm involves utilizing the *lmfit* library [40]. *lmfit* is a Python library that offers a high-level interface for non-linear optimization and curve fitting problems. This library is inspired by algorithms, already implemented by the *scipy* library [41], and it provides numerous enhancements to optimization techniques and data fitting tasks, such as support for parameter constraints, and the ability to handle uncertainties. These particular features are fundamental since all the curves have physically meaningful parameters from which values must not diverge.

Lmfit also contains an interesting feature for spectra analysis that allows a partitioned treatment of the peaks. Each identified and characterized peak is taken as an individual model, either *Gaussian* or an *EMG* model, with its characteristic parameters and constraints. All the models are then summed in order to best fit deconvoluted but mainly convoluted peaks. By doing so, the algorithm makes use of non-linear regression methods to reach the best combination of parameter values that best fit the spectrum. The returned values can then be used to replicate the individual peak, making the integration process much more intuitive and easy. In figure 3.6 there is an example of a fitting made for a rather simple spectrum and in figure 3.7 there is another example made for a complex spectrum featuring some extremely convoluted peaks.

There are spectra in which the decision between fitting a spectrum with *Gaussian* curves only or using *EMG* to fit *Compton* peaks has a bigger impact than in others. Taking the example of the spectrum used in figure 3.4 and focusing only on the *Compton* peaks, there is a considerable difference between the two mentioned approaches. Figure 3.8

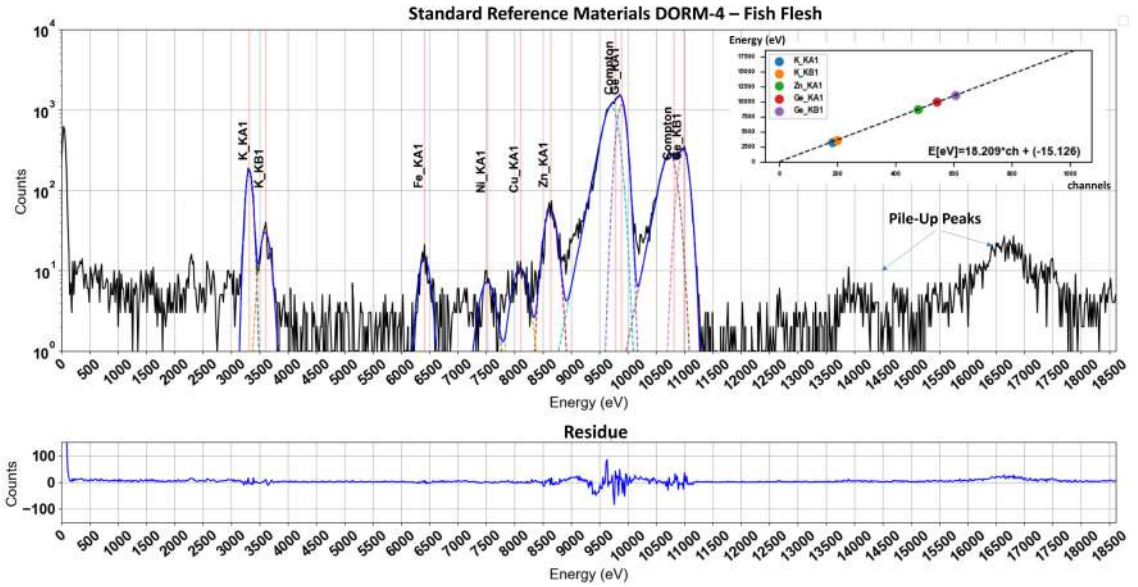

Figure 3.6: Example of the fitting analysis and energy calibration curve performed for the sample DORM-4 (Fish Flesh) using a setup with a Ge secondary target. Characteristic X-ray peaks are fitted using a *Gaussian* curve while Compton peaks are fitted with an *EMG*, resulting in an insignificant fit residue.

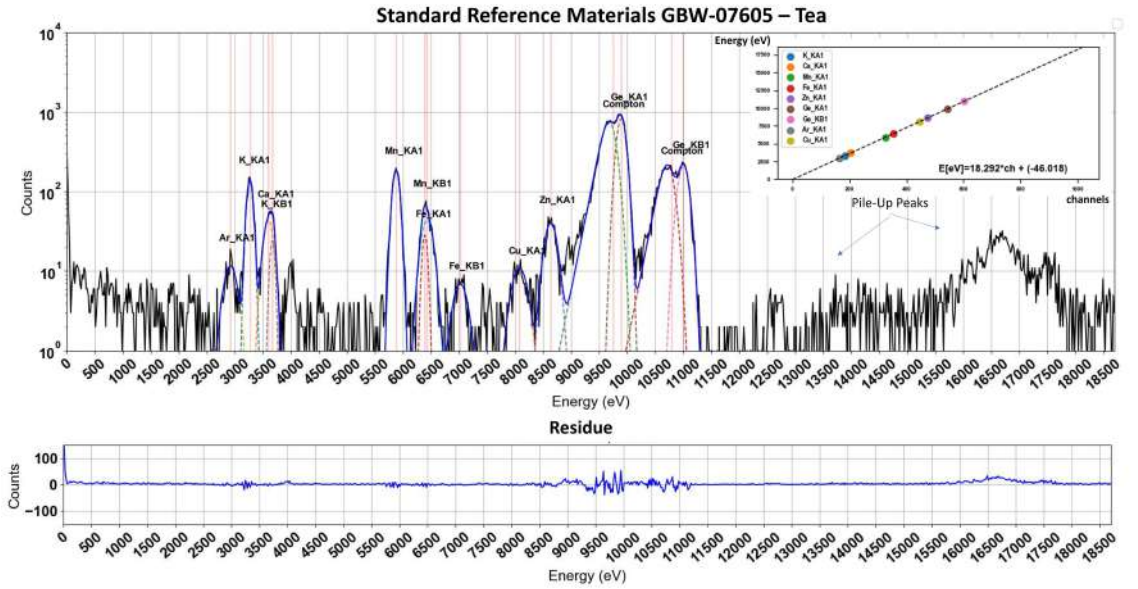

Figure 3.7: Example of the fitting analysis and energy calibration curve performed for the sample GBW-07605 (Tea) using a setup with a Ge secondary target. There are two couples of entirely convoluted peaks, that are then separated into two well-defined curves, ready to be integrated.

shows two fits: in red, a is fit performed using only *Gaussian* curves; in blue, a fit using *Gaussian* curves and *EMG* curves on the *Compton* contributions.

Figure 3.8 is a representative case of the positive impact of considering *EMG* curves to fit *Compton* contributions. Analysing and comparing the residue that the blue and the

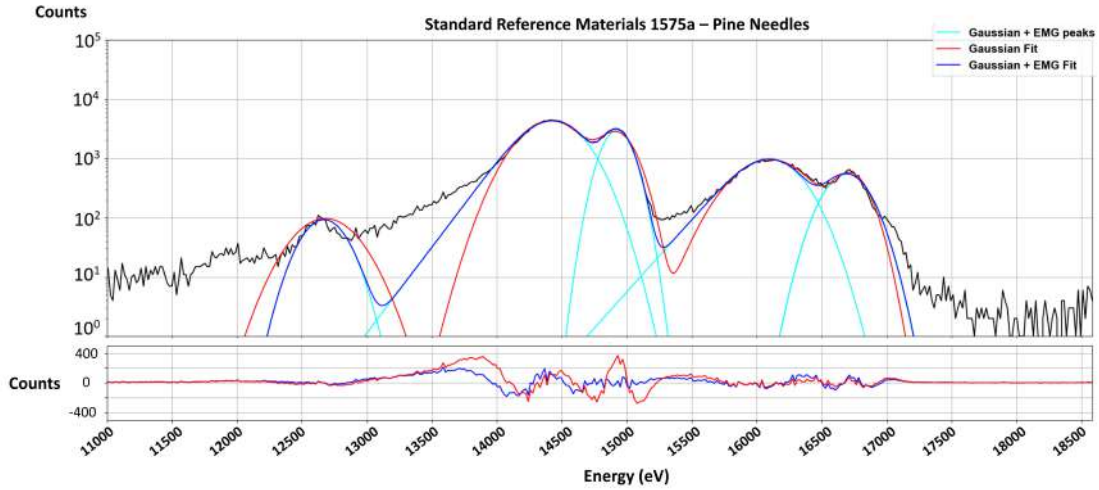

Figure 3.8: Example of the fitting analysis sample Standard Reference Materials 1575a Pine Needles using a setup with a Yttrium secondary target. In red, a fit is performed using only *Gaussian* curves; in blue, a fit using *Gaussian* curves and *EMG* curves.

red curve present, we conclude that the *Gaussian+EMG* fit is better, since the residue of the fit using only *Gaussian* curves is considerably bigger, sometimes hundreds of times bigger, than the *Gaussian+EMG* fit. This difference will only get bigger and bigger with the increase of statistics, indicating that the approach *Gaussian+EMG* fit is an improvement that needs to be taken into account.

3.4 Peak Integration

The spectrum analysis gets completed once the number of X-rays corresponding to each measured X-ray transition is known, this information is usually acquired by numerically integrating the individual deconvoluted peaks. However, this process will be simplified in our spectrum analysis for the majority of the peaks. Since all the peaks are normalized, *Gaussian* and *EMG* curves have a gain factor, the integral of these curves can be fortunately taken as the already calculated G factor for each *Rayleigh* peak.

An example of the processes explained until this point is presented in figure 3.9 along with the area under each curve.

3.5 Quantification Algorithm

The quantification process is a non-linear optimization problem in which, through an iterative process, a set of variable parameters (C_i and I_0) needs to be worked out in order to achieve a minimal error between a set of measured points (Y_i) and a set of calculated points (I_i) that are functions of C_i (concentrations of the sample elements) and I_0 (approximated intensity of incident X-rays on the sample).

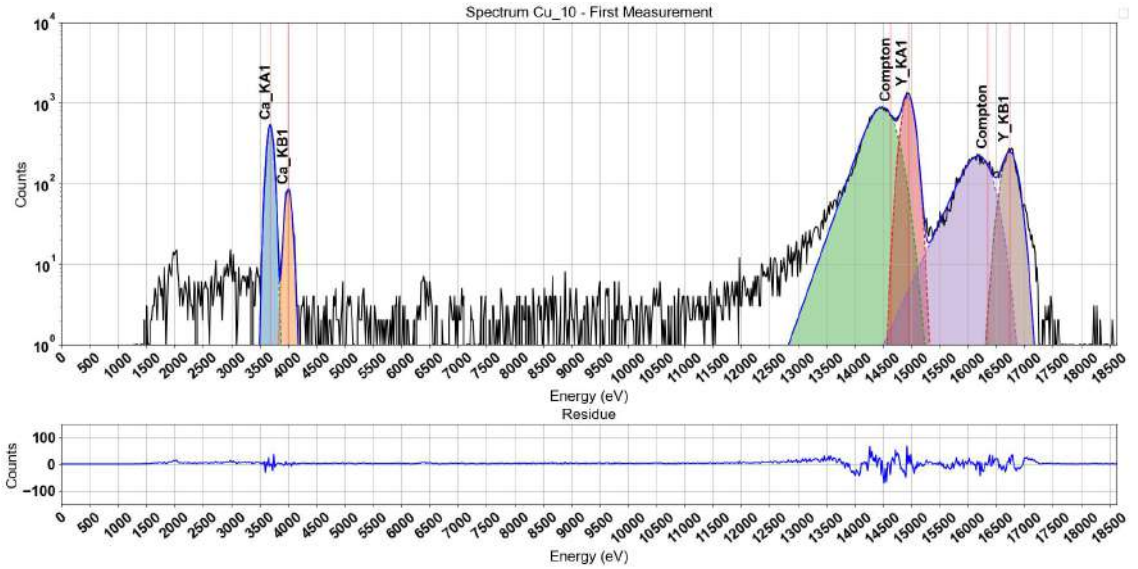

Figure 3.9: Example of the integration analysis on Hydroxyapatite ($Ca_{10}(PO_4)_6(OH)_2$) sample pellet using a setup with a Yttrium secondary target. The area is taken as the gain factor G of each normalized peak and the uncertainty calculated during the fitting process.

Quantification Theory

There are several approaches that could be taken as already exposed in the introduction. The method chosen for this analysis is meant to be a standard-free quantification method, only dependent on the fundamental atomic parameters of each element and on the setup. Consequently, it is computationally expensive and holds a deeper understanding of atomic theory from which were developed equations that try to calculate the rate of produced characteristic X-rays as a function of: the element concentrations in the sample, geometrical coefficients, atomic parameters and matrix effects, as has been thoroughly contemplated and theorized [15, 30, 33]. For this particular application, it will be adapted the theory presented by Marek Lankosz [42]. Equation 3.4 is a simplified function that gathers all the physical phenomena to mimic the number of X-rays that we measure in the spectra in order to achieve the best possible set of arguments that minimize the error to the measured values of K_α characteristic X-rays. Knowing these optimal values of element concentration the sample gets quantified.

$$I_i(I_0, C_i) = G_i K_i C_i F_i(I_0, C_i) \tag{3.4}$$

The number of detected X-rays characteristic of an element i is proportional to the detectors efficiency and geometrical factors (G_i), to an excitation factor (K_i) given by equation 3.5, to the element concentration C_i (the value is normalized between 0 and 1) and to F_i that expresses phenomena related to mass attenuation processes within the sample and energy absorption.

$$K_i = \frac{(r_i - 1)w_i f_i}{r_i} \tag{3.5}$$

The above equation 3.5 exploits the excitation factor K_i where, for a given chemical element, r_i is the jump ratio, w_i is the fluorescence yield and f_i is the transition probability.

The quantity F_i (eq.3.8) needs to be calculated for each characteristic transition that will be quantified and it is composed of two contributions: one referred to the secondary target K_α X-rays (F_{ai} eq.3.6) and the other to the secondary target K_β X-rays (F_{bi} eq.3.7).

$$F_{ai} = I_0(E_\alpha)\tau_i(E_\alpha)\frac{1 - exp\{(\mu(E_\alpha) + \mu(E_i))x\rho\} \times csc(45°)}{\mu(E_\alpha) + \mu(E_i)} \tag{3.6}$$

$$F_{bi} = I_0(E_\beta)\tau_i(E_\beta)\frac{1 - exp\{(\mu(E_\beta) + \mu(E_i))x\rho\} \times csc(45°)}{\mu(E_\beta) + \mu(E_i)} \tag{3.7}$$

$$F_i = F_{ai} + F_{bi} \tag{3.8}$$

It is noteworthy that by E_i it is evoked the energy of the characteristic X-ray in analysis and by E_α and E_β it means the energy of the K_α and K_β X-rays coming from the secondary target. Each of the contributions of the F_i factor quantifies how much the secondary target X-rays are attenuated within the sample given its depth (x), density (ρ), also knowing the mass attenuation coefficient of the sample for the secondary target X-ray energy ($\mu(E_{\alpha/\beta})$ and the photoelectric absorption coefficient ($\tau(E_{\alpha/\beta})$). The attenuation of the emitted characteristic X-rays needs also to be taken into the equation through the mass attenuation coefficient of the sample for the characteristic X-ray energy ($\mu(E_i)$). The sum of these two contributions (F_{ai} and F_{bi}) will add up to the equation 3.8. It must be noted that the F_i factor is directly affected by the concentration of the elements in the sample since it depends on the mass attenuation coefficients and these are functions of the mentioned element concentration as shown in equation 3.9.

$$\mu(E) = \left(1 - \sum_i^n C_i\right)\mu_{dm}(E) + \left(\sum_i^n C_i\mu_i(E)\right) \tag{3.9}$$

The mathematical approximation to compute the mass attenuation coefficient of a sample, given its constitution, is to make a weighted average of the mass attenuation coefficient concerning an hypothetical dark matrix (μ_{dm}), which is composed of light elements invisible to the spectrum, and the same parameter for each measured element. These coefficients were all either directly gathered from *NIST Database* [36], from *xraylib* library [43], from other cientific publications [44] or calculated and modified within the quantification iterative process.

Approximations

The presented theory aims to describe how fundamental parameters and experimental setup can be modulated to best simulate the physical phenomena behind the fluorescence

X-ray emission and all the other processes involved. However, achieving a flawless modulation of reality is nearly impossible. There are approximations that need to be taken so the quantification method can be computationally viable.

By admitting this theory we are not taking into account the commonly termed *Matrix Effects*. These effects can be synthesized into the interactions that characteristic X-rays have with other elements of the sample. These interactions are probabilistic and will surely modify the measured signal of the element that emitted the photon. There are two possible observations: either the characteristic X-rays have sufficiently high energy to ionize another element of the matrix stimulating the emission of a different characteristic X-ray (second-order ionization), or the characteristic X-rays do not have enough high energy and get absorbed by the matrix. These phenomena will create a misleading idea that some elements may have a higher or lower concentration given the false increase, or decrease, of measured photons which first provenience was from other elements. We are aware of these effects, studies aiming to understand its impact were developed for a diversity of samples [20].

Nevertheless, are considered mass attenuation phenomena resulting from light elements invisible to the analysis technique. This consideration is taken in equation 3.9 through the μ_{dm} factor. These interactions are the only ones that are considered concerning the influence of matrix elements. Still, even this consideration may be incomplete given the number of possibilities (combinations of the element concentrations in the sample) for optimal quantification. To overcome this problem and simplify it, the dark matrix is always provided by the software user. This can be done either through manual input of the matrix composition or by selecting a matrix from the *NIST* database [36]. In either case, the concentration of matrix elements remains constant in the quantification.

Optimization Method

The essence of the theory can be outlined by equation 3.4 and the optimization problem can be graphically represented in figure 3.10.

By looking at the data as if the measured points (in orange) represent a curve that needs to be fitted by a set of initial points (in blue) by changing the concentrations (C_i) and the intensity (I_0), then quantifying a sample through this technique is no different from any other non-linear optimization problem including the way the error (χ^2) is calculated (equation 3.10).

$$\chi^2 = \sqrt{\sum_i^k (\Delta_i)^2} \quad \xrightarrow[\text{with 3.10}]{\text{according}} \quad \chi^2 = \sqrt{\Delta_{Ag}^2 + \Delta_{Fe}^2 + \Delta_{cu}^2 + \Delta_{Zn}^2} \tag{3.10}$$

The pursuit for the set of parameters that minimize the χ^2 is unclear and will face several potential ideal combinations of these parameters. This is explained by the high amount of fit parameters when compared with the number of points to be fitted, also the complexity of the problem and the several approximations can play a role in the distortion

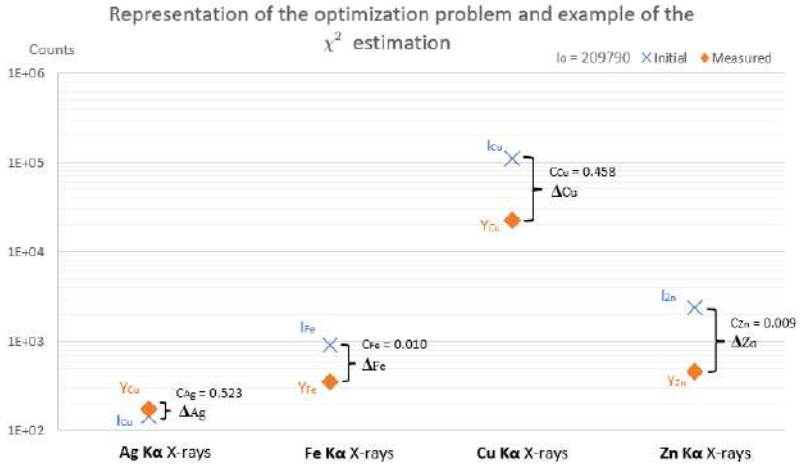

Figure 3.10: Graphical representation of the optimization of an exemplary sample containing silver (Ag), copper (Cu), Iron (Fe) and Zinc (Zn). The data that needs to be fitted (Y_i) by the theoretical calculated intensities (I_i) when changing the optimization parameters (C_i and I_0) are equivalent to the points of a curve in curve fitting problems.

of the absolute best set of parameters. Still, optimal values exist and can be reached with a powerful and clever algorithm capable of recognizing the most efficient perturbations to previous sets of parameters in order to achieve more accurate values that lead to the minimal χ^2.

The chosen non-linear optimization method was developed independently by Kenneth Levenberg in 1944 [45] and by Donald Marquardt in 1963 [46], later their efforts have been merged into the *Levenberg-Marquardt Algorithm* (LMA) presenting an ability to rapidly discard sets of values with high χ^2 and reach decreasing values χ^2. This behaviour is accomplished by a combination of two simpler numerical optimization algorithms: the *Gradient Descent Method* (GDM), in which the improvement of the parameters follows the opposite way of the function gradient (the decreasing orientation of χ^2), computed through a small perturbation; and the *Gauss-Newton Method* (GNM) that assumes that the objective function is locally quadratic allowing it to be easily approximated via first-order Taylor series expansion.

The combination of these two methods simply relies on adjusting the parameters update between one method and the other, using the GDM update technique when the algorithm reaches high χ^2 values and the GNM update technique when dealing with the imminence of a local minimum. This method counts with uncontable implementations in a wide range of programming languages, one of them was presented in 2023 by Henri P. Gavin in Python [47]. This implementation will be adapted in our software. Mathematically, the algorithm can be summed into one equation (equation 3.11), where λ is a weighting parameter used to settle the mathematical approach to the optimization.

$$h_n = -\left(\nabla^2 f(x_n) + \lambda I\right)^{-1} (\nabla f(x_n)) \tag{3.11}$$

$$h_n \approx -(\lambda I)^{-1}(\nabla f(x_n)) \quad when \quad \lambda \to \infty \tag{3.12}$$

$$h_n \approx -\left(\nabla^2 f(x_n)\right)^{-1}(\nabla f(x_n)) \quad when \quad \lambda \to 0 \tag{3.13}$$

The balance between using the GDM and GNM way of calculating the set of perturbations (h) to update the parameters is settled by λ: a greater λ gives more importance to the GDM technique of calculating h, with small values steps (equation 3.12); an infinitesimal λ approximates the technique to the GNM (equation 3.13).

Despite the substantially increased complexity of dealing with a combination of two methods, it improves significantly the optimization convergence. To visualize the behaviour of the LMA, let us consider an analysis of a sample containing only three quantifiable elements (elements A, B and C). A surface plot expressing χ^2 as a function of (C_A, C_B, C_C) can be performed allowing a visual representation of the locals and absolutes extremes of the surface. Considering that there is the constraint of all the concentrations adding up to 1, such a plot can be performed using the C_A and the C_B as the independent variables in a $[0,1]\times[0,1]$ space. If $C_A + C_B < 1$, then C_C is regarded as $C_C = 1-(C_A+C_B)$, otherwise $C_C = 0$ and the sample is composed only by element A and B. Coordinates of which the sum is above 1, are not valid. An example of such a surface plot is given in figure 3.11.

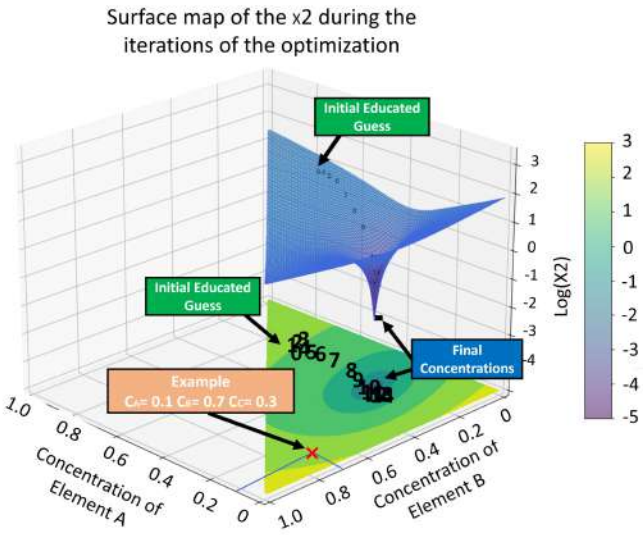

Figure 3.11: 3D surface plot of the χ^2 calculated using the simulated intensities (I_i) and the measured X-ray K_α intensities (Y_i) for different combinations of element A, B and C concentrations. The surface map shows a clear absolute minimum which is reached after around 14 iterations (iterations are represented as the respective number on the plot). The curve domain excludes all the concentration combinations that exceed a sum of 1, showing a triangle in the $C_A \times C_B$ plane.

When reaching a region in the χ^2 surface with a low gradient, the curve can not be approximated to a quadratic function, leading to an increase of λ in order to find

quickly the way of a minimum. Once a greater gradient is achieved, λ is decreased slowly approximating the curve to a quadratic function meaning that this optimization will be more accurate and faster towards a minimum.

There are three convergence criteria in which the algorithm decides to stop searching for a better set of parameters and calls it an end:

1. **Convergence in the gradient**: When the gradient value is low and the alteration to the parameters does not affect significantly the gradients value.
2. **Convergence in the parameters**: When the difference between the best parameters so far and new attempts to improve them is infinitesimal.
3. **Convergence in iterations**: A previously defined number maximum of iterations is reached without any of the above criteria being fulfilled.

For a final concise and compact illustration of the quantification process, it is presented in figure 3.12 a diagram simulating the quantification processes on a centenary coin from the XV century with real values obtained throughout the quantification.

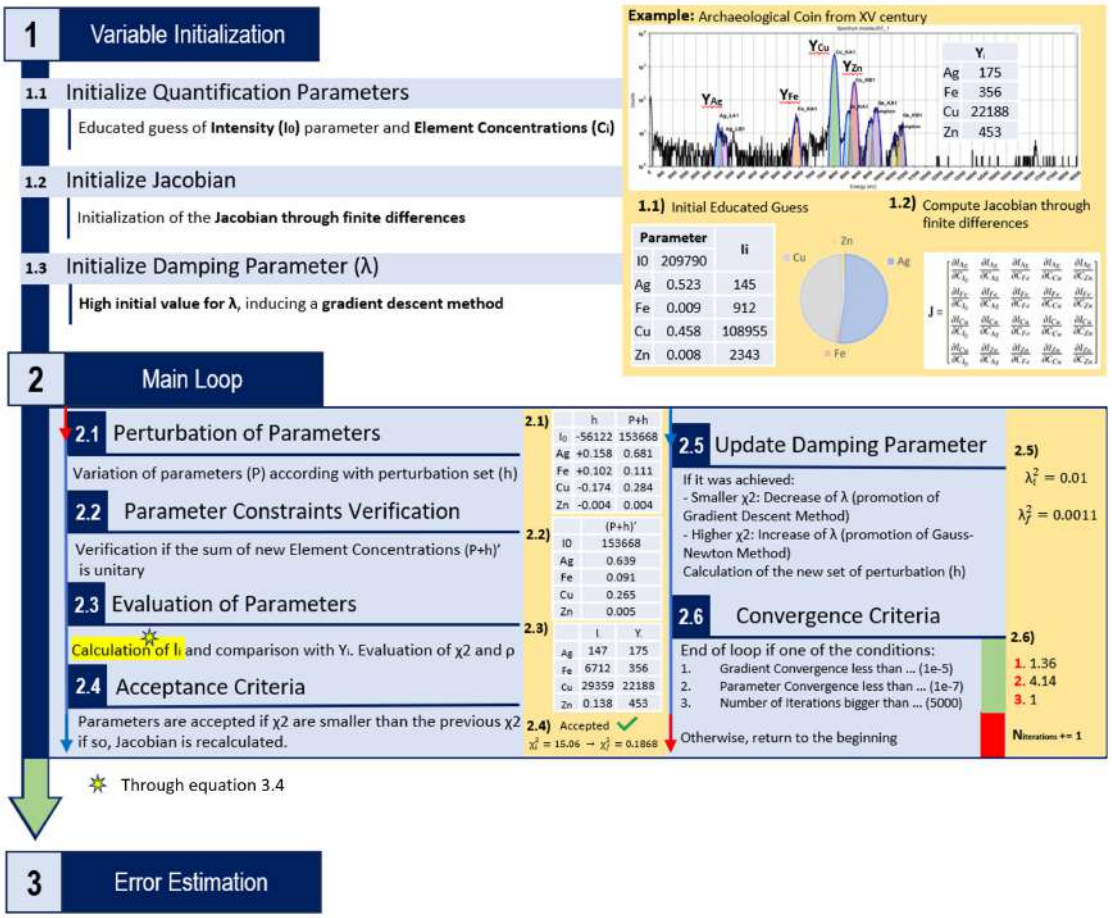

Figure 3.12: Diagram succinctly explaining the quantification steps using *Levenberg-Marquardt Method* applied on an archaeological coin from the XV century. The process starts with an initialization of variables (1) including an educated guess of the parameters and the λ damping parameter; then gets into a loop (2) where the parameters are perturbed according to a set of variations h defined by a combination of the GDM and GNM (2.1), the parameters are verified through a normalization (2.2), is then calculated χ^2 (2.3) and according to previously defined thresholds the new set of parameters may be accepted (2.4). A rethought of the importance of the GDM and GNM in the calculation of h (2.5) will then take place according to the χ^2 achieved, lastly the parameters, gradient and number of iterations undergo verification (2.6). Once the convergence criteria are matched, the loop stops and the parameters are saved along with statistical errors.

Chapter 4

Case Study - Analysis of Cu+Ag+Zn Alloys - Results and Discussion

To furthermore validate the software **VerX** and the method presented by it, a case study was taken and the results that emerged from its analyses are discussed below. There are two kinds of results to consider: the first kind that arises from fitting a spectra with the best adequate peaks (type of mathematical function and parameters), making the correct labelling and an assertive counting of the area underneath - Spectrum Fitting; and the quantification process, an iterative process seeking the absolute best set of element concentrations that reproduce the sample spectrum with minimal error - Sample Quantification.

The ideal case study would analyse a simple set of samples composed of metals with precise knowledge of their composition. Since metals can easily absorb X-rays with high fluorescence yield, most characteristic X-rays are detected and the dark matrix effect can be neglected. Concerning the dark matrix effect, an example of the type of sample to avoid when making a first-instance case study would be a biological sample given the high concentration of light elements invisible to the X-ray fluorescence spectra, such as carbon, oxygen or hydrogen.

4.1 Presentation of the set of samples

Given all the facts above described, the chosen case study was a set of samples made from metallic alloys containing fixed and residual quantities of Zn and varying quantities of Cu and Ag. These samples were ordered to a local jewelry craftsman who made these alloys with as much accuracy as possible, according with the concentration of Cu and Ag as follows ($\%Cu/\%Ag$): 10/90, 20/80, 30/70, 50/50, 70/30, 80/20, 90/10, 95/5, 98/2. All the samples were previously analyzed and quantified using a commercial spectrometer: *M4 Tornado Micro XRF* from *Bruker Corporation*. This preliminary analyses gave us quantitative values as a control reference to quantify the set of sample, since this spectrometer has a well estabilished and functional quantification software built in. The set of samples

can be discerned as in table 4.1 by its given name and known composition given by the mentioned preliminary analysis.

Table 4.1: Table describing the compositions of Cu, Ag and Zn as an atomic percentage of the total. The names given to the samples follow a rule: Cu_X where X is the atomic percentage of Cu that the sample has, being $100 - X$ the quantity of Ag and residual quantity of Zn.

Element	Cu_{10}	Cu_{20}	Cu_{30}	Cu_{50}	Cu_{70}	Cu_{80}	Cu_{90}	Cu_{95}	Cu_{98}
Cu	8.809	18.817	28.024	47.838	70.479	80.584	89.699	95.042	98.280
Ag	91.163	81.139	71.917	52.076	29.405	19.294	10.292	4.949	1.710
Zn	0.028	0.043	0.059	0.086	0.116	0.122	0.009	0.010	0.010

The spectra were acquired within the scope of other research using the setup shown in figure 2.4 equipped with a Ge secondary target and were kept in a spectra database, they will now be used as a case study. During the spectra acquisition, each sample was measured twice (changing the irradiated spot between them) trying to discard any non homogeneity issue with the sample. It serves very well our purposes and allows us to test the fitting algorithm and most of all the quantification method, with a multi-element set of samples with well know variations in concentrations.

4.2 Example of the analysis - Cu_{10}

Once the spectra are acquired in a 3EDXRF spectrometer, the files must be converted into *.txt*, if they are not already, so **VerX** can open them and start the analysis. All the steps described in chapter 3 are carried out to ensure a correct spectrum fitting and counting of X-rays detected per peak. An example of the fitting performed by the algorithm is in figure 4.1.

Table 4.2: Table describing the intensities of the peaks found in figure 4.1.

X-ray Line	Energy (eV)	Channel	Integral (counts)
Ag_{LA1}	2966.85	165	437 ± 50
Ag_{LB1}	3133.42	175	402 ± 58
Cu_{KA1}	8043.93	443	3586 ± 29
Zn_{KA1}	8637.60	477	430 ± 34
Cu_{KB1}	8908.14	491	642 ± 33
$Compton$	9721.46	530	504 ± 69
Ge_{KA1}	9875.20	543	1257 ± 62
$Compton$	3133.42	590	162 ± 68
Ge_{KB1}	10991.70	604	187 ± 53

Upon concluding the fitting, the area defined by the K_α or L_α peaks of the characteristic X-rays (Ag_{LA}, Cu_{KA} and Zn_{KA}) is calculated and it is given to the quantification algorithm in order to start the iterative process.

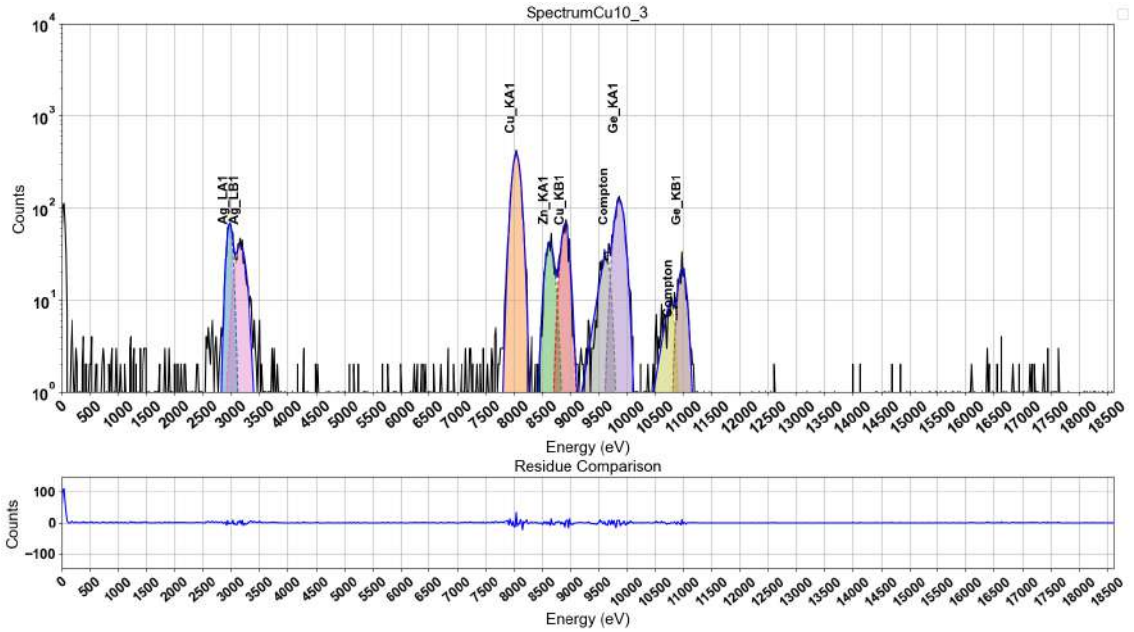

Figure 4.1: Example of the results obtained after the fitting algorithm analysis about sample *Cu_10* using the spectrum corresponding to the first acquisition.

A total of 18 acquisitions and their respective fitting analyses were made. In the samples whose concentration of Ag is higher, all of the peaks of interest are visible, as seen in 4.1. The ones with less Ag concentration do not present such a higher signal of Ag peaks as expected. Since Zn and Cu have higher fluorescence efficiency and absorption cross-section, the correspondent peaks show clearer evidence in all the spectra.

The convergence history of the quantification performed to the spectrum shown in figure 4.1 is detailed below in figure 4.2 as an example of how important parameters change over the iterations.

From figure 4.2, the convergence treshold is noticeable from around the 25^{th} iteration in a total of 32 iterations. The initial educated guessing (presented in the legend of subgraphs b) and c) with the indication *init*) is a great help to the quantification since it guides all the convergence towards the best local minimum of χ^2. In the first subgraph a), it is clear an overall decrease of the absolute difference between I_i and Y_i and that is even more obvious when analysing the last subgraph d), where χ^2 indeed reaches a minimum from where the values do not deviate until the end of the algorithm.

To pursue a better understanding of this particular result, a plot of the χ^2 for all possible combinations of C_{Cu}, C_{Ag} and C_{Zn} is shown in figure 4.3.

In fact, there is a clear minimum of the error χ^2 at the same combination of concentrations $C_{Cu} : C_{Ag} : C_{Zn} \rightarrow 0.017 : 0.981 : 0.001$ in both representations. The result obtained does not match accurately with the expected $0.10 : 0.90 : 0.00$ ratio, this will be explained in the next subsection.

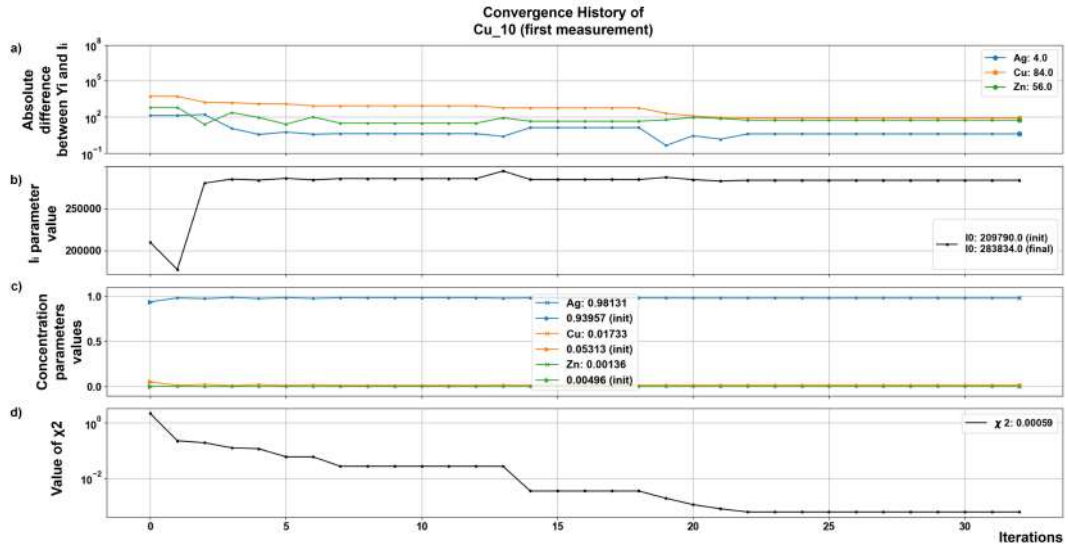

Figure 4.2: History of the parameters values over the iterations of the quantification (Convergence History). a) Absolute difference between I_i and Y_i; b) Value of I_0 parameter; c) Value of the parameters equivalent to the concentration of the elements in analysis; d) Value of the overall error (χ^2).

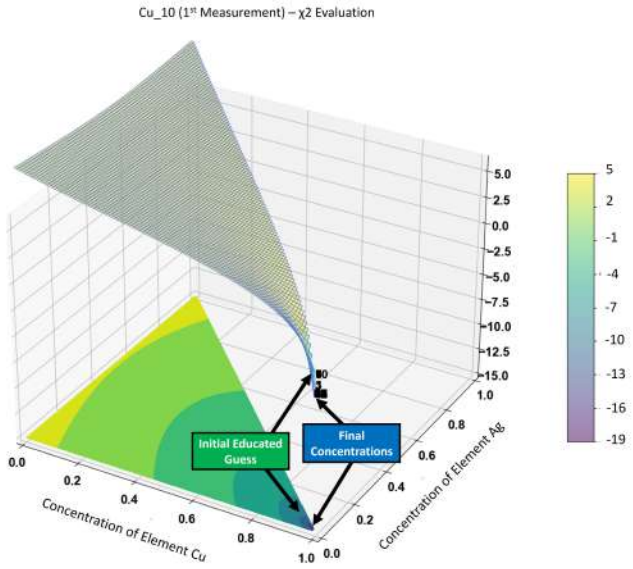

Figure 4.3: Illustration of the values of χ^2 for all the possible combinations of Ag, Cu and Zn.

4.3 Summary of Findings and Discussion

Repeating the process described in the previous section to all the spectra acquired using all the samples available, a similar arrangement of the table 4.1 was built using the quantification results obtained from the 18 spectra (table 4.3). Despite the initial guess of the parameters set (performed automatically by VerX), the density of the samples were approximated using values of density given by *American Elements* website [48] and they

were inputed into the software.

Table 4.3: Table describing the compositions of Cu, Ag and Zn as an atomic percentage of the total. Columns with the suffix *Avg* have the average of the results for each sample, these are the values of interest.

Name	C_{Cu}	C_{Cu} Avg	C_{Ag}	C_{Ag} Avg	C_{Zn}	C_{Zn} Avg
$1Cu_{10}$	1.73		98.13		0.14	
$2Cu_{10}$	1.83	1.78	97.92	98.02	0.25	0.19
$1Cu_{20}$	4.48		95.22		0.83	
$2Cu_{20}$	4.21	4.34	95.63	95.43	0.52	0.68
$1Cu_{30}$	5.96		93.92		0.13	
$2Cu_{30}$	6.66	6.31	93.14	93.53	0.65	0.39
$1Cu_{50}$	18.89		80.75		0.79	
$2Cu_{50}$	18.40	18.64	91.30	81.02	0.61	0.70
$1Cu_{70}$	29.12		70.45		0.43	
$2Cu_{70}$	28.25	28.63	71.39	70.92	0.46	0.44
$1Cu_{80}$	40.80		58.70		0.50	
$2Cu_{80}$	34.16	37.42	65.45	62.08	0.49	0.50
$1Cu_{90}$	73.90		22.69		3.41	
$2Cu_{90}$	72.82	73.35	24.35	23.52	2.84	3.12
$1Cu_{95}$	74.37		22.78		2.95	
$2Cu_{95}$	74.92	74.59	22.24	22.51	2.84	2.89
$1Cu_{98}$	75.57		21.51		3.02	
$2Cu_{98}$	74.50	73.98	24.17	22.84	3.33	3.175

Since the way of finding the above quantifications uses numerical algorithms, the obtained uncertanties are statistical and have no physical meaning to the study. Instead, there is an alternative way of estimating the uncertanties: by calculating the greatest deviation between the values from table 4.3 and the quantifications calculated using the value of the counts summed with the uncertanties associated. For example, when looking at the table 4.2, we try to calculate what are the maximum and minimum values of concentration of Ag and Cu: the maximum counts that we can assume for Ag is 437 + 50 (of uncertainty); the minimum counts we can assume for Cu is 3586 - 29 (of uncertainty); and Zn, since it has residual concentration plays no significant impact to the quantification. From this extreme scenario we achieve a quantification that deviates from the one originally obtained using the values from the table. We must perform a similar calculation to achieve the opposite extreme scenario (subtract uncertainty of Ag and sum the uncertainty of Cu). The biggest deviation in quantification that these extreme cases show is taken as the uncertainty of this quantification.

Despite the 18 acquired spectra, the relevant results taken from the table 4.3 are the average of the concentrations between the two measurements of the same sample. These values can be plotted in a more compact and visual way in a stacked bar chart shown in figure 4.4.

The results shown in figure 4.4 and table 4.3 are the culmination of the case study carried out using the described theory and the software VerX.

There is no overlap between the results obtained from VerX and from table 4.1, yet they show clear consistency: samples with progressively higher quantities of Cu, or Ag

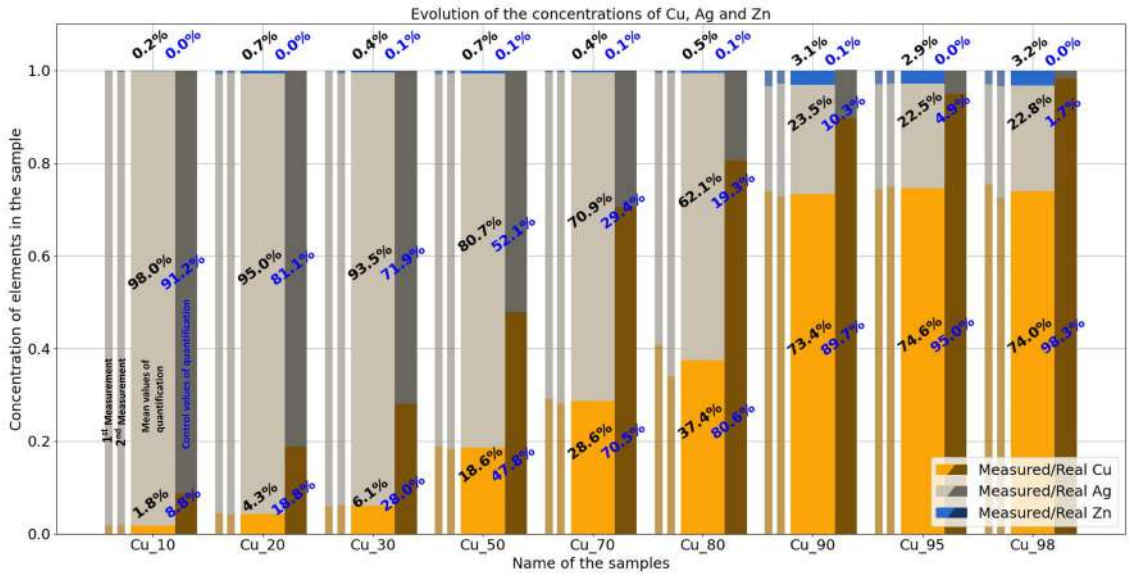

Figure 4.4: Stacked bar chart representing the quantification results. In each bin the quantification for the first and the second acquisitons of the correspondent sample (on the left and right correspondently) is represented. In the middle the average of these two quantifications. The described percentages correspond to the average of the quantifications performed for both acquisitons. Lighter colours correspond to measured values and darker colours to real values.

for instance, show higher quantifications of Cu. Nevertheless, results show deviations from the expected quantanties of Ag and Cu. These deviations are translated into relative errors between 18% and 83%, depending on the sample.

Concerning the individual and overall peak fitting, it is presented very low residues, under 1% of the measured counts, showing how VerX improves the way the spectra is analyzed through EMG curves. Regarding the integral of the peaks, the uncertainties are also low, depending on the number of data presented by the spectra the relative uncertainties can be higher or lower, yet they are usually under 10%.

The quantification data allows us to conclude that the algorithm used to calculate these results, presented in chapter 3, has the right methods of finding the absolute optimal concentration with the adapted physical model. In spite of the high errors, when comparing with the data from table 4.1, we came to the conclusion that these deviations occur because of approximations applied to the physical model. When considering that characteristic X-rays are not absorbed by other atoms from the sample we are not considering the amount of characteristic X-rays from Cu that are lost at the same time that enhance the amount of detected characteristic X-rays from Ag. This phenomenon, explained in section 3 (in *Approximations* subsection), has a higher probability of ocurring when the energy of the absorbed X-ray is closer (but always higher) than the emitted characteristic X-ray, which the case with Cu and Ag K_α X-rays. This is not a isolated phenomenon, it can occur multiple times with the same first emitted X-ray if there are consecutively less energetic levels to be excited, creating n^{th} order fluorescence and

mischaracterizing the quantification. Another strong evidence of this conclusion, is the improvment of the accuracy with samples with less concentration of Ag. If the Ag atoms are the main responsibles for the attenuation of Cu K_α X-rays, with higher concentrations of Ag the quantification is the worst (samples with $30 < C_{Ag} < 95$) and gets much better when the concentration of Ag is under 30%.

In appendix A, there are all of the 18 spectra acquired for this case study along with the fitted peaks and a table summarizing the results for each spectrum.

The methods presented throughout this thesis have been already tested in some other context: studying the improvment of quantification methods (using certified reference materials) when using EMG curves to fit *Compton* peaks. This study shows an overall upgrade of the previous methods and allows the creation of quantification curves with less uncertainty. Such impact in research will be published in the *X-Ray Spectrometry* journal with the name *Improvement of Quantification Curves Using Exmponential Modified Gaussian Curves to Fit Compton Peaks*.

Chapter 5

Conclusion

5.1 Conclusions

Having tools able to conduct analyses in a non-destructive way is a priority nowadays and the reasons behind it can be multiple: either the samples are rare and hard to produce, or it may be necessary to perform multiple analyses using different physical principles, or even the set of samples have cultural value and simply can not be destroyed. Such reasons motivate a rigorous search for a technique that can take the most information out of few data acquisition in a non-destructive manner. The method described in this thesis entirely fulfills the outlined demands.

By investing in XRF spectrometers it is possible to rapidly identify a wide range of elements that compose the samples, making it a technique suitable for preliminary analyses but also for more comprehensive ones. These characteristics are outlined by the way the 3EDXRF spectrometer is connected to the (WDXRF) DCS, making it exceptionally easy to make either quick analyses or highly detailed ones. More than identifying elements, it was presented a functional method of levering EDXRF analyses and make use of a physical model to quantify these elements in the sample. Concerning the triaxial geometry, a highly pertinent attribute of the 3EDXRF spectrometer is the noise removal from the spectra it acquires. This feature upgrades the XRF classical techniques and leads the way for further complex analyses like quantification.

In summary, this dissertation presents recent developments on two dimensions of EDXRF spectrometry: at the apparatus level, a system composed of a 3EDXRF spectrometer and a DCS are nearing completion allowing interdisciplinary scientific research that lead to a significant range of results with distinct natures, having the possibility of cross-validating hypotesis; and at data processing, by taking XRF spectra and modelling the reality (always caring for the considered approximations) it was possible to find meaning in the peaks that spectra present and integrate that information with the physical model and non-linear optimization algorithms in order to produce a versatile software capable of quantifying samples.

The presented solution for data analysis has the name *VerX* and aims to perform

sample quantification. The algorithms that have already been elaborated upon and form the foundation of VerX are:

1. Peak Identification: It is identified which channels accomodate X-ray peaks.
2. X-ray Lines Labelling: From the identified peaks, it is built an energy calibration curve in order to label them with the correct X-ray line, identifying the elements that compose the sample.
3. Peak Fitting: To proceed with quantification, each peak is fitted with a curve to resolve the spectrum. The vast majority of software consider gaussian curves to resolve each peak, but *VerX* uses a combination of gaussian and EMG curves depending on the physical origin of the peak. This is one of the main features of the software.
4. Peak Integration: Having curves that resolve the spectrum, it is calculated how many photons were detected from each element.
5. Quantification: From all the previous data it was built a physical model, that approximates the reality by simplifying it. Using an adaptation of the LMM, we tried to find what are the conditions (concentration of elements in the sample and setup parameters) that best replicate the spectrum obtained.

An important aspect of the software is the user-data interaction, so it was developed an intuitive frontend that shows the data throughout the above steps in order to enhance the clarity and reliability of the analyses. The way the results are presented and stored for further discussion is a distinct advantage, additionally it can also be personalized. The software frontend is presented in appendix 5.2.

Case studies have tested these methods and have shown which are the sucesses and the aspects that require improvment. Concerning the algorithms that prepare the data for quantification, *VerX* is capable of taking complex spectra with many overlapping peaks and resolve them with well defined uncertanties and low errors, showing that the proposed objetives have been fulfilled. The quantification process represents a great starting point for a more complex model to be taken into consideration, results have shown that the method shows consistency, the quantification does not contradict the known information about the samples, but lacks complexity in the way it models reality, showing errors that can reach tens of percent in concentration.

5.2 Future Perspectives

Over the course of this dissertation there were aspects that emerged with particularly need for improvment and continuity. Some of them required more time to be developed, others arose from the results of the case study. The main aspects I would like to carry on are:

1. Conclusion of 3EDXRF spectrometer: Despite being in its final steps, the 3EDXRF spectrometer is not yet ready for spectra acquisition. The sample holder and the secondary target support needs to be finalized and aligned in order to achieve a rigorous triaxial path until the X-ray beam reaches the detector.

2. Improve the EMG curve: The EMG curve, used to fit *Compton* peaks in the spectra, is a major feature in the spectra analyses performed by VerX and its introduction as shown clear improvments on the peak fitting results. There is still room for upgrading the type of curve used, a deeper study on how the *Compton* phenomena modifies the energy of a beam of X-rays can be made in order to better fit the overall spectra and have more accurate quantifications.

3. Increase the complexity of the model: By considering secondary or even tertiary fluorescence by the atoms of the matrix we can take into some of the matrix effects that disrupted the results shown in the case study. Another possible way of reaching a more complete model is to take into account the characteristic K_β counts measured in the spectra for the quantification, instead of only the characteristic K_α X-ray. Despite the dark matrix effects being modeled, they can be reviewed on the considered physical model because they play a very important role in the analyses of lighter samples like biological samples, for instance.

4. Noise removal feature: The application of *VerX* in these circunstances do not need noise removal. However, by adding such a feature, a meaningful step is taken towards the application of *VerX* to non triaxial XRF spectra. Moreover, by adding a noise removal feature to the peak fitting techniques already proposed, the software have sufficient tools to be applied in other analyses techniques like PIXE, RBS, Auger spectrometry and alike techniques.

5. Improve the software interface and displayed results: Including the uncertainties of the quantification in the displayed results is important. The interface was developed using the *PySimpleGUI Python* library, a easy and quick way to make a sufficiently good interface. By using a more professional and frontend directed coding languages, the interface can be highly improved from the point of view of the user.

In a long perspective, during the development of some of VerX features, I concluded that there are a lot of algorithms that may benefit from artifically intelligent features for peak classification, such as: to distinguish the shape of the peaks in a spectrum, the parameters that define their FWMH, or also to identify the correct X-ray line that each peak present. Such implementation of artificial intelligent algorithms in the software may improve the its autonomy and accuracy.

Bibliography

[1] J. M. Lourenço. *The NOVAthesis LaTeX Template User's Manual*. NOVA University Lisbon. 2021. URL: https://github.com/joaomlourenco/novathesis/raw/main/template.pdf (cit. on p. i).

[2] *Encyclopedia of Spectroscopy and Spectrometry (X-ray Fluorescence Spectrometers)*. Elsevier, 2017, pp. 2467–2500. ISBN: 9780128032244. DOI: 10.1016/C2014-1-01729-2. URL: https://linkinghub.elsevier.com/retrieve/pii/C20141017292 (cit. on pp. 2, 3, 7).

[3] R. van (Rene) Grieken and A. Markowicz. *Handbook of X-ray spectrometry*. Marcel Dekker, 2002, p. 983. ISBN: 0824706005 (cit. on p. 2).

[4] V. D. Hodoroaba. *Energy-dispersive X-ray spectroscopy (EDS)*. Elsevier, 2019-09, pp. 397–417. ISBN: 9780128141830. DOI: 10.1016/B978-0-12-814182-3.00021-3 (cit. on pp. 2, 7).

[5] L. Martins et al. "Overview and calculation of X-ray K-shell transition yields for comprehensive data libraries". In: *X-Ray Spectrometry* 49 (3 2020-05), pp. 398–423. ISSN: 10974539. DOI: 10.1002/xrs.3123 (cit. on p. 2).

[6] P. Brouwer. *Theory of XEF : getting acquainted with the principles*. PANalytical BV, 2003, p. 71. ISBN: 9090167587 (cit. on pp. 2–8).

[7] R. Jenkins et al. "IUPAC—nomenclature system for x-ray spectroscopy". In: *X-Ray Spectrometry* 20 (3 1991-06), pp. 149–155. ISSN: 0049-8246. DOI: 10.1002/xrs.1300200308 (cit. on p. 2).

[8] M. F. Vitha, R. Klockenkämper, and A. V. Bohlen. *TotalReflection XRay Fluorescence Analysis and Related Methods*. Ed. by R. Klockenkämper and A. von Bohlen. Wiley, 2014-12. ISBN: 9781118460276. DOI: 10.1002/9781118985953. URL: https://onlinelibrary.wiley.com/doi/book/10.1002/9781118985953 (cit. on p. 3).

[9] R. Roque. "X-ray imaging using 100 mum thick Gas Electron Multipliers operating in Kr-CO2 mixtures Optimization of a large area Zero-IBF for ionbackflow reduction in Time Projection Chambers View project Nano-materials for thermal neutron detection View project". In: (2018). DOI: 10.13140/RG.2.2.16794.49600. URL: https://www.researchgate.net/publication/327816840 (cit. on p. 3).

[10] J. A. Seibert. "X-ray imaging physics for nuclear medicine technologists. Part 1: Basic principles of x-ray production." In: *Journal of nuclear medicine technology* 32 (3 2004-09), pp. 139–47. ISSN: 0091-4916. URL: http://www.ncbi.nlm.nih.gov/pubmed/15347692 (cit. on p. 4).

[11] E. Haug and W. Nakel. "Theory of the elementary process of electron-electron bremsstrahlung". In: 2004-03, pp. 147–174. DOI: 10.1142/9789812795007_0005. URL: http://www.worldscientific.com/doi/abs/10.1142/9789812795007_0005 (cit. on p. 4).

[12] F. de Beer. "Neutron and X-Ray tomography as research tools for applied research in South Africa". PhD thesis. 2018-07. DOI: 10.13140/RG.2.2.22287.89765 (cit. on p. 4).

[13] C. Suryanarayana and M. G. Norton. "X-Rays and Diffraction". In: *X-Ray Diffraction* (1998), pp. 3–19. DOI: 10.1007/978-1-4899-0148-4_1 (cit. on p. 4).

[14] M. Cooper et al. *X-Ray Compton Scattering*. Oxford University Press, 2004-10. ISBN: 9780198501688. DOI: 10.1093/acprof:oso/9780198501688.001.0001 (cit. on p. 5).

[15] R. M. Rousseau. "Concept of the influence coefficient". In: (). URL: https://www.researchgate.net/publication/313180256 (cit. on pp. 5, 6, 25).

[16] R. M. Rousseao. "Fundamental Algorithm Between Concentration and Intensity in XRF Analysis 1-Theory". In: () (cit. on p. 5).

[17] A MARKOWICZ. "An overview of quantification methods in energy-dispersive X-ray fluorescence analysis". In: *Pramana* 76 (2 2011-02), pp. 321–329. ISSN: 0304-4289. DOI: 10.1007/s12043-011-0045-z (cit. on p. 6).

[18] R. Sitko. "Theoretical influence coefficients for correction of matrix effects in x-ray fluorescence analysis of intermediate-thickness samples". In: *X-Ray Spectrometry* 35 (2 2006-03), pp. 93–100. ISSN: 0049-8246. DOI: 10.1002/xrs.867 (cit. on p. 6).

[19] B. Kanngießer. "Quantification procedures in micro X-ray fluorescence analysis". In: *Spectrochimica Acta Part B: Atomic Spectroscopy* 58 (4 2003-04), pp. 609–614. ISSN: 05848547. DOI: 10.1016/S0584-8547(02)00281-1. URL: https://linkinghub.elsevier.com/retrieve/pii/S0584854702002811 (cit. on p. 6).

[20] S. Pessanha et al. "Determination of gold leaf thickness using X-ray fluorescence spectrometry: Accuracy comparison using analytical methodology and Monte Carlo simulations". In: *Applied Radiation and Isotopes* 152 (2019-10), pp. 6–10. ISSN: 09698043. DOI: 10.1016/j.apradiso.2019.06.014. URL: https://linkinghub.elsevier.com/retrieve/pii/S0969804319300545 (cit. on pp. 6, 14, 27).

[21] I. R. M. J. S. F. C. M. S. J. F. A. Pandolfi S. Pessanha S. "Overcoming paraffin embedding constraints in the analysis of FFPE tissue samples with polarized XRF". 11th International Topical Meeting on Industrial Radiation and Radioisotope Measurement Applications (IRRMA 11). 2023. URL: https://irrma.ing.unibo.it/index.php/en/programme (cit. on p. 7).

[22] S. Pessanha et al. "A novel portable energy dispersive X-ray fluorescence spectrometer with triaxial geometry". In: *Journal of Instrumentation* 12 (01 2017-01), P01014–P01014. ISSN: 1748-0221. DOI: 10.1088/1748-0221/12/01/P01014. URL: https://iopscience.iop.org/article/10.1088/1748-0221/12/01/P01014 (cit. on pp. 7, 8, 15).

[23] A. A. Dias et al. "Quantitative evaluation of ante-mortem lead in human remains of the 18 th century by triaxial geometry and bench top micro X-ray fluorescence spectrometry". In: *Journal of Analytical Atomic Spectrometry* 30 (12 2015), pp. 2488–2495. ISSN: 0267-9477. DOI: 10.1039/C5JA00340G. URL: http://xlink.rsc.org/?DOI=C5JA00340G (cit. on pp. 7, 15).

[24] P. Custódio et al. "Direct analysis of human blood (mothers and newborns) by energy dispersive X-ray fluorescence". In: *Journal of Trace Elements in Medicine and Biology* 19 (2-3 2005-12), pp. 151–158. ISSN: 0946672X. DOI: 10.1016/j.jtemb.2005.09.002. URL: https://linkinghub.elsevier.com/retrieve/pii/S0946672X05001045 (cit. on p. 7).

[25] S. Pessanha et al. "A simple and sustainable portable triaxial energy dispersive X-ray fluorescence method for in situ multielemental analysis of mining water samples". In: *Spectrochimica Acta Part B: Atomic Spectroscopy* 164 (2020-02), p. 105762. ISSN: 05848547. DOI: 10.1016/j.sab.2019.105762. URL: https://linkinghub.elsevier.com/retrieve/pii/S0584854719305634 (cit. on p. 8).

[26] L. Strüder, P. Lechner, and P. Leutenegger. "Silicon drift detector the key to new experiments". In: *The Science of Nature* 85 (11 1998-11), pp. 539–543. ISSN: 0028-1042. DOI: 10.1007/s001140050545. URL: http://link.springer.com/10.1007/s001140050545 (cit. on p. 9).

[27] S. Usman and A. Patil. "Radiation detector deadtime and pile up: A review of the status of science". In: *Nuclear Engineering and Technology* 50 (7 2018-10), pp. 1006–1016. ISSN: 17385733. DOI: 10.1016/j.net.2018.06.014 (cit. on p. 9).

[28] R. Tertian and F. Claisse. *Principles of quantitative X-ray fluorescence analysis*. Heyden, 1982 (cit. on pp. 9, 10).

[29] J. Machado et al. "Accuracy improvement in XRF analysis for the quantification of elements ranging from tenths to thousands mug g ¹ in human tissues using different matrix reference materials". In: *Journal of Analytical Atomic Spectrometry* 35 (12 2020-12), pp. 2920–2927. ISSN: 0267-9477. DOI: 10.1039/D0JA00307G. URL: http://xlink.rsc.org/?DOI=D0JA00307G (cit. on p. 10).

[30] J Sherman. "The theoretical derivation of fluorescent X-ray intensities from mixtures". In: *Spectrochimica Acta* 7 (5 1955-12), pp. 283–306. ISSN: 03711951. DOI: 10.1016/0371-1951(55)80081-1. URL: https://linkinghub.elsevier.com/retrieve/pii/0371195155800811 (cit. on pp. 10, 25).

[31] H. A. V. Sprang. "FUNDAMENTAL PARAMETER METHODS IN XRF SPECTROSCOPY". In: (2000). URL: www.dxcicdd.com (cit. on p. 10).

[32] T. Schoonjans et al. "Fundamental parameter based quantification algorithm for confocal nano-X-ray fluorescence analysis". In: *Spectrochimica Acta Part B: Atomic Spectroscopy* 67 (2012-01), pp. 32–42. ISSN: 05848547. DOI: 10.1016/j.sab.2011.12.006. URL: https://linkinghub.elsevier.com/retrieve/pii/S0584854711002485 (cit. on p. 10).

[33] T. Shiraiwa and N. Fujino. "Theoretical Calculation of Fluorescent X-Ray Intensities in Fluorescent X-Ray Spectrochemical Analysis." In: *Japanese Journal of Applied Physics* 5 (10 1966-10), p. 886. ISSN: 0021-4922. DOI: 10.1143/JJAP.5.886. URL: https://iopscience.iop.org/article/10.1143/JJAP.5.886 (cit. on pp. 10, 25).

[34] P. Amaro et al. "Validation of the Geant4 Monte Carlo package for X-ray fluorescence spectroscopy in triaxial geometry". In: *Spectrochimica Acta Part B: Atomic Spectroscopy* 130 (2017-04), pp. 60–66. ISSN: 05848547. DOI: 10.1016/j.sab.2017.02.012. URL: https://linkinghub.elsevier.com/retrieve/pii/S0584854716302476 (cit. on p. 10).

[35] S. Akbulut. "Validation of classical quantitative fundamental parameters method using multivariate calibration procedures for trace element analysis in ED-XRF". In: *J. Anal. At. Spectrom.* 29 (5 2014), pp. 853–860. ISSN: 0267-9477. DOI: 10.1039/C3JA50377A. URL: http://xlink.rsc.org/?DOI=C3JA50377A (cit. on p. 10).

[36] J. H. Hubbell and S. M. Seltzer. "NIST Standard Reference Database 126". In: (2004-07) (cit. on pp. 19, 26, 27).

[37] R. D. Deslattes et al. "X-ray transition energies: new approach to a comprehensive evaluation". In: *Reviews of Modern Physics* 75 (1 2003-01), pp. 35–99. ISSN: 0034-6861. DOI: 10.1103/RevModPhys.75.35. URL: https://link.aps.org/doi/10.1103/RevModPhys.75.35 (cit. on p. 19).

[38] M. Guerra et al. "Performance of three different Si X-ray detectors for portable XRF spectrometers in cultural heritage applications". In: *Journal of Instrumentation* 7 (10 2012-10). ISSN: 17480221. DOI: 10.1088/1748-0221/7/10/C10004 (cit. on p. 20).

[39] M. V. Gysel, P. Lemberge, and P. V. Espen. "Description of Compton peaks in energy-dispersive x-ray fluorescence spectra". In: *X-Ray Spectrometry* 32 (2 2003), pp. 139–147. ISSN: 00498246. DOI: 10.1002/xrs.628 (cit. on p. 21).

[40] M. Newville et al. "lmfit/lmfit-py: 1.2.2". In: (2016-07) (cit. on p. 22).

[41] P. Virtanen et al. "scipy/scipy: SciPy 1.11.2". In: (2023-08) (cit. on p. 22).

[42] M. Lankosz and P. A. Pella. "A new approach to quantitative x-ray microfluorescence analysis of individual particles". In: *X-Ray Spectrometry* 26 (6 1997-11), pp. 347–349. ISSN: 0049-8246. DOI: 10.1002/(SICI)1097-4539(199711/12)26:6<347::AID-XRS232>3.0.CO;2-Y. URL: https://onlinelibrary.wiley.com/doi/10.1002/(SICI)1097-4539(199711/12)26:6<347::AID-XRS232>3.0.CO;2-Y (cit. on p. 25).

[43] T. Schoonjans et al. "The xraylib library for X-raymatter interactions. Recent developments". In: *Spectrochimica Acta Part B: Atomic Spectroscopy* 66 (11-12 2011-11), pp. 776–784. ISSN: 05848547. DOI: 10.1016/j.sab.2011.09.011. URL: https://linkinghub.elsevier.com/retrieve/pii/S0584854711001984 (cit. on p. 26).

[44] D. de Boer. "Fundamental parameters for X-ray fluorescence analysis". In: *Spectrochimica Acta Part B: Atomic Spectroscopy* 44 (11 1989-01), pp. 1171–1190. ISSN: 05848547. DOI: 10.1016/0584-8547(89)80114-4. URL: https://linkinghub.elsevier.com/retrieve/pii/0584854789801144 (cit. on p. 26).

[45] K. Levenberg. "A method for the solution of certain non-linear problems in least squares". In: *Quarterly of Applied Mathematics* 2 (2 1944), pp. 164–168. ISSN: 0033-569X. DOI: 10.1090/qam/10666. URL: https://www.ams.org/qam/1944-02-02/S0033-569X-1944-10666-0/ (cit. on p. 28).

[46] D. W. Marquardt. "An Algorithm for Least-Squares Estimation of Nonlinear Parameters". In: *Journal of the Society for Industrial and Applied Mathematics* 11 (2 1963-06), pp. 431–441. ISSN: 0368-4245. DOI: 10.1137/0111030. URL: http://epubs.siam.org/doi/10.1137/0111030 (cit. on p. 28).

[47] H. P. Gavin. "Nonlinear Least Squares Parameter Estimation Problem Using Levenberg-Marquardt Method". In: *Journal of Environmental Science, Computer Science and Engineering and Technology* 6 (3 2017). ISSN: 2278179X. DOI: 10.24214/jecet.c.6.3.30313. URL: http://jecet.org/download_frontend.php?id=198&table=Section%20C:%20Engineering%20Science (cit. on p. 28).

[48] A. Elements. *Silver Copper Alloy*. http://web.archive.org/web/20080207010024/http://www.808multimedia.com/winnt/kernel.htm. Accessed: 2010-09-30 (cit. on p. 35).

Appendix A

VerX Frontend

In appendix A, it is presented the frontend of VerX software. Some of the main functions concerning the peak labelling, dark matrix or shape and type of peaks are presented along with a labelling of how to use the software. It is also presented some results as an example of the output visualization.

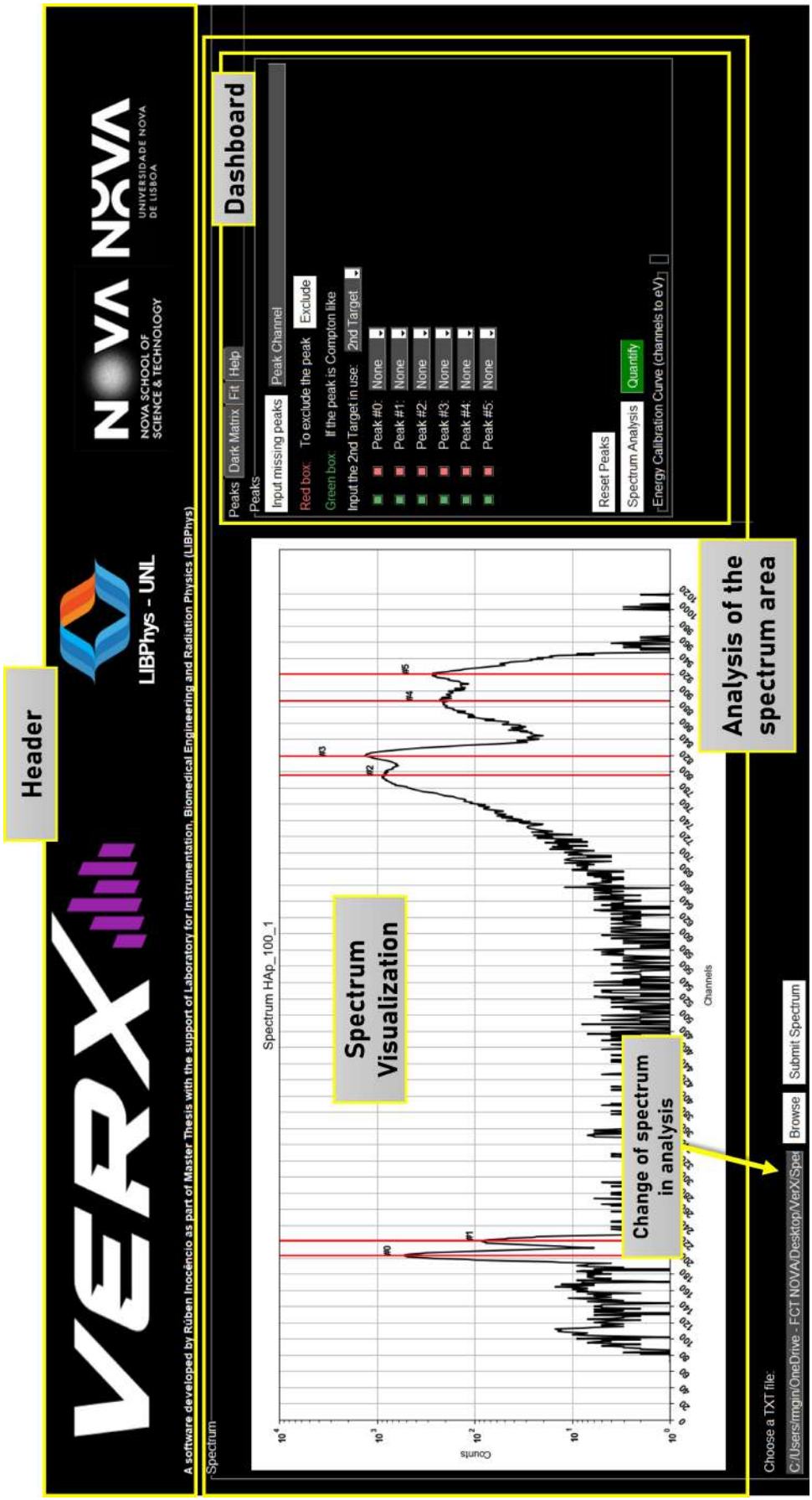

Figure A.1: Main page of VerX. It is shown the header of the software, a plot of the spectrum in analysis, a dashboard where are the features of the software and a searching box to start a new analysis on another spectrum.

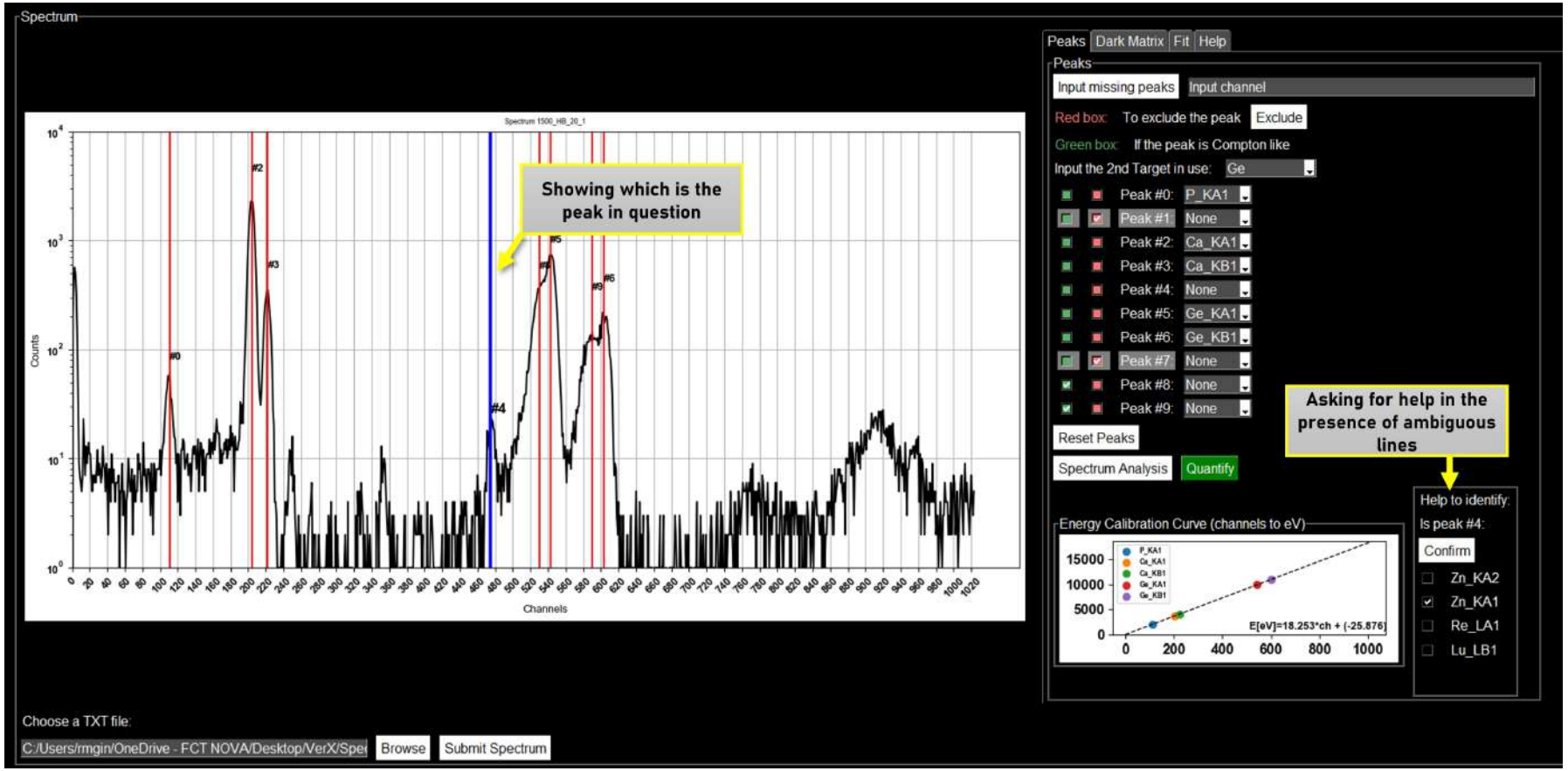

Figure A.2: Example of the calibration curve calculations. The known X-ray lines presented in the spectrum are filled in the correspondent box in *Peaks* of the dashboard. If the program detects possible misleading X-ray lines, it ask to the user for a clearer specification.

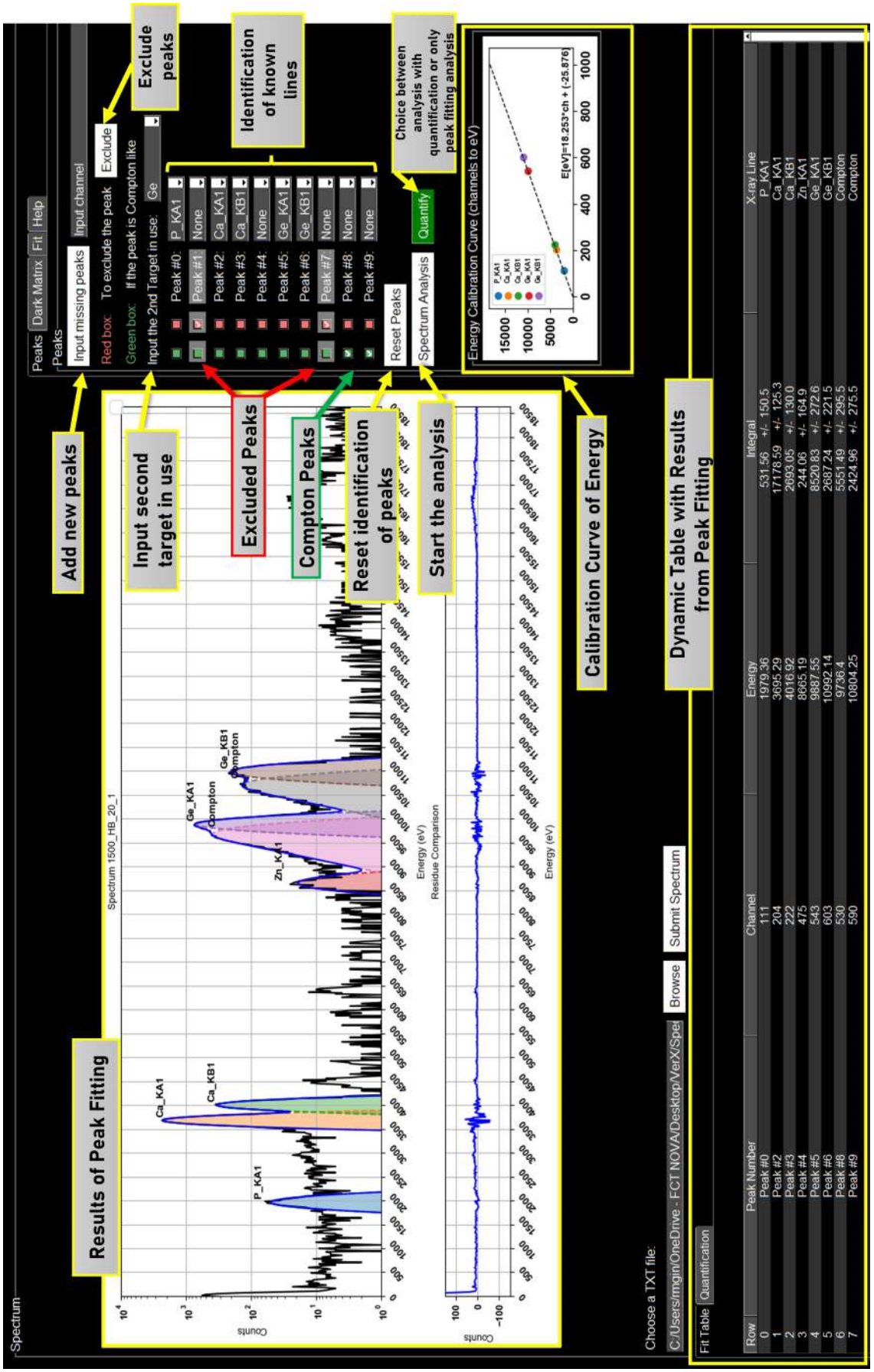

Figure A.3: Visualization of the main page after peak fitting. Is is shown a labelling of the *Peaks* tab of the dashboard, the energy calibration curve, the individual and overall fit of the spectrum and a table showing the results of the fit.

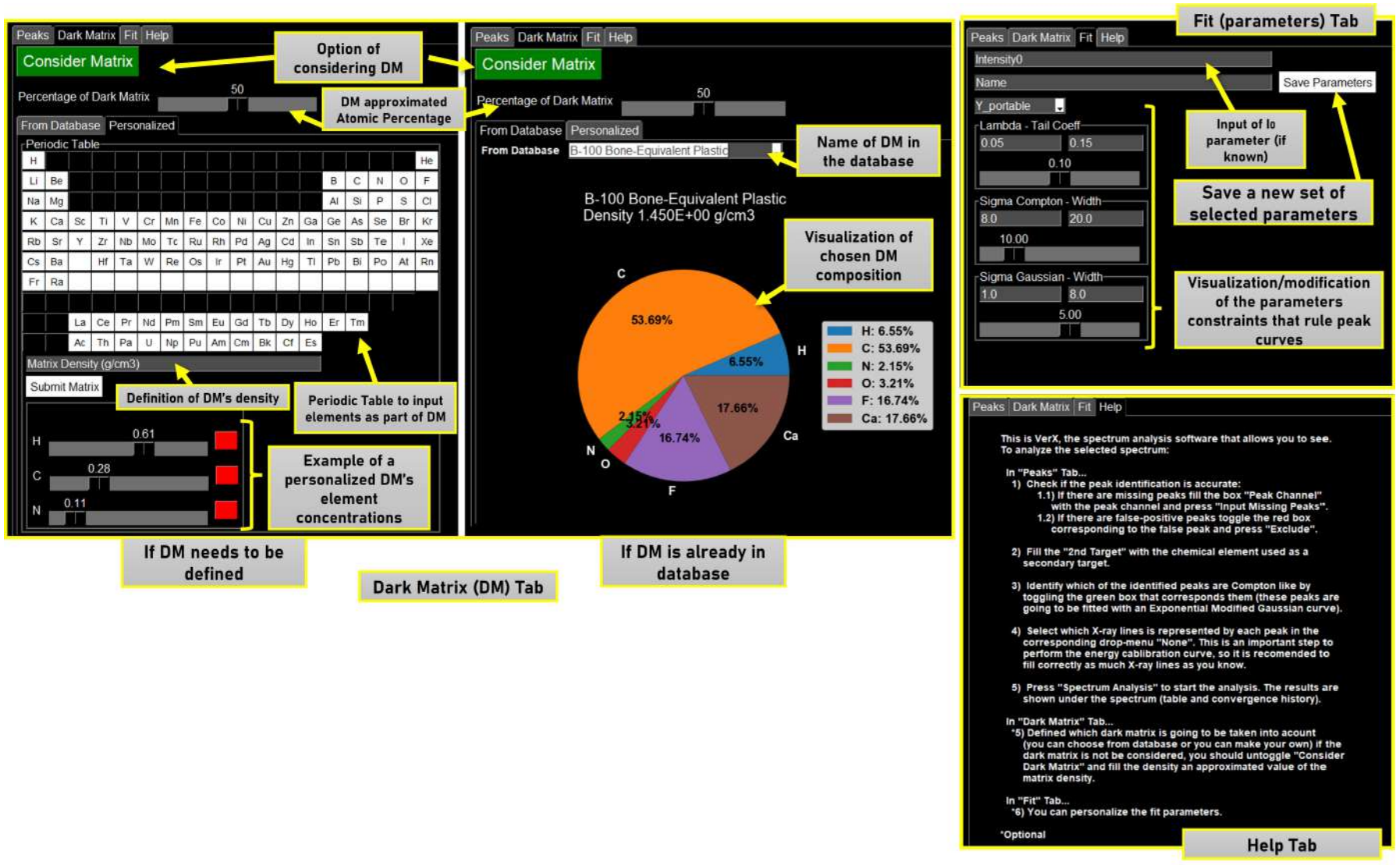

Figure A.4: Labelling of the remain tabs part of the dashboard.

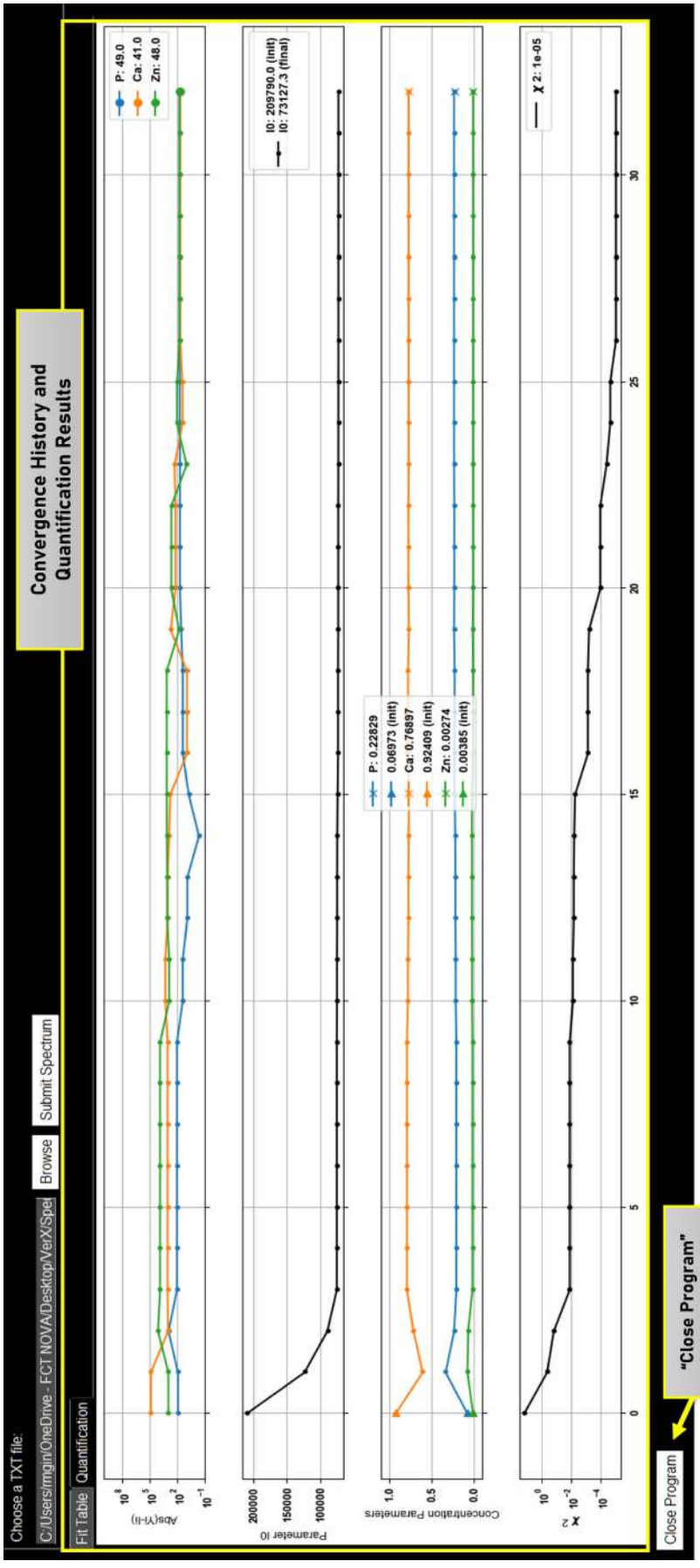

Figure A.5: Analysis results sections. There are two tabs: *Table* in which the results from the peak fitting are shown in table format; and *Quantification* in which the final results of quantification are shown along with the history of calculation during quantification (convergence history).

Appendix B

Fitting Process Results From Case Study

In this appendix are presented the results from the analyses of all the spectra acquired from the set of alloys part of the case study presented in chapter 4. To each spectra corresponds a fitted spectrum and a table describing the peak features obtained from the fitting analysis. It was only considered the Ag_{LA1}, Cu_{KA1} and the Zn_{KA1} X-ray lines for the quantification, since these X-ray lines are the ones that represent the elements that compose the alloy according with the producer. At a certain spectrum, a characteristic X-ray from Fe starts taking shape. This peak was not considered for quantification, since it represented a residual quantity similar to a contamination. Nevertheless, it was fitted in the overall fit as shown.

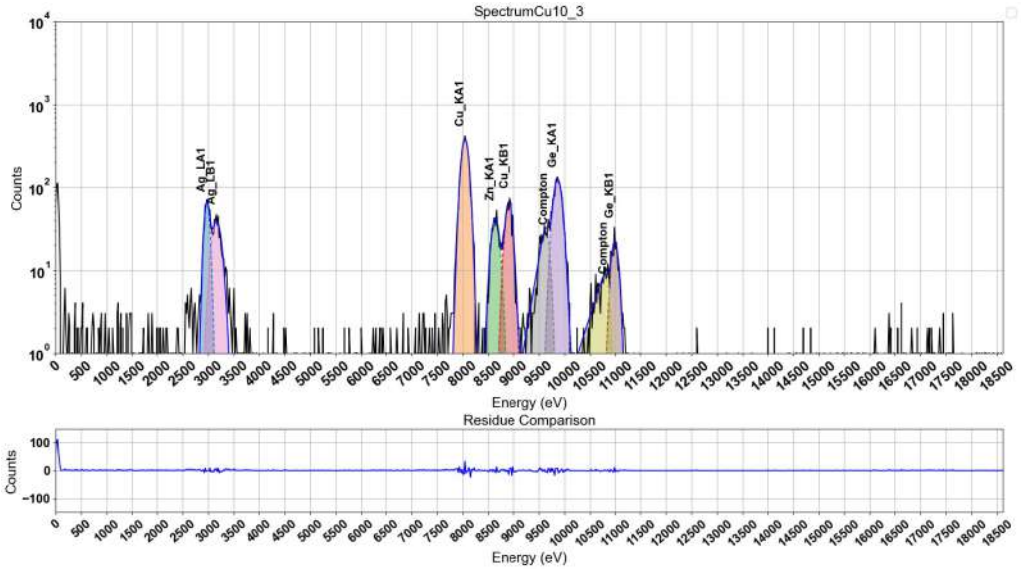

Figure B.1: Fitting results of the sample Cu_{10} (first acquisition).

Table B.1: Description of peaks found in $1Cu_{10}$ spectrum.

X-ray Line	Energy	Channel	Integral
Ag_{LA1}	2966.85	165	437 ± 50
Ag_{LB1}	3133.42	175	402 ± 58
Cu_{KA1}	8043.93	443	3586 ± 29
Zn_{KA1}	8637.60	477	430 ± 34
Cu_{KB1}	8908.14	491	642 ± 33
$Compton$	9721.46	530	504 ± 69
Ge_{KA1}	9875.20	543	1257 ± 62
$Compton$	3133.42	590	162 ± 68
Ge_{KB1}	10991.70	604	187 ± 53

Table B.2: Description of peaks found in $2Cu_{10}$ spectrum.

X-ray Line	Energy	Channel	Integral
Ag_{LA1}	2978.94	165	278.97 ± 42.5
Ag_{LB1}	3166.29	175	262.41 ± 49.9
Cu_{KA1}	8043.68	444	2425.26 ± 29.4
Zn_{KA1}	8628.52	475	390.93 ± 37.2
Cu_{KB1}	8903.68	490	466.5 ± 36.8
$Compton$	9750.04	530	1133.81 ± 75.8
Ge_{KA1}	9876.6	543	1488.1 ± 71.7
$Compton$	10810.71	590	279.27 ± 51.9
Ge_{KB1}	10981.5	605	309.19 ± 43.3

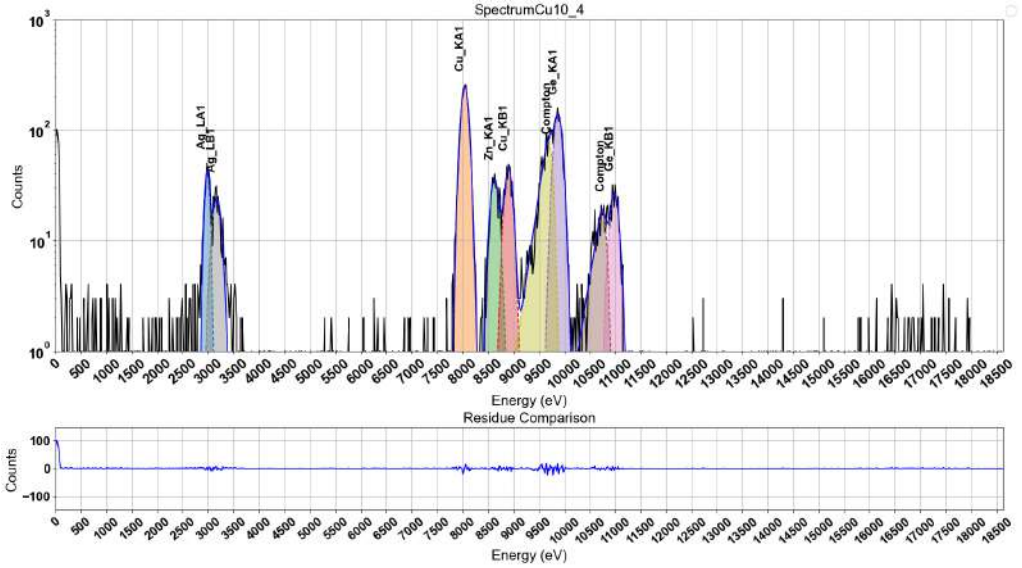

Figure B.2: Fitting results of the sample Cu_{10} (second acquisition).

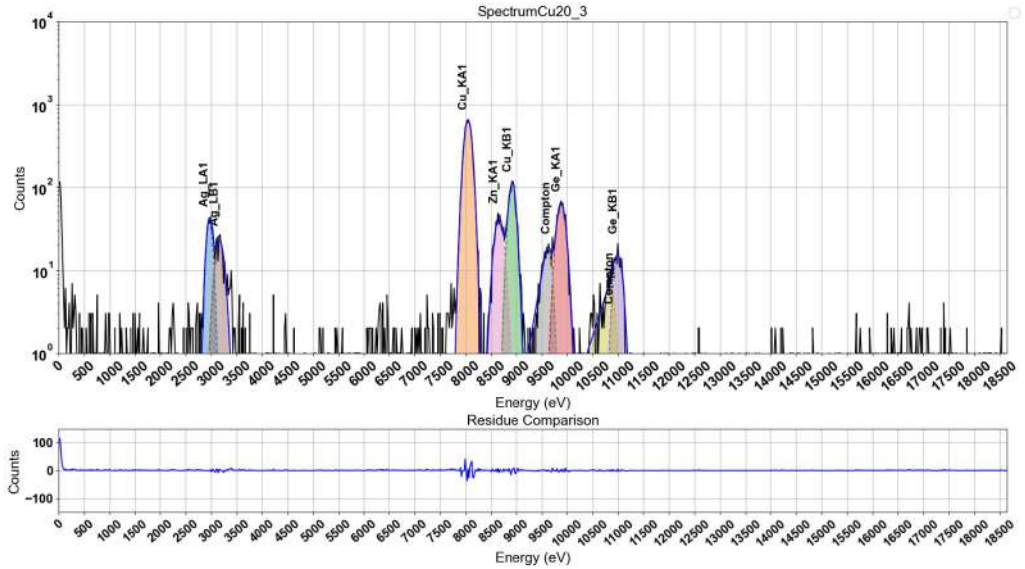

Figure B.3: Fitting results of the sample Cu_{20} (first acquisition).

Table B.3: Description of peaks found in $1Cu_{20}$ spectrum.

X-ray Line	Energy	Channel	Integral
Ag_{LA1}	2962.67	166	300.72 ± 63.4
Ag_{LB1}	3159.59	175	274.01 ± 70.9
Cu_{KA1}	8045.83	443	6239.13 ± 33.2
Zn_{KA1}	8651.68	475	500.94 ± 44.9
Cu_{KB1}	8918.36	491	1052.68 ± 40.7
$Compton$	9681.59	530	239.72 ± 48.4
Ge_{KA1}	9881.28	543	715.49 ± 40.6
$Compton$	10891.13	590	93.84 ± 126.0
Ge_{KB1}	10997.42	604	155.46 ± 124.9

Table B.4: Description of peaks found in $2Cu_{10}$ spectrum.

X-ray Line	Energy	Channel	Integral
Ag_{LA1}	2964.06	166	482.36 ± 41.6
Ag_{LB1}	3156.15	175	451.05 ± 49.2
Cu_{KA1}	8055.44	443	9561.08 ± 34.4
Zn_{KA1}	8653.64	475	531.06 ± 42.0
Cu_{KB1}	8922.93	488	1540.56 ± 40.2
$Compton$	9704.89	530	269.89 ± 50.8
Ge_{KA1}	9899.39	542	1199.32 ± 41.1
$Compton$	10778.06	590	80.84 ± 54.5
Ge_{KB1}	10997.79	604	246.5 ± 43.7

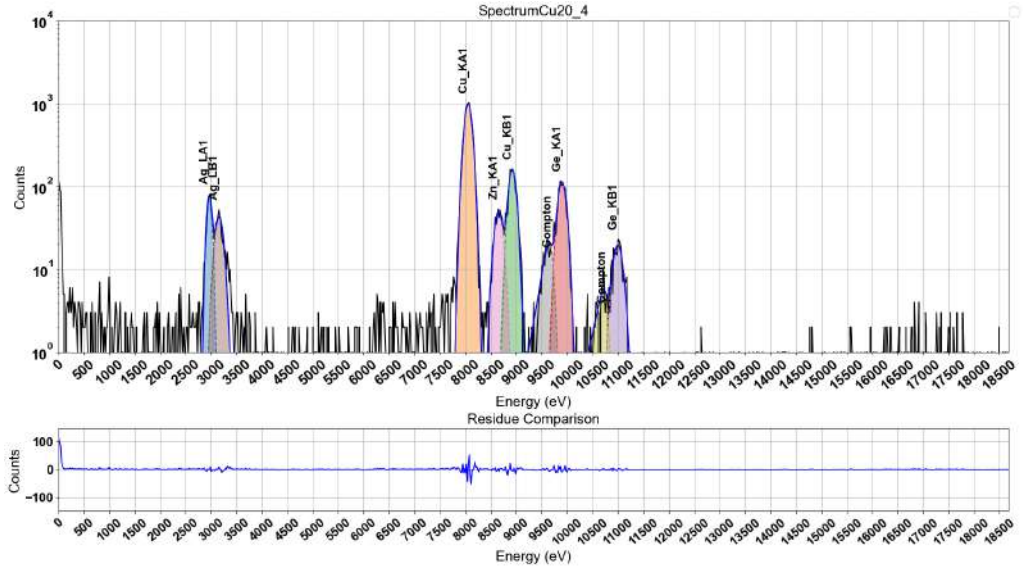

Figure B.4: Fitting results of the sample Cu_{20} (second acquisition).

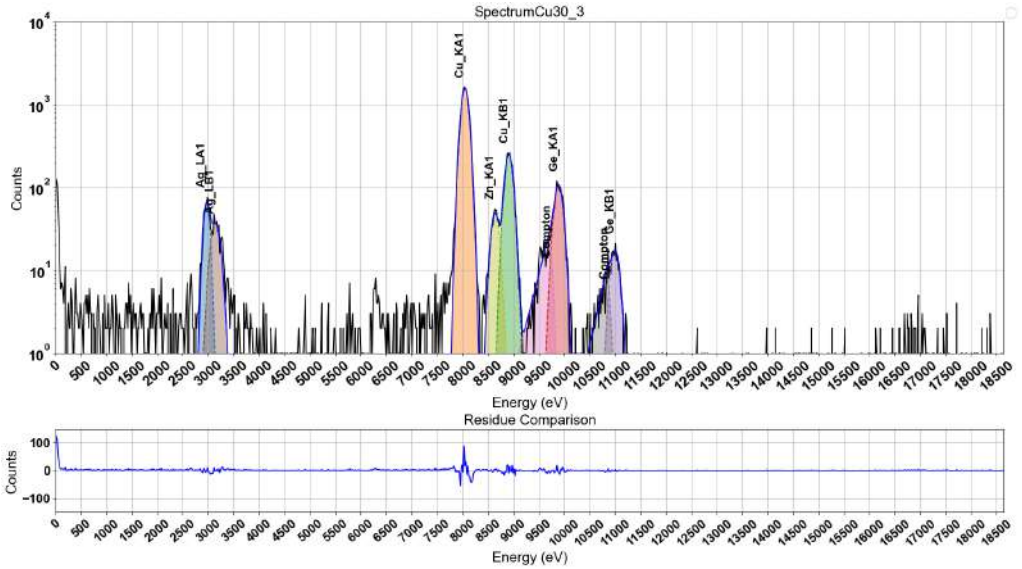

Figure B.5: Fitting results of the sample Cu_{30} (first acquisition).

Table B.5: Description of peaks found in $1Cu_{30}$ spectrum.

X-ray Line	Energy	Channel	Integral
Ag_{LA1}	2967.72	166	483.49 ± 190.8
Ag_{LB1}	3143.56	175	443.49 ± 136.6
Cu_{KA1}	8049.01	442	15196.78 ± 40.5
Zn_{KA1}	8641.53	475	496.38 ± 40.4
Cu_{KB1}	8912.56	491	2536.15 ± 44.2
$Compton$	9748.7	530	331.02 ± 70.7
Ge_{KA1}	9889.29	542	1174.41 ± 69.5
$Compton$	10884.25	590	114.36 ± 89.3
Ge_{KB1}	10997.59	605	192.95 ± 87.1

Table B.6: Description of peaks found in $2Cu_{30}$ spectrum.

X-ray Line	Energy	Channel	Integral
Ag_{LA1}	2971.72	165	351.34 ± 65.1
Ag_{LB1}	3156.91	175	468.03 ± 79.0
Cu_{KA1}	8046.34	443	14136.66 ± 36.6
Zn_{KA1}	8655.6	475	560.82 ± 55.1
Cu_{KB1}	8917.61	489	2322.47 ± 52.1
$Compton$	9817.22	530	417.1 ± 220.2
Ge_{KA1}	9895.16	545	955.34 ± 229.6
$Compton$	10893.01	590	117.88 ± 125.7
Ge_{KB1}	11000.6	604	184.73 ± 127.4

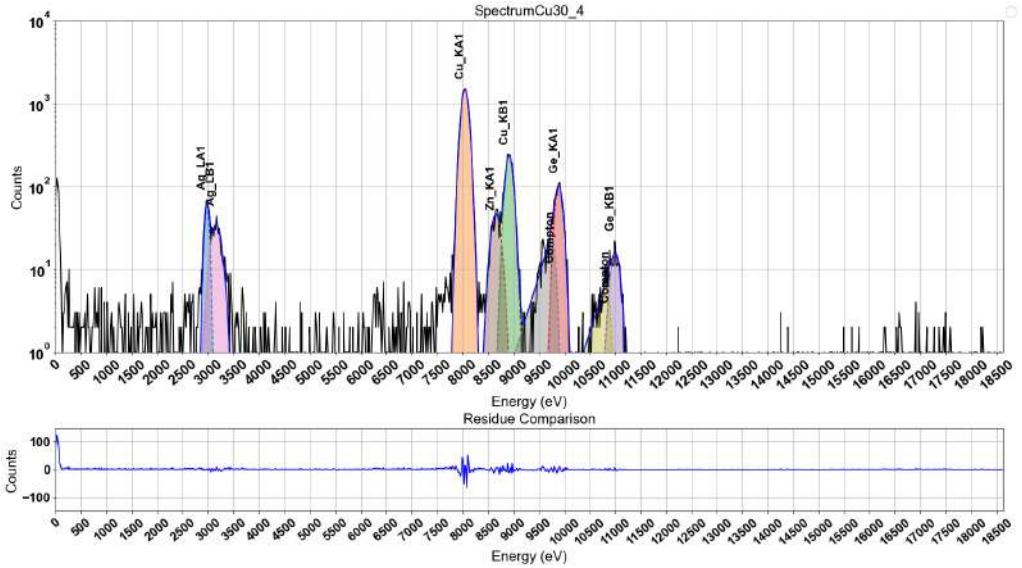

Figure B.6: Fitting results of the sample Cu_{30} (second acquisition).

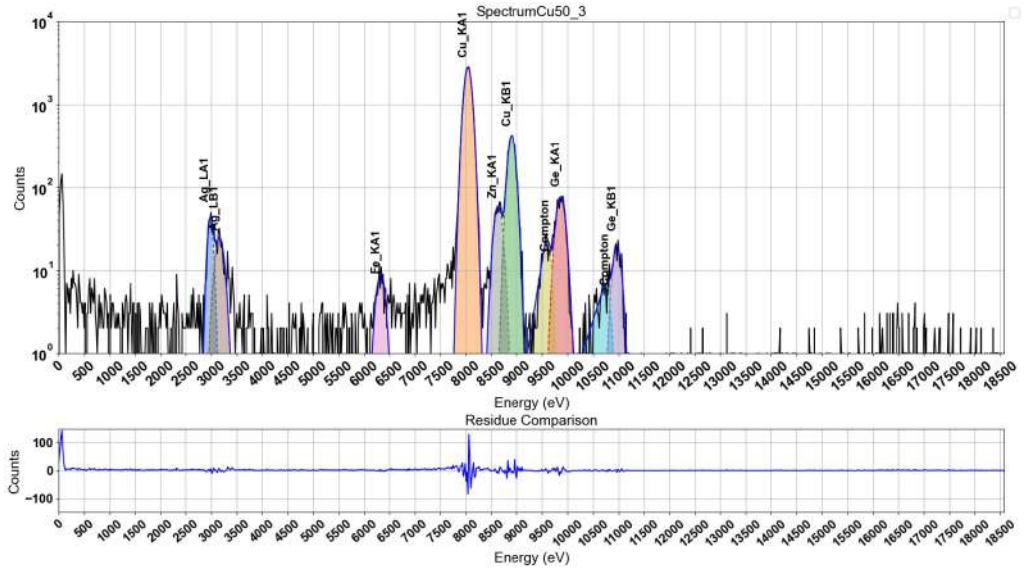

Figure B.7: Fitting results of the sample Cu_{50} (first acquisition).

Table B.7: Description of peaks found in $1Cu_{50}$ spectrum.

X-ray Line	Energy	Channel	Integral
Ag_{LA1}	2974.08	165	230.94 ± 127.6
Ag_{LB1}	3144.19	175	356.51 ± 148.4
Cu_{KA1}	8040.08	444	26854.41 ± 45.7
Fe_{KA1}	6339.3	350	122.87 ± 57.5
Zn_{KA1}	8630.3	475	634.83 ± 55.2
Cu_{KB1}	8902.08	491	4187.47 ± 53.4
$Compton$	9639.82	530	263.12 ± 61.2
Ge_{KA1}	9862.8	546	897.75 ± 57.7
$Compton$	10821.67	590	122.65 ± 100.9
Ge_{KB1}	10966.14	605	205.48 ± 78.7

Table B.8: Description of peaks found in $2Cu_{50}$ spectrum.

X-ray Line	Energy	Channel	Integral
Ag_{LA1}	2977.03	165	342.98 ± 67.2
Ag_{LB1}	3163.73	175	326.75 ± 78.8
Cu_{KA1}	8059.11	443	27544.86 ± 45.5
Fe_{KA1}	6348.16	350	126.42 ± 57.4
Zn_{KA1}	8640.74	475	589.51 ± 55.5
Cu_{KB1}	8921.59	490	4329.19 ± 55.2
$Compton$	9736.78	530	309.41 ± 79.9
Ge_{KA1}	9899.81	545	855.96 ± 62.5
$Compton$	10784.03	590	73.24 ± 67.0
Ge_{KB1}	10995.18	601	242.68 ± 62.0

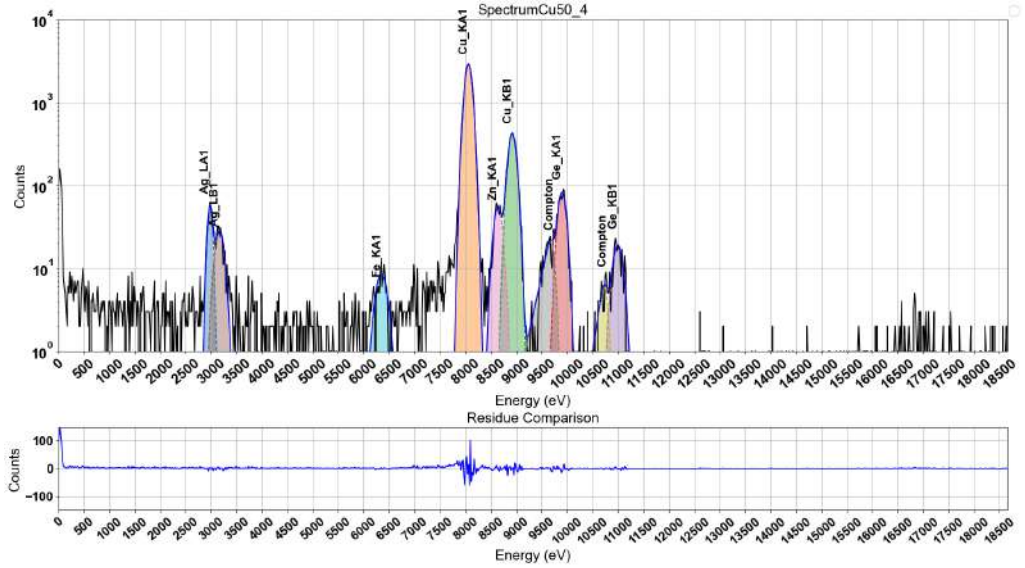

Figure B.8: Fitting results of the sample Cu_{50} (second acquisition).

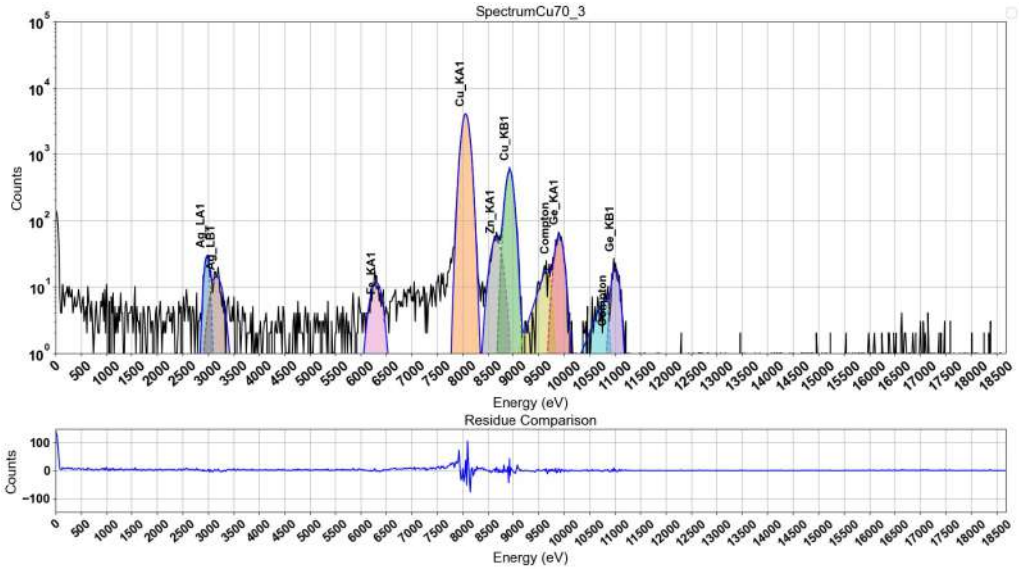

Figure B.9: Fitting results of the sample Cu_{70} (first acquisition).

Table B.9: Description of peaks found in $1Cu_{70}$ spectrum.

X-ray Line	Energy	Channel	Integral
Ag_{LA1}	2968.8	166	216.12 ± 108.6
Ag_{LB1}	3163.49	175	178.91 ± 126.8
Cu_{KA1}	8060.71	443	38809.17 ± 48.3
Fe_{KA1}	6297.86	350	177.51 ± 60.8
Zn_{KA1}	8660.47	475	746.52 ± 80.6
Cu_{KB1}	8928.79	490	5682.86 ± 74.0
$Compton$	9727.59	530	297.87 ± 87.2
Ge_{KA1}	9904.14	543	652.54 ± 65.8
$Compton$	10851.94	590	116.39 ± 98.1
Ge_{KB1}	11004.57	602	192.52 ± 64.8

Table B.10: Description of peaks found in $2Cu_{70}$ spectrum.

X-ray Line	Energy	Channel	Integral
Ag_{LA1}	2983.84	166	223.25 ± 83.0
Ag_{LB1}	3165.7	175	210.03 ± 92.6
Cu_{KA1}	8051.85	443	38165.03 ± 46.9
Fe_{KA1}	6321.79	350	195.87 ± 61.9
Zn_{KA1}	8656.82	475	758.15 ± 74.9
Cu_{KB1}	8916.21	490	5626.26 ± 69.6
$Compton$	9666.63	530	222.65 ± 67.4
Ge_{KA1}	9879.7	543	711.06 ± 59.6
$Compton$	10843.25	590	88.8 ± 108.0
Ge_{KB1}	10999.41	605	211.56 ± 94.0

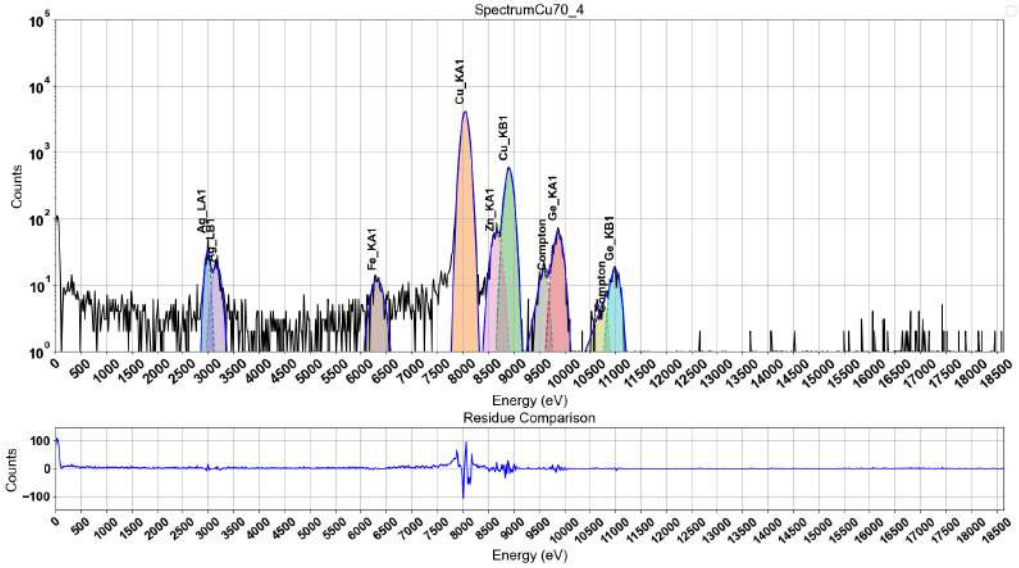

Figure B.10: Fitting results of the sample Cu_{70} (second acquisition).

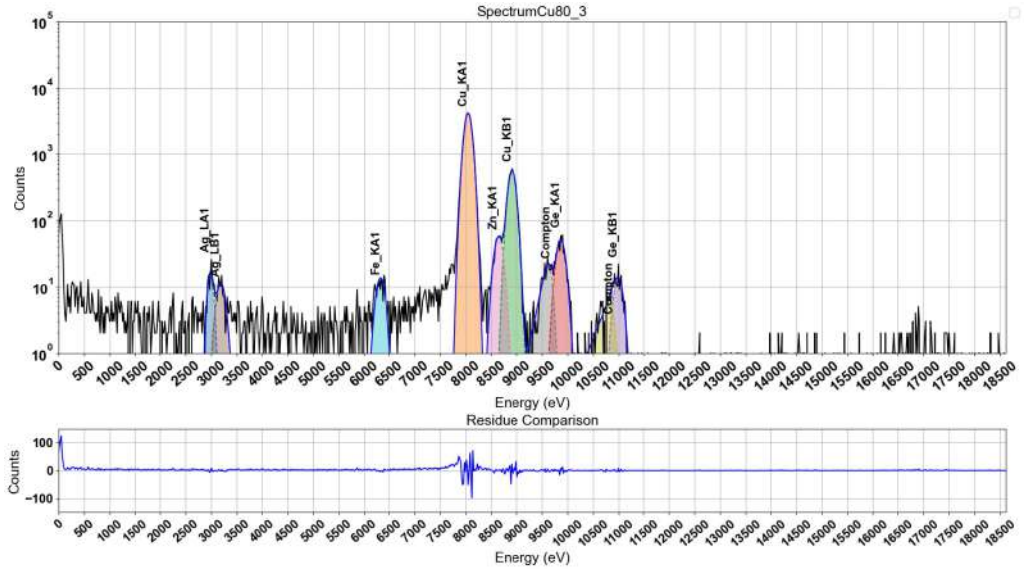

Figure B.11: Fitting results of the sample Cu_{80} (first acquisition).

Table B.11: Description of peaks found in $1Cu_{80}$ spectrum.

X-ray Line	Energy	Channel	Integral
Ag_{LA1}	2979.73	166	162.49 ± 57.5
Ag_{LB1}	3184.89	175	145.44 ± 54.9
Cu_{KA1}	8045.79	443	39832.99 ± 44.6
Fe_{KA1}	6320.46	350	198.58 ± 58.5
Zn_{KA1}	8640.95	475	623.25 ± 57.6
Cu_{KB1}	8910.54	490	5785.61 ± 55.7
$Compton$	9684.15	530	287.66 ± 68.7
Ge_{KA1}	9870.52	545	574.22 ± 60.6
$Compton$	10907.13	590	120.93 ± 326.4
Ge_{KB1}	10995.24	605	154.63 ± 341.7

Table B.12: Description of peaks found in $2Cu_{80}$ spectrum.

X-ray Line	Energy	Channel	Integral
Ag_{LA1}	2989.1	165	129.37 ± 71.2
Ag_{LB1}	3193.71	175	64.58 ± 57.8
Cu_{KA1}	8053.02	443	27849.13 ± 41.0
Fe_{KA1}	6343.66	350	141.41 ± 53.8
Zn_{KA1}	8679.55	475	712.0 ± 89.9
Cu_{KB1}	8921.22	490	4024.58 ± 81.7
$Compton$	9698.53	530	270.02 ± 60.8
Ge_{KA1}	9877.15	543	512.84 ± 56.1
$Compton$	10791.87	590	65.58 ± 93.7
Ge_{KB1}	10960.6	605	148.15 ± 91.2

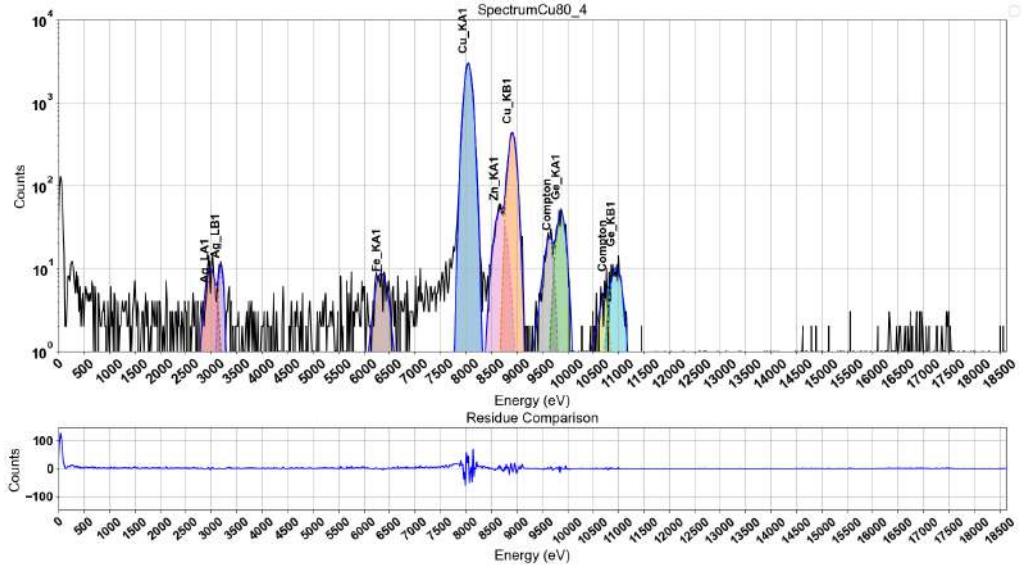

Figure B.12: Fitting results of the sample Cu_{80} (second acquisition).

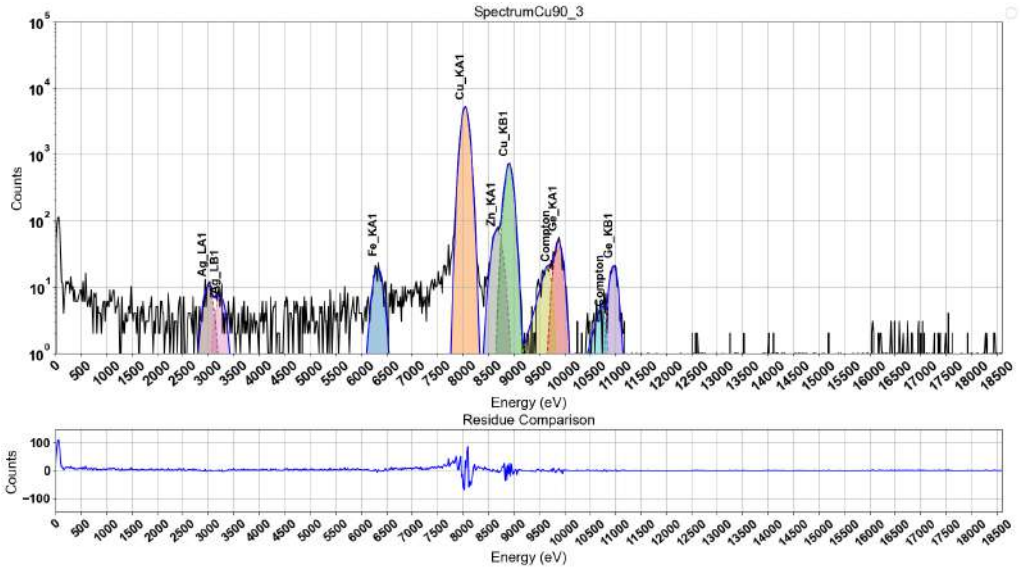

Figure B.13: Fitting results of the sample Cu_{90} (first acquisition).

Table B.13: Description of peaks found in $1Cu_{90}$ spectrum.

X-ray Line	Energy	Channel	Integral
Ag_{LA1}	2995.98	165	126.1 ± 133.5
Ag_{LB1}	3241.43	175	90.33 ± 132.8
Fe_{KA1}	6333.39	349	238.41 ± 55.0
Cu_{KA1}	8049.35	443	48995.69 ± 47.9
Zn_{KA1}	8674.7	475	909.93 ± 93.9
Cu_{KB1}	8913.31	491	6957.87 ± 88.7
$Compton$	9730.9	530	297.99 ± 91.6
Ge_{KA1}	9882.95	544	514.81 ± 76.6
$Compton$	10792.85	590	73.75 ± 78.9
Ge_{KB1}	10965.78	605	211.71 ± 59.4

Table B.14: Description of peaks found in $2Cu_{90}$ spectrum.

X-ray Line	Energy	Channel	Integral
Ag_{LA1}	2996.83	165	127.21 ± 44.8
Ag_{LB1}	3184.27	175	70.38 ± 43.4
Fe_{KA1}	6330.24	347	266.39 ± 53.2
Cu_{KA1}	8061.86	443	48162.97 ± 46.3
Zn_{KA1}	8667.77	475	784.29 ± 76.0
Cu_{KB1}	8926.21	491	7152.07 ± 70.8
$Compton$	9723.49	530	283.8 ± 77.2
Ge_{KA1}	9892.12	543	520.77 ± 65.1
$Compton$	10925.94	590	122.47 ± 530.3
Ge_{KB1}	10998.02	603	157.93 ± 530.8

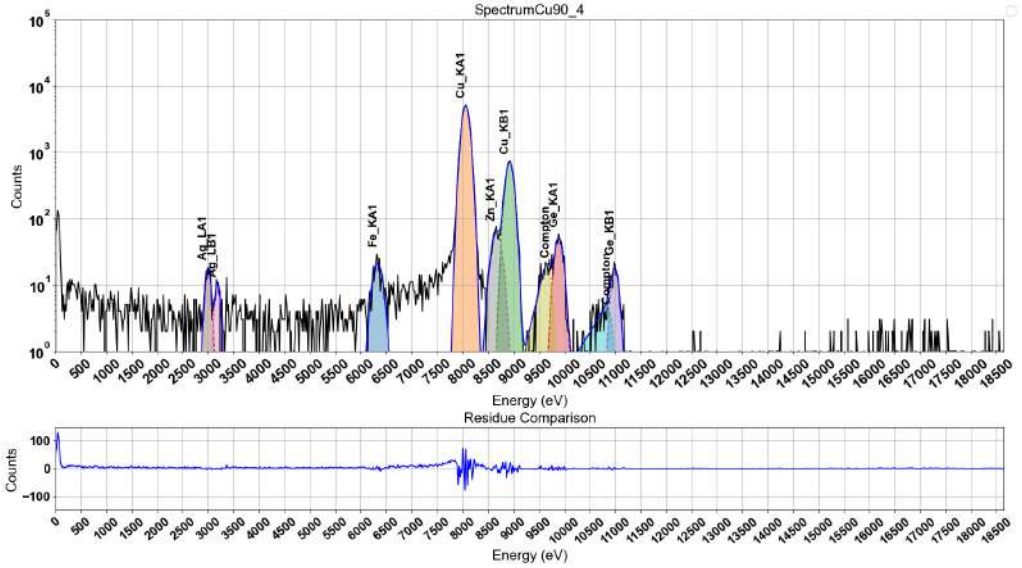

Figure B.14: Fitting results of the sample Cu_{90} (second acquisition).

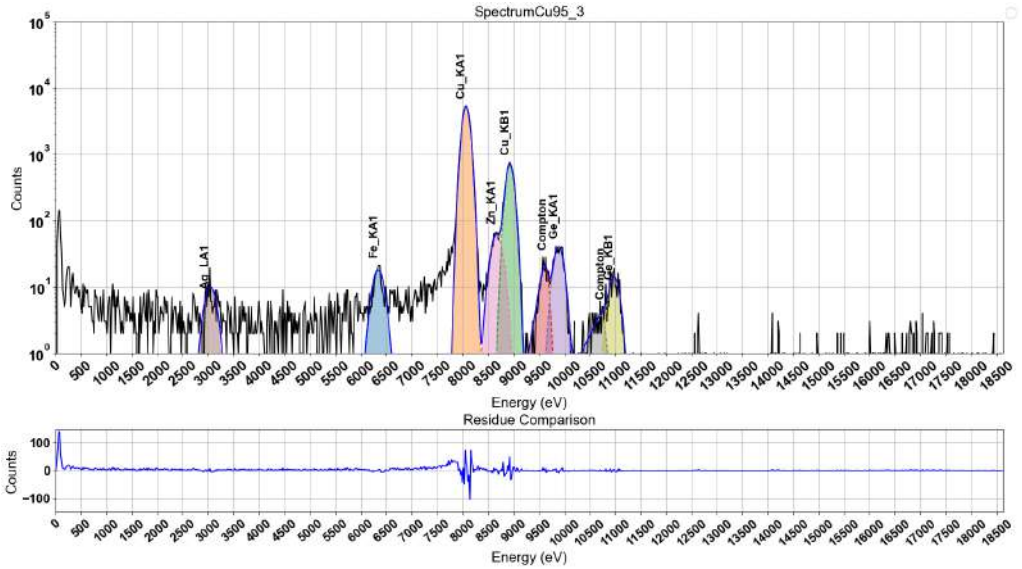

Figure B.15: Fitting results of the sample Cu_{95} (first acquisition).

Table B.15: Description of peaks found in $1Cu_{95}$ spectrum.

X-ray Line	Energy	Channel	Integral
Ag_{LA1}	3044.3	165	149.27 ± 62.0
Fe_{KA1}	6342.51	348	264.23 ± 61.6
Cu_{KA1}	8068.5	443	50377.77 ± 49.3
Zn_{KA1}	8670.05	475	881.63 ± 97.1
Cu_{KB1}	8931.61	490	7104.03 ± 88.2
$Compton$	9668.65	526	233.41 ± 70.6
Ge_{KA1}	9888.32	540	503.74 ± 71.7
$Compton$	10800.99	590	81.59 ± 122.7
Ge_{KB1}	10976.61	605	191.54 ± 88.8

Table B.16: Description of peaks found in $2Cu_{95}$ spectrum.

X-ray Line	Energy	Channel	Integral
Ag_{LA1}	2981.89	165	93.28 ± 67.7
Ag_{LB1}	3233.85	175	79.15 ± 79.0
Fe_{KA1}	6309.47	350	206.89 ± 66.9
Cu_{KA1}	8039.46	443	53276.87 ± 54.6
Zn_{KA1}	8643.84	475	829.89 ± 88.3
Cu_{KB1}	8902.73	492	7643.81 ± 81.5
$Compton$	9654.4	530	253.75 ± 78.1
Ge_{KA1}	9856.57	546	537.57 ± 73.6
$Compton$	10892.01	590	90.48 ± 259.5
Ge_{KB1}	10988.34	605	135.18 ± 259.7

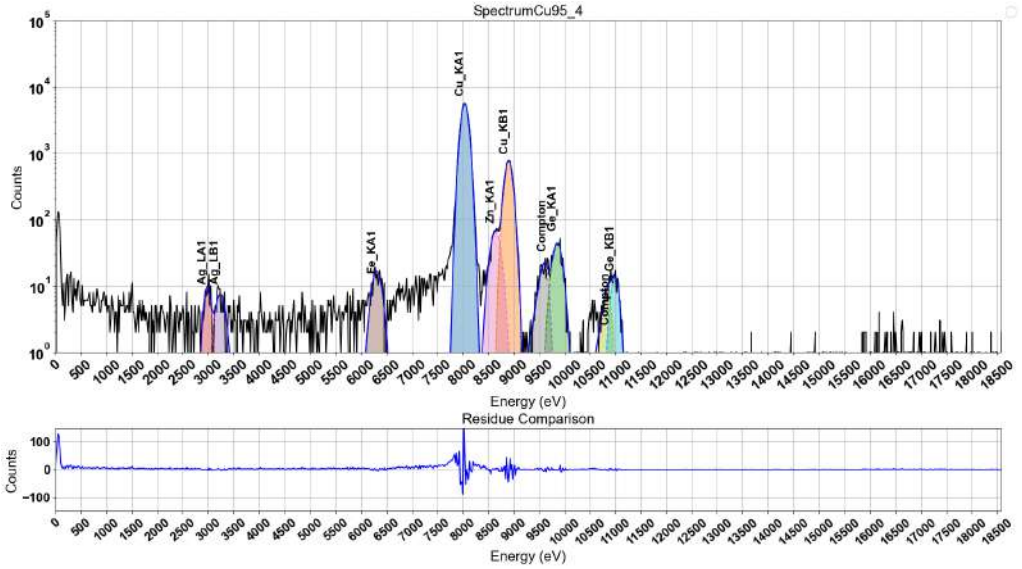

Figure B.16: Fitting results of the sample Cu_{95} (second acquisition).

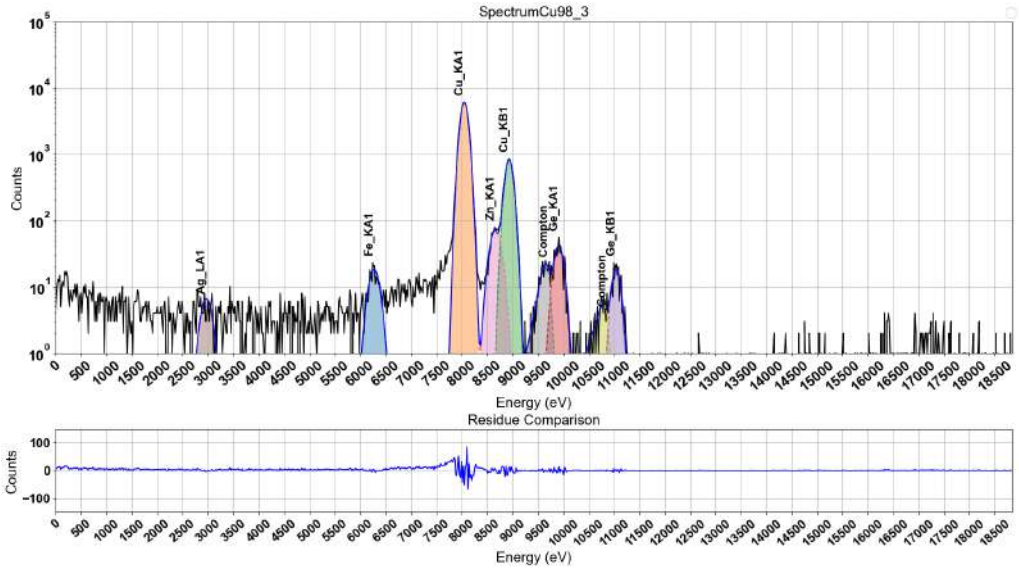

Figure B.17: Fitting results of the sample Cu_{98} (first acquisition).

Table B.17: Description of peaks found in $1Cu_{98}$ spectrum.

X-ray Line	Energy	Channel	Integral
Ag_{LA1}	2178.09	166	86.06 ± 35.9
Fe_{KA1}	5774.78	346	251.89 ± 47.7
Cu_{KA1}	8290.96	475	995.57 ± 66.4
Zn_{KA1}	9591.9	543	488.55 ± 65.3
Cu_{KB1}	10778.13	601	200.13 ± 62.9
$Compton$	9377.5	530	273.9 ± 70.7
Ge_{KA1}	10590.84	590	91.92 ± 84.2
$Compton$	8568.9	491	8169.07 ± 68.0
Ge_{KA2}	7641.6	443	57745.91 ± 49.1

Table B.18: Description of peaks found in $2Cu_{98}$ spectrum.

X-ray Line	Energy	Channel	Integral
Ag_{LA1}	3020.78	165	109.6 ± 58.1
Fe_{KA1}	6341.82	348	207.86 ± 58.1
Cu_{KA1}	8058.33	443	42712.85 ± 46.3
Zn_{KA1}	8653.03	475	811.58 ± 81.4
Cu_{KB1}	8919.49	490	6028.34 ± 74.4
$Compton$	9647.52	530	220.29 ± 62.8
Ge_{KA1}	9855.37	544	430.55 ± 58.6
$Compton$	10772.25	590	86.01 ± 80.0
Ge_{KA2}	10967.44	605	179.69 ± 66.3

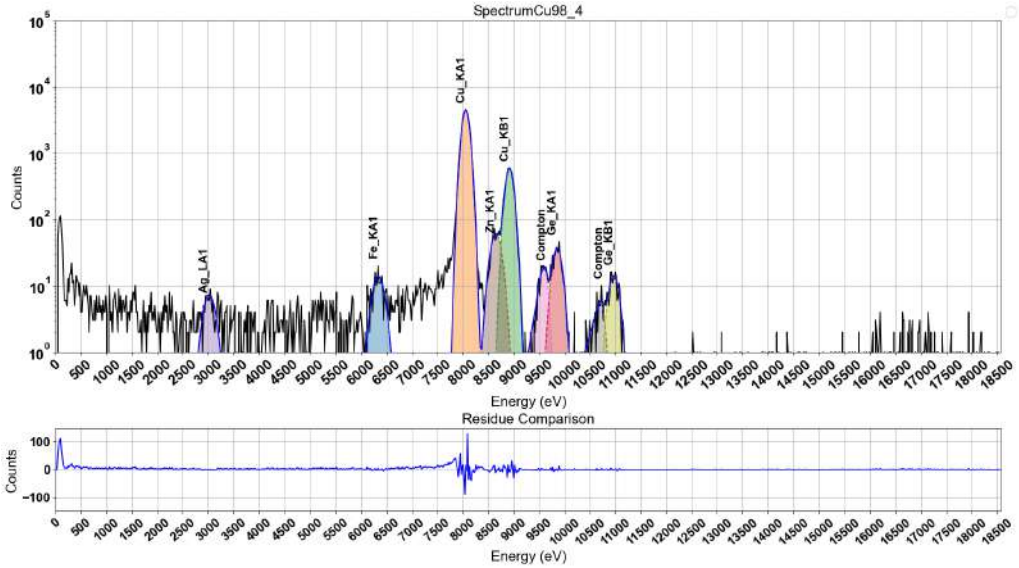

Figure B.18: Fitting results of the sample Cu_{98} (second acquisition).

ANNEX

Certified Reference Material Datasheet (table with composition) - DORM-4 Fish Flesh

National Research Council Canada | Conseil national de recherches Canada

Certificate of Analysis

Certified Reference Material

DORM-4

Fish Protein Certified Reference Material for Trace Metals and other Constituents

The following tables show those constituents for which certified, reference and information values have been established for this fish protein certified reference material (CRM).

The expanded uncertainty (U_{CRM}) in the certified value is equal to $U = ku_c$ where u_c is the combined standard uncertainty calculated according to the JCGM Guide [1] and k is the coverage factor. A coverage factor of two (2) was applied for all elements which corresponds to approx. 95 % confidence. It is intended that U_{CRM} accounts for every aspect that reasonably contributes to the uncertainty of the measurement. All listed values are expressed on a dry mass basis.

Table 1: Certified quantity values and expanded uncertainty (k=2) for DORM-4

Element	Mass fraction, mg/kg	International recognition of measurement capability (CMC)
arsenic (b,d,f)	6.87 ± 0.44	MEF-14
cadmium (a,d)	0.299 ± 0.018	MEF-16
calcium (d,e)	2360 ± 140	MEF-17
chromium (a,d,e)	1.87 ± 0.18	MEF-18
copper (a,d,e)	15.7 ± 0.46	MEF-20
iron (a,d)	343 ± 20	MEF-21
lead (a,b,d)	0.404 ± 0.062	MEF-22
magnesium (d,e)	910 ± 80	MEF-23
manganese (b,d,e)	3.17 ± 0.26	MEF-24
mercury (a,c,g)	0.412 ± 0.036	MEF-25
nickel (a)	1.34 ± 0.14	MEF-28
potassium (d,e)	15 500 ± 1000	MEF-29
selenium (a,d,f)	3.45 ± 0.40	MEF-30
silver (a,d)	0.0252 ± 0.0050	MEF-31
strontium (d,e)	10.1 ± 0.8	MEF-33
vanadium (d,e)	1.57 ± 0.14	MEF-34
zinc (a,d)	51.6 ± 2.8	MEF-35

Canada

Table 1 (continued): Certified quantity values and expanded uncertainty (*k*=2) for DORM-4

Substance	Mass fraction, mg/kg	International recognition of measurement capability (CMC)
arsenobetaine (as As) (h,i)	3.95 ± 0.36	MEF-15
methylmercury (as Hg) (j,k)	0.355 ± 0.028	MEF-26

Table 2: Reference values and expanded uncertainty (*k*=2) for DORM-4

Element	Mass fraction, mg/kg	International recognition of measurement capability (CMC)
aluminium (b,d,e)	1280 ± 340 *	MEF-13
sodium (d,e)	14 000 ± 2400	MEF-32
tin (a,d)	0.061 ± 0.018	--

* Note: The mass fraction of aluminium is obtained without the use of hydrofluoric acid.

Table 3: Information values for DORM-4

Element	Mass fraction, mg/kg	International recognition of measurement capability (CMC)
cobalt (d)	0.25	MEF-19
lithium (d)	1.21	--
molybdenum (d)	0.29	MEF-27
phosphorus (d)	8000	--
uranium (d)	0.050	--

Table 3 (continued): Information values for DORM-4

Substance	Mass fraction, mg/kg (as Sn)	International recognition of measurement capability (CMC)
monobutyltin (j)	< 0.05	--
dibutyltin (j)	< 0.005	--
tributyltin (j)	< 0.005	--

Coding

The coding refers to the instrumental method of analyte determination.

- **a** Isotope dilution inductively-coupled plasma mass spectrometry (ID-ICP-MS)
- **b** Standard addition inductively-coupled plasma mass spectrometry (ICP-MS)
- **c** Inductively-coupled plasma mass spectrometry (ICP-MS)
- **d** Inductively-coupled plasma atomic emission spectroscopy (ICP-AES)
- **e** Standard addition inductively-coupled plasma atomic emission spectroscopy (ICP-AES)
- **f** Hydride generation graphite furnace atomic absorption spectroscopy
- **g** Cold-vapour atomic absorption spectroscopy (CV-AAS)

ANNEX II

Certified Reference Material Datasheet (table with composition) - SRM 1575a

National Institute of Standards and Technology
U.S. Department of Commerce

Date of Issue:
04 May 2022

Standard Reference Material® 1575a
Trace Elements in Pine Needles (*Pinus taeda*)
CERTIFICATE OF ANALYSIS

Purpose: The certified values delivered by this Standard Reference Material (SRM) are intended for use in the evaluation of techniques employed in the analysis of pine needles and materials of a similar matrix.

Description: A unit of SRM 1575a consists of approximately 50 g of dried, jet milled, radiation sterilized, and blended pine needles.

Certified Values: These values are traceable to the International System of Units (SI) [1]. The certified values for twelve elements, expressed as mass fractions [2] on a dry mass, are provided in Table 1. The certified value for mercury is based on results from a single NIST primary method, cold vapor isotope dilution inductively coupled plasma mass spectrometry, and was confirmed by radiochemical neutron activation analysis at NIST. Certified values for other elements are based on results from two or more critically evaluated independent analytical techniques. Analyses were performed at NIST and at the United States Geological Survey (USGS) (Denver, CO).

Table 1. Certified Mass Fraction Values[(a)] (Dry-Mass Basis) in SRM 1575a

Minor Constituents

Elements	Mass Fraction (%)
Phosphorus (P)	0.107 ± 0.008
Potassium (K)	0.417 ± 0.007
Calcium (Ca)	0.25 ± 0.01

Trace Elements

Elements	Mass Fraction (mg/kg)	Elements	Mass Fraction (mg/kg)
Aluminum (Al)	580 ± 30	Copper (Cu)	2.8 ± 0.2
Barium (Ba)	6.0 ± 0.2	Iron (Fe)	46 ± 2
Cadmium (Cd)	0.233 ± 0.004	Mercury (Hg)	0.0399 ± 0.0007
Chlorine (Cl)	421 ± 7	Rubidium (Rb)	16.5 ± 0.9
		Zinc (Zn)	38 ± 2

[(a)] The certified values are either the result of measurements from a single NIST primary method or the average values from two or more analytical methods. The uncertainty values represent expanded uncertainties, which include components of uncertainty from each method and for two or more analytical methods, a Type B distribution for between method uncertainty, combined according to the method described in reference 3 in compliance with the JCGM Guide [4]. The certified values are the measurands and are metrologically traceable to the SI derived unit of mass fraction expressed as percent (%) or as milligrams per kilogram (mg/kg). Analytical methods of analysis are listed in Table A2.

Non-Certified Values: Non-certified values are provided in Appendix A.

Additional Information: Additional information is provided in Appendix B.

Period of Validity: The certified values delivered by **SRM 1575a** are valid within the measurement uncertainty specified until **01 August 2032**. The certified values are nullified if the material is stored or used improperly, damaged, contaminated, or otherwise modified.

Carlos A. Gonzalez, Chief
Chemical Sciences Division

Steven J. Choquette, Director
Office of Reference Materials

Certificate Revision History on Page 2

ANNEX III

Certified Reference Material Datasheet (table with composition) - GBW07605-5 Tea Leaves

Approved by General Administration of Quality Supervision,

Inspection and Quarantine of the People's Republic of China

GBW07601- GBW07605

Certificate of Certified Reference Material

Vegetable and Human Hair

Date of Certification

Date of Expiration

Institute of Geophysical and Geochemical Exploration

(Langfang China)

Table 2. Certified values of vegetable and human hair CRMs

Element μg/g	GBW07602 (GSV-1)	GBW07603 (GSV-2)	GBW07604 (GSV-3)	GBW07605 (GSV-4)	GBW07601 (GSH-1)
Ag	0.027±0.006	0.049±0.007	(0.013)	(0.018)	0.029±0.008
Al %	0.214±0.022	0.20±0.03	0.104±0.006	(0.30)	
As	0.95±0.12	1.25±0.15	0.37±0.09	0.28±0.04	0.28±0.05
Au ng/g					(2.5)
B	34±7	38±6	53±5	15±4	(1.3)
Ba	19±3	18±2	26±4	58±6	17±2
Be	0.056±0.014	0.051±0.004	0.021 ±0.005	0.034±0.006	0.063±0.020
Bi	(0.022)	0.023±0.005	0.027±0.002	0.063±0.008	0.34±0.02
Br	2.4±0.4	3.0±0.4	7.2±1.4	3.4±0.5	(0.36)
Ca %	2.22±0.13	1.68±0.11	1.81±0.13	0.43±0.04	0.29±0.03
Cd	0.14±0.06	(0.38)	0.32+0.07	0.057±0.010	0.11±0.03
Ce	2.4±0.3	2.2±0.1	0.49±0.07	1.0±0.2	0.12±0.03
Cl %	(1.13)	(1.92)	(0.23)		
Co	0.39±0.05	0.41±0.05	0.42±0.03	0.18±0.02	0.071±0.012
Cr	2.3±0.3	2.6±0.2	0.55±0.07	0.80±0.03	0.37±0.06
Cs	0.27±0.03	0.27±0.02	0.053±0.003	0.29±0.02	
Cu	5.2±0.5	6.6±0.8	9.3±1.0	17.3±1.8	10.6±1.2
Dy		(0.13)	(0.036)	(0.074)	(0.017)
Eu	0.037±0.002	0.039±0.003	0.009±0.003	0.018±0.002	(0.006)
F	24±3	23±4	22±4	320±31	
Fe	1020±67	1070±57	274±17	264±15	54±10
Gd		(0.19)	(0.043)	(0.093)	
Hf	0.14±0.02	(0.15)	(0.026)	(0.033)	
Hg			0.026±0.003	(0.013)	0.36±0.08
Ho		(0.033)		(0.019)	
K %	0.85±0.05	0.92±0.10	1.38±0.07	1.66±0.12	(0.002)
La	1.23±0.10	1.25±0.06	0.26±0.02	0.60±0.04	0.049±0.011
Li	2.4±0.4	2.6±0.4	0.84±0.15	(0.36)	2.0±0.1
Lu		(0.011)		(0.007)	
Mg %	0.287±0.018	0.48±0.04	0.65±0.05	0.17±0.02	0.036±0.004
Mn	58±6	61±5	45±4	1240±70	6.3±0.8
Mo	0.26±0.04	0.28±0.05	0.18±0.01	0.038±0.007	0.073±0.014
N %	1.20±0.02	1.50±0.03	2.56±0.06	3.32±0.09	14.9±0.1
Na	1.10±0.10%	1.96±0.18%	200±13	44±6	152±17
Nd	(1.1)	1.0±0.1	(0.22)	(0.44)	
Ni	1.7±0.4	1.7±0.3	1.9±0.3	4.6±0.5	0.83±0.19
P	830±40	1000±40	1680±60	2840±90	170±10
Pb	7.1±1.1	47±3	1.5±0.3	4.4±0.3	8.8±1.1
Pr		(0.24)		(0.12)	
Rb	4.2±0.2	4.5±0.6	7.6±0.8	74±5	
S %	0.32±0.03	0.73±0.06	0.35±0.04	0.245±0.022	4.3±0.3
Sb	0.078±0.020	0.095±0.014	0.045±0.006	0.056±0.006	0.095±0.016
Sc	0.31±0.03	0.32±0.04	0.069±0.007	0.085±0.013	0.008±0.001
Se	0.184±0.013	0.12±0.02	0.14±0.02	(0.072)	0.60±0.04
Si %	0.58±0.04	0.60±0.07	0.71±0.08	(0.21)	0.087±0.008
Sm	0.19±0.01	0.19±0.02	0.038±0.006	0.085±0.023	(0.012)
Sn		(0.27)			
Sr	345±11	246±16	154±9	15.2±0.7	24±1
Tb	(0.026)	0.025±0.003		(0.011)	
Th	0.37±0.02	0.36±0.04	0.070±0.010	0.061±0.009	
Ti	95±18	95±20	20.4±2.2	24±4	2.7±0.6
U	(0.11)	(0.12)	(0.028)		
V	2.4±0.3	2.4±0.4	(0.64)	(0.86)	
W	(0.06)	(0.06)			
Y	(0.63)	0.68±0.02	0.145±0.015	0.36±0.04	0.084±0.020
Yb	0.063±0.014	0.063±0.009	0.018±0.004	0.044±0.005	
Zn	20.6±2.2	55±4	37±3	26.3±2.0	190±9

Note: Data behind "±"are standard deviations. Data enclosed in brackets are proposed values.